High Energy Pair Production of Muons in Electron-Positron Annihilation at Center of Mass Energies Ranging from 130 to 183GeV

by

Bryan R. Smith

Submitted to the Department of Physics
in partial fulfillment of the requirements for the degree of

Doctor of Philosophy

at the

MASSACHUSETTS INSTITUTE OF TECHNOLOGY

June 1998

Author .....
Department of Physics
May 4, 1998

Certified by .....
.....
Ulrich J. Becker
Professor
Thesis Supervisor

Accepted by .....
Thomas J. Greytak
Associate Department Head for Education

High Energy Pair Production of Muons in Electron-Positron Annihilation at Center of Mass Energies Ranging from 130 to 183GeV

by

Bryan R. Smith

Submitted to the Department of Physics
on May 4, 1998, in partial fulfillment of the
requirements for the degree of
Doctor of Philosophy

Abstract

For the process $e^+e^- \rightarrow \mu^+\mu^-(n\gamma)$, the cross section and forward-backward charge asymmetry are measured at the highest ever center of mass energies which ranged from 130 to 183GeV. The data originates from $85pb^{-1}$ of integrated luminosity collected with the L3 detector at LEP. The measured muon pair cross section and forward-backward asymmetry agree with the Standard Model prediction with a $\chi^2_{SM}/N = .61$ with 10 degrees of freedom. A mass limit on an additional heavy, neutral gauge boson of $M_{Z'} > 315$GeV is set using muon pair production alone, rising to $M_{Z'} > 805$GeV when all final states are considered. A search for an excited lepton decaying via $\mu^* \rightarrow \mu\gamma$ excludes such objects with electromagnetic coupling up to 183GeV.

Thesis Supervisor: Ulrich J. Becker
Title: Professor

Contents

1 Introduction

The cross section and forward-backward charge asymmetry for the process $e^+e^- \to \mu^+\mu^-(n\gamma)$ are measured using $85pb^{-1}$ of data taken above the Z pole at center of mass energies as large as 183GeV. The data cover the highest energy range of electron-positron annihilation ever measured.

The $85pb^{-1}$ of data was collected with the L3 detector. The L3 [1, 2] detector is located at the LEP [3, 4] accelerator complex in Geneva, Switzerland. Three other experiments, ALEPH [5], DELPHI [6], and OPAL [7], are also taking data at LEP.

The Standard Model is the currently accepted theoretical interpretation of the experimental data. No difference with the Standard Model and experimental measurements has yet been confirmed; however, the theoretical consensus is that at some energy range, the Standard Model must break down. In the early 1990s, lepton and quark pair production measurements [8] in electron-positron collisions at the Z pole provided one of the most stringent tests of the Standard Model of Electroweak interactions. In 1995-97, data from electron-positron collisions well above the Z pole has been taken. New physics processes predicted by the Standard Model, like WW pair production and ZZ pair production, start to play a role, yet the Fermion pair production observables are still important to measure in the high energy data because they are sensitive to new types of physics. For example, an additional heavy boson, Z', with a mass $M_{Z'} \leq 1$TeV interfering with the Z is predicted to make a detectable distortions to the cross section and forward-backward asymmetry of the process $e^+e^- \to \mu^+\mu^-(n\gamma)$ in the high energy data (Section 2).

There are many published measurements of lepton pair production at LEP, [9, 10, 11, 12, 13, 14, 15, 16, 17, 18, 19]. There is not yet any published measurement of lepton pair production at the highest LEP energy data set, $\sqrt{s} = 183$GeV, which is significant since 60% of the integrated luminosity collected was collected at $\sqrt{s} = 183$GeV.

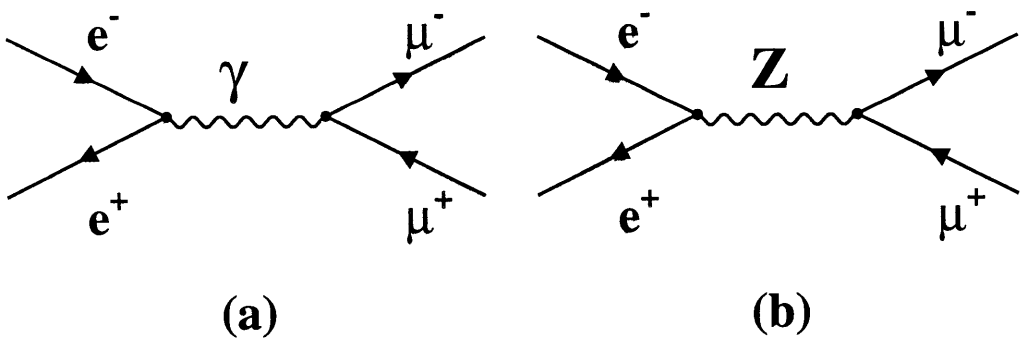

Figure 1: Feynman graphs for the muon-pair production via (a) photon and (b) Z exchange.

2 Theory

One hundred years of experimental work [20, 21] and the corresponding theoretical interpretation has allowed a concise picture of nature to be developed which, in addition to describing all of the experimental data, makes predictions. The next sections discuss the predictions made by the Standard Model of electroweak interactions (Appendix E) for the reaction $e^+e^- \rightarrow \mu^+\mu^-(n\gamma)$. Examples of distortions to the Standard Model predictions stemming from new physics particles are discussed in Sections 2.4.1 and 2.4.2.

2.1 The Born Approximation

The Born approximation consists of taking only the two tree level Feynman diagrams corresponding to Z and to γ exchange (Figure 1) into account and ignoring the infinite number of other higher order diagrams. The tree level Higgs exchange has been neglected due to the predicted small Yukawa coupling to the electron.

2.1.1 Born Cross Section for the Process $e^+e^- \rightarrow \mu^+\mu^-$

The Born level differential cross section,σ^o, of the process $e^+e^- \rightarrow \mu^+\mu^-$is [22]

$$\frac{d\sigma^o}{d\Omega} = \frac{\alpha^2}{4s} N_C^\mu \sqrt{1-\mu_t}\{G_1(s)(1+\cos^2\theta) + G_2(s)\mu_t \sin^2\theta + G_3(s)\sqrt{1-\mu_t}2\cos\theta\}. \quad (1)$$

The angle θ is defined by the incoming e^- and the outgoing μ^- (Figure 2). The invariant mass is denoted by s, the muon mass is denoted by m_μ, and $N_C^\mu = 1$ is the color factor for the muon. The threshold to produce a real muon pair, μ_t, is $\frac{4m_\mu^2}{s}$. The vector and axial couplings, v and a, are

absorbed in the functions

$$\begin{aligned} G_1(s) &= Q_\mu^2 - 2v_e v_\mu Q_\mu \Re|\chi^o(s)| + (v_e^2 + a_e^2)\{v_\mu^2 + a_\mu^2(1-\mu_t)\}|\chi^o(s)|^2 \\ G_2(s) &= Q_\mu^2 - 2v_e v_\mu Q_\mu \Re|\chi^o(s)| + (v_e^2 + a_e^2)v_\mu^2|\chi^o(s)|^2 \\ G_3(s) &= -2a_e a_\mu Q_\mu \Re|\chi^o(s)| + 4v_e a_e v_\mu a_\mu |\chi^o(s)|^2. \end{aligned}$$

Q_μ, the muon charge, is -1. Note that these formulas hold for any fermion simply by replacing the muon charge, mass, and color factor by that of the corresponding fermion. The propagator in the lowest order Breit-Wigner approximation, χ^o, and the Z width, Γ_Z^o, are given by

$$\begin{aligned} \chi^o(s) &= \frac{s}{s - M_Z^2 + iM_Z\Gamma_Z^o} \\ \Gamma_Z^o &= \sum_f N_C^f \frac{\alpha}{3} M_z \sqrt{1-\mu_t}\{v_f^2(1+\frac{\mu_t}{2}) + a_f^2(1-\mu_t)\} \end{aligned}$$

The sum $\sum_f$ is over all energetically allowed fermion pairs, f. After the angular integration of Equation 1, one is left with

$$\sigma^o = \frac{\pi\alpha^2}{2s} N_C^\mu \sqrt{1-\mu_t}\{\frac{8}{3}G_1(s) + \frac{4}{3}G_2(s)\mu_t\}. \tag{2}$$

One can neglect the muon mass and write Equation 2 in terms of the couplings making the QED, interference, and Z terms manifest

$$\begin{aligned} \sigma^o &= \frac{4\pi\alpha^2}{3s}(Q_\mu^2 - 2v_e v_\mu Q_\mu \Re|\chi^o(s)| + (v_e^2 + a_e^2)(v_\mu^2 + a_\mu^2)|\chi^o(s)|^2) \\ &= \{\sigma_\gamma + \sigma_{\gamma Z} + \sigma_Z\}. \end{aligned} \tag{3}$$

For muon pair production above the Z-pole, photon exchange is the dominant contribution to the cross section because $|\chi^o(s)|^2$ behaves as $\approx 1 + 2M_Z^2/s$ above the Z pole and the factor $(v_i^2 + a_i^2)^2$ is equal to 0.12 for leptons in the Standard Model. At the highest energy data point, 183GeV, the ratio of the Z to the photon contribution to the cross section is 0.22. At the lowest energy data point, 130GeV, the ratio of the Z to the photon contribution to the cross section is 0.48.

2.1.2 Born Forward-backward Asymmetry for the Process $e^+e^- \to \mu^+\mu^-$

An $e^+e^- \to \mu^+\mu^-$event, may be classified as either *forward* or *backward* according to whether the projection of the outgoing negatively charged fermion momentum along the beam line is parallel or anti-parallel to the direction of travel of the incident electron (Figure 2). The forward-backward

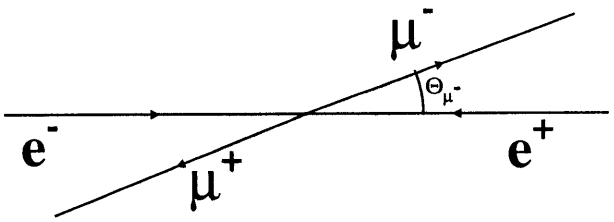

Figure 2: *Forward* muon pair production. Notice that the μ^- polar angle with respect to the e^- beam direction satisfies $\cos(\theta) > 0$.

asymmetry,A^o_{fb}, is then defined in terms of the cross sections of the forward and backward events [23]

$$A^o_{fb}(s) = \frac{\sigma_f - \sigma_b}{\sigma_f + \sigma_b}. \tag{4}$$

where,

$$\begin{aligned} \sigma_f &= 2\pi \int_0^1 d(\cos\theta) \frac{d\sigma}{d\Omega} \\ \sigma_b &= 2\pi \int_{-1}^0 d(\cos\theta) \frac{d\sigma}{d\Omega}. \end{aligned}$$

In the notation of Section 2.1.1, one has

$$A^o_{fb}(s) = \frac{3}{4} \frac{G_3(s)}{G_1(s) + \frac{\mu_t}{2} G_2(s)} \sqrt{1-\mu_t} \tag{5}$$

Ignoring the muon mass and parameterizing the differential cross section in terms of the total cross section (Equation 1) and the forward-backward asymmetry (Equation 5) one has

$$\frac{d\sigma}{d(\cos\theta)} = 2\pi \frac{d\sigma}{d\Omega} = \sigma^o(s)[\frac{3}{8}(1+\cos^2\theta) + A^o_{fb}(s)\cos\theta]. \tag{6}$$

2.2 Radiative Corrections

The Born-level predictions do not describe the data. For precision measurements, higher order contributions must be included. These radiative corrections to the process $e^+e^- \rightarrow \mu^+\mu^-$lead to substantial modifications to σ^o and A^o_{fb}. At energies well above the Z-pole, initial state QED radiation more than doubles the Born cross section. The radiative one-loop corrections can be subdivided into two gauge-invariant subclasses that may be treated independently from one another: 1) electroweak corrections, and 2) pure QED corrections. A detailed description of the radiative corrections can be found in the References [22, 24, 23, 25].

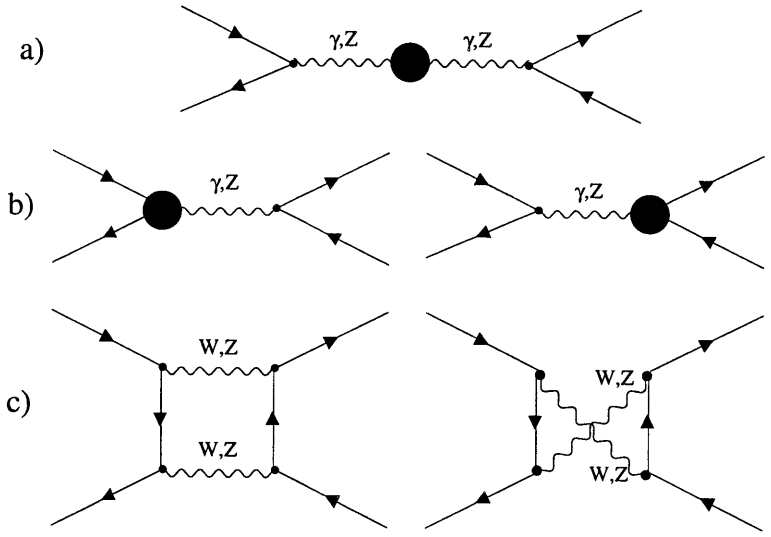

Figure 3: Radiative electroweak corrections to the process $e^+e^- \to \mu^+\mu^-$. a) propagator corrections. b) vertex corrections. c) box corrections.

2.2.1 Electroweak Corrections: The Improved Born Approximation.

The weak corrections collect all non-photonic corrections arising from propagator corrections, vertex corrections, and electroweak box corrections [22]. Vector boson propagator corrections consist of virtual loops of of leptons, quarks, Zs, Ws, or Higgs (Figure 3a). It is these self-energy interactions of the photon which cause the s dependence of the fine structure constant,α

$$\alpha \to \alpha(s) = \frac{\alpha}{1 - \delta\alpha(s)} = \frac{1}{129} \mid_{s=m_Z^2} \tag{7}$$

The self-energy interactions of the Z are parameterized by a s dependence of the Z boson width, Γ_Z

$$\Gamma_Z^o \to \Gamma_Z(s) \approx \Gamma_Z \frac{s}{m_Z^2}. \tag{8}$$

Vertex corrections (Figure 3b), take into account the exchange of particles *other* than photons between the two incoming or the two outgoing fermions plus the fermion self-energy diagrams. The vertex corrections (Figure 3b) can be absorbed by a transformation of the vector and axial-vector couplings, v and a, into effective couplings, $\bar{v}$ and $\bar{a}$.

$$\begin{aligned} \bar{v}_f &= \sqrt{\rho_f(s)} \frac{I_3^f - 2Q_f k_f(s) \sin^2(\theta_W)}{2 \sin\theta_W \cos\theta_W} \\ \bar{a}_f &= \sqrt{\rho_f(s)} \frac{I_3^f}{2 \sin\theta_W \cos\theta_W} \end{aligned} \tag{9}$$

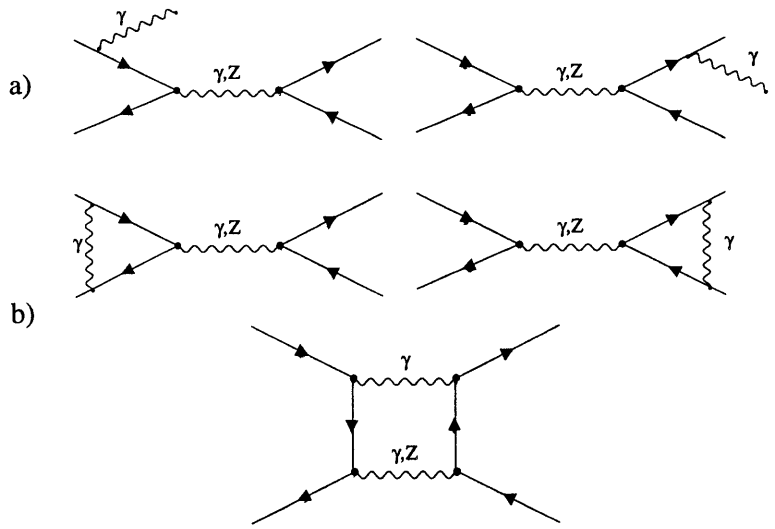

Figure 4: Radiative QED corrections to the process $e^+e^- \to \mu^+\mu^-$. a) emission of ISR and FSR. b) loops with virtual photon.

ρ_f and k_f differ slightly from one in the Standard Model (and their exact value depends on the renormalization scheme [21]), roughly, $\rho_f \approx 1+\rho_t$ and $k_f \approx 1+\rho_t/\tan^2\theta_W$ where $\rho_t = 3G_F m_t^2/8\sqrt{2}\pi^2$ [26] represents the dominant quadratic top quark mass, m_t, dependence.

Electroweak box corrections stem from two heavy bosons being exchanged (Figure 3c). Electroweak box diagrams, which are ignored on the Z-pole, start to have sizable contributions near the W-pair production threshold. They change the Standard Model cross section prediction by nearly 1% [25] at high energies. If the effective couplings were to include the box corrections, an angular dependence would be introduced in the coupling, so, in general, the Standard Model prediction of the box effects is incoherently added to the total cross section prediction [27].

The general structure of the Born approximation described in Section 2.1 still holds if one redefines the variables α, Γ_Z, v, and a to accommodate the weak corrections. The result is called the improved Born approximation. Equations 1 and 5 still hold, but one must remember that the "weak" effects have been absorbed into the couplings.

2.2.2 QED corrections

QED diagrams, involving the emission of bremsstrahlung photons or the exchange of virtual photons in loops (Figure 4), yield finite and gauge invariant contributions to observable processes. Since these corrections depend on the fermion energies and on experimental cuts, they must be calculated for each individual experiment and analysis. The presence of large logarithms of the type $\ln\frac{s}{m_e^2}$ explain the need for QED corrections past first order. Initial state radiation (ISR), final state radiation (FSR) and their interference all have to be considered.

If an ISR photon is emitted, the initial center-of-mass energy, $\sqrt{s}$, is lowered in the annihilation

process to a center-of-mass energy of, $\sqrt{s'}$. Consider the simple case of only one ISR photon with energy E_γ. The $\sqrt{s'}$ value is given by

$$s' = sz = s(1 - \frac{2E_\gamma}{\sqrt{s}}). \tag{10}$$

Using Equation 2, after all of the electroweak corrections sketched in the previous section have been taken into account, the cross section to be compared with experiment is then given by a convolution

$$\sigma^T(s) = \int_{\mu_t}^{1} G(z)\sigma(sz)dz, \tag{11}$$

The QED radiator function, $G(z)$, contains the probability to emit an ISR photon into a reduced center-of-mass energy, $\sqrt{s'}$. The integration ranges over all possible ISR photon energies between the kinematic limit, μ_t, and 1. The same type of convolution integral holds for A_{fb} except the radiator has a non-symmetric term of order $\alpha^2(\ln \frac{s}{m_e^2})^2$ which vanishes in the angular integration [28, 25].

$$\begin{aligned} G(z) &= \beta(1-z)k^{\beta-1}\delta_{S+V} + \delta H(z) \\ \beta &= 2\frac{\alpha}{\pi}e_e^2 \ln(\frac{q^2}{m_e^2}) \end{aligned}$$

δ_{S+V} and $\delta H(z)$ are power series in α and represent the "soft + virtual" and hard corrections, see Reference [29] for details.

2.3 Standard Model Predictions

Although the Born level presentation in Section 2.1 is straightforward, keeping track of the large number of details involved in predicting the effects of the radiative corrections sketched in Section 2.2 is not as easy. There are published and extensively checked FORTRAN computer programs, like KORALZ [30] or ZFITTER [31, 28, 32, 27], that make predictions for the SM observables by calculating the radiative corrections. The programs are periodically updated as the measurement precision and theoretical understanding improves.

2.3.1 Signal

ZFITTER (Figure 5) is used to obtain the Standard Model cross section prediction and forward-backward asymmetry prediction. The differential cross section with respect to $\sqrt{s'}$ is obtained by integrating over the complete polar angle with ZFITTER 5.00 and varying the minimum fermion pair invariant mass cut (Figure 5). The ZFITTER predictions hold only for "ideal detectors" which have no detection inefficiencies; consequently, another program, KORALZ, is used to generate $e^+e^- \to \mu^+\mu^-(n\gamma)$ events which are run through the complete L3 detector so that the number of detected events can be corrected by the efficiency and then compared with theory. Appendix D

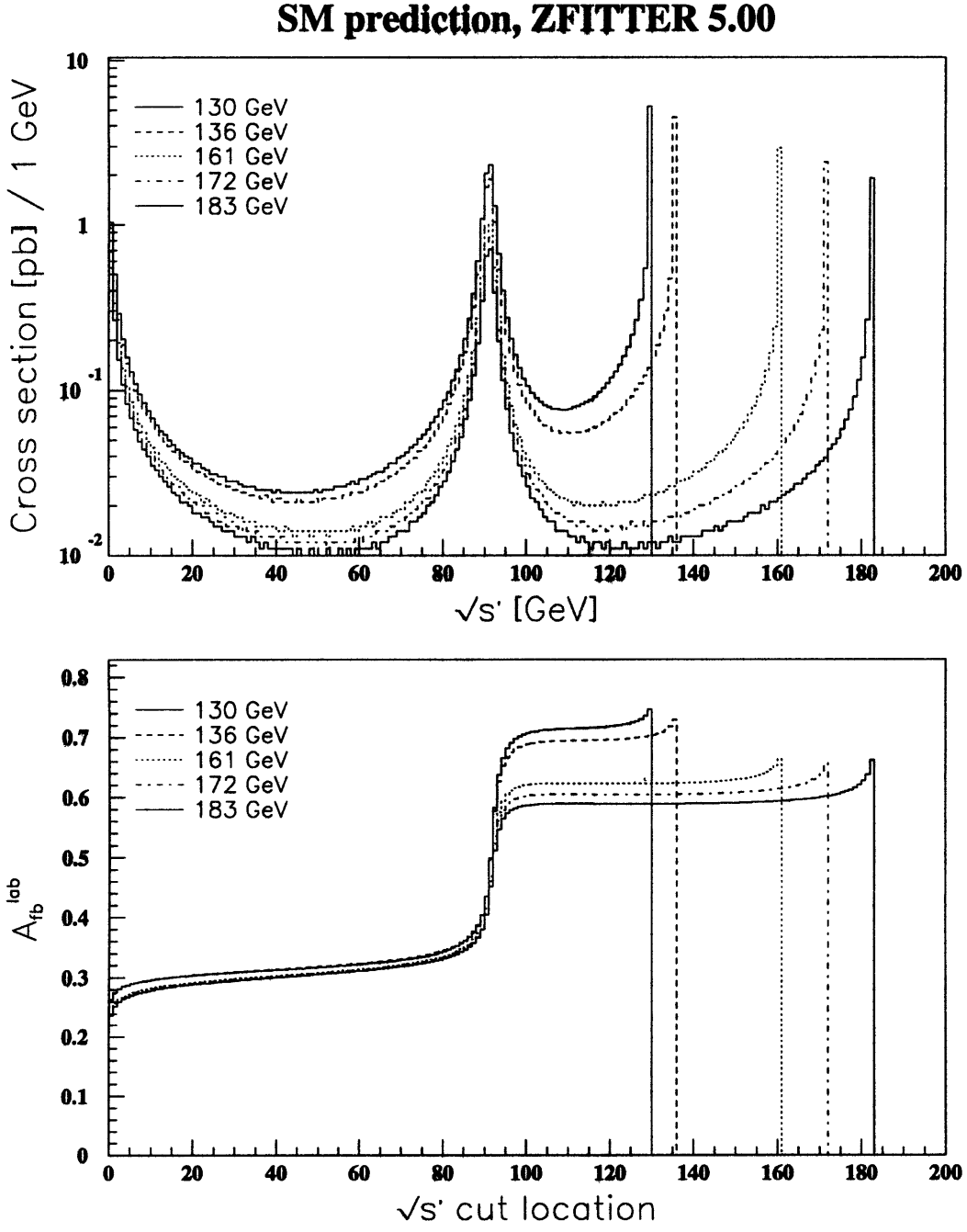

Figure 5: Standard Model prediction of the cross section and forward backward asymmetry at the five data set energies. $\sqrt{s'}$ is defined in the text. The decrease in the cross section and the better separation with respect to the "return to Z" events at higher energy is clearly seen. $A_{fb} \approx 0.3$ below the Z-pole simply reflects the averaging of the high energy events which have a large, positive asymmetry and the Z-pole events which have an asymmetry close to zero.

elaborates on the use of ZFITTER and KORALZ.

As was already mentioned, $\sqrt{s'}$ is the collision energy after initial state radiation. If the incident particles emit an initial state photon which is undetected down the beam pipe, the center of mass of the collision is reduced. The two muons in the final state are still back to back in the phi projection. Experimentally, because the muon momentum is less precisely measured than the muon polar angles, the momentum can be eliminated by using the energy and momentum constraint equations:

$$\begin{aligned} E_\mu^1 \sin\theta_1 &= E_\mu^2 \sin\theta_2 \\ E_\gamma^{ISR} &= |E_\mu^1 \cos\theta_1 + E_\mu^2 \cos\theta_2| \\ E_\gamma^{ISR} &= \sqrt{s} - E_\mu^1 - E_\mu^2, \end{aligned} \tag{12}$$

therefore,

$$E_\gamma^{ISR} = \sqrt{s} \cdot \frac{|\sin(\theta_1+\theta_2)|}{\sin\theta_1 + \sin\theta_2 + |\sin(\theta_1+\theta_2)|}. \tag{13}$$

Clearly, the center of mass of the colliding electron and positron after initial state radiation can be described by the LEP beam energy and the muon polar angles alone:

$$\begin{aligned} s' &= s - 2E_\gamma^{ISR}\sqrt{s} \\ s' &= s \cdot \frac{\sin\theta_1 + \sin\theta_2 - |\sin(\theta_1+\theta_2)|}{\sin\theta_1 + \sin\theta_2 + |\sin(\theta_1+\theta_2)|} \end{aligned}$$

Of course, the relation only holds exactly when the muons do not radiate, when only a single initial state radiation photon is emitted collinear with the beam, and when interference between initial and final state radiation is ignored. The bias in the algorithm, i.e. events with a small $\sqrt{s'}$ which nevertheless pass the $\sqrt{s'}$ cut, is determined from Monte Carlo and is subtracted from the number of candidate events (Table 7).

2.3.2 Backgrounds

The three principal physics backgrounds (Figure 6) to $e^+e^- \to \mu^+\mu^-(n\gamma)$ are the multiperipheral ("two-photon") background, the WW background, and the $\tau^+\tau^-(\gamma)$ background. The Monte Carlo technique is used to subtract an estimated number of background events from the event candidates. The number of generated SM background events (Table 1) is approximately a factor of 10 more than is expected from the data set luminosity. The SM Monte Carlo cross sections of the generated event sets are seen in Table 2. The background contaminations at the nominal set of analysis cuts can be found in Table 7. Further information about the use of Monte Carlo programs can be found in Appendix D.

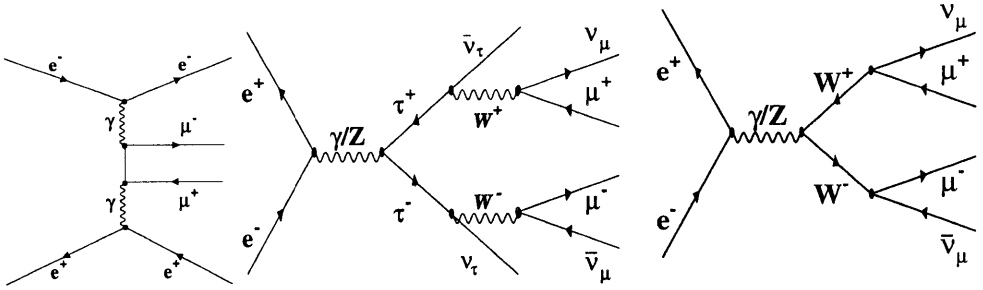

Figure 6: The three principal backgrounds to $e^+e^- \to \mu^+\mu^-$.

# generated, simulated, and reconstructed MC							
$\sqrt{s}$	Eff. calc.	Background calculation					
	$\mu^+\mu^-(n\gamma)$	$\tau^+\tau^-(\gamma)$	$W^+W^-(n\gamma)$	$e^+e^-\mu^+\mu^-$	q^+q^-	ZZ	Ze^+e^-
130	4991	5000	3000	30000	8714	5000	5000
136	4986	4992	6000	20000	19925	5000	5000
161	50000	50000	29832	99000	197995	4945	15874
172	49831	49820	49305	98918	143632	9944	22849
183	99572	100000	243927	98922	376983	29625	26754

Table 1: Generated Monte Carlo event statistics.

The two photon cross section is fifty times as large as the $e^+e^- \to \mu^+\mu^-(n\gamma)$ signal, yet even a weak momentum cut reduces its background contribution to the few percent level (Section 4). Bias in the $\sqrt{s'}$ calculation is the origin of two photon events which leak into the candidate events. Were one able to measure the momenta of muons with small polar angles as precisely as they are measured in the barrel muon spectrometer, the two photon background would be eliminated.

The WW cross section becomes large above threshold but the 10% branching ratio to muons [1] and the relatively small boost of the W at LEP2 means the WW background is readily identified by acollinear muon pairs (Figure 20).

Due to the extreme boost of the taus, when both taus decay to muons, the background is to a large extent irreducible without tight momentum cuts. Given the 17% branching ratio of the tau to muons and the observed lepton universality, a few percent tau background is unavoidable when loose selection cuts are used.

In the highest energy data at our nominal set of analysis cuts, the sum of all other physics backgrounds does not approach the contribution of any of the three just mentioned. Non-physics backgrounds, like cosmic rays and bias in the $\sqrt{s'}$ algorithm, are also accounted for.

[1] Of course $W \to \tau \to \mu$ also contributes.

MC SM cross section of generated events, $\sigma_{MC}(pb)$						
$\sqrt{s}$	Background calculation					
	$\tau^+\tau^-(\gamma)$	$W^+W^-(n\gamma)$	$e^+e^-\mu^+\mu^-$	q^+q^-	ZZ	Ze^+e^-
130	22.63	.07	577.7	326.1	.50	2.06
136	20.10	.11	548.0	266.0	.47	2.13
161	12.57	3.26	498.9	146.4	.43	2.52
172	10.40	12.22	676.4	121.2	.42	2.67
183	8.65	15.57	604.8	108.3	.59	3.26

Table 2: The SM background MC cross sections of the generated event sets. Jumps in the $e^+e^-\mu^+\mu^-$ cross section were caused by changes in the low Q^2 cuts. The $e^+e^-\mu^+\mu^-$ background to the $\mu^+\mu^-(n\gamma)$ signal was not affected, as seen by the smooth increase in the $e^+e^-\mu^+\mu^-$ background with increasing $\sqrt{s}$ in Table 7.

2.4 New Particle Searches

Theoretical ideas which attempt to extend the Standard Model can be tested and constrained using the measured $e^+e^- \to \mu^+\mu^-(n\gamma)$ cross section and forward-backward asymmetry (Section 4). Two very simple examples follow which could affect the $e^+e^- \to \mu^+\mu^-(n\gamma)$ cross section and asymmetry.

2.4.1 Heavy Gauge Bosons

Additional neutral, heavy gauge bosons, Z', are predicted in many theories which attempt to extend the Standard Model; for example, left-right symmetric models [33], which attempt to explain low energy parity violation, predict right handed charged currents and an additional Z boson. E_6 GUT theories also allow additional gauge bosons [34]. Some recent theoretical predictions state that in Super String and Super Gravity models, the lightest Z' boson is most naturally found in the 200GeV to 1TeV range [35].

The CDF limit on the Z' boson mass, assuming Standard Model couplings, is 690GeV from a direct search of electron and muon pair production [36]. It should be mentioned, however, that the largest observed CDF muon pair invariant mass is 320GeV, and besides the Standard Model coupling assumption, they assume a parton distribution function, for which they choose the Martin-Roberts-Stirling set D'_- [37].

Unlike hadron colliders which rely on direct production and leptonic decay of a hypothetical Z', e^+e^-machines can search by looking for small deviations from Standard Model predictions due to propagator effects. In the presence of a Z', Equation 3 would be modified to

$$\sigma = \sigma_\gamma + \sigma_{\gamma Z} + \sigma_Z + \sigma_{Z'} + \sigma_{\gamma Z'} + \sigma_{ZZ'}. \tag{14}$$

Even if $\sigma_{Z'}$ is small, the experimental consequence of the two additional interference terms, $\sigma_{\gamma Z'}$ and $\sigma_{ZZ'}$ would be to distort the cross section and forward backward asymmetry from its Standard

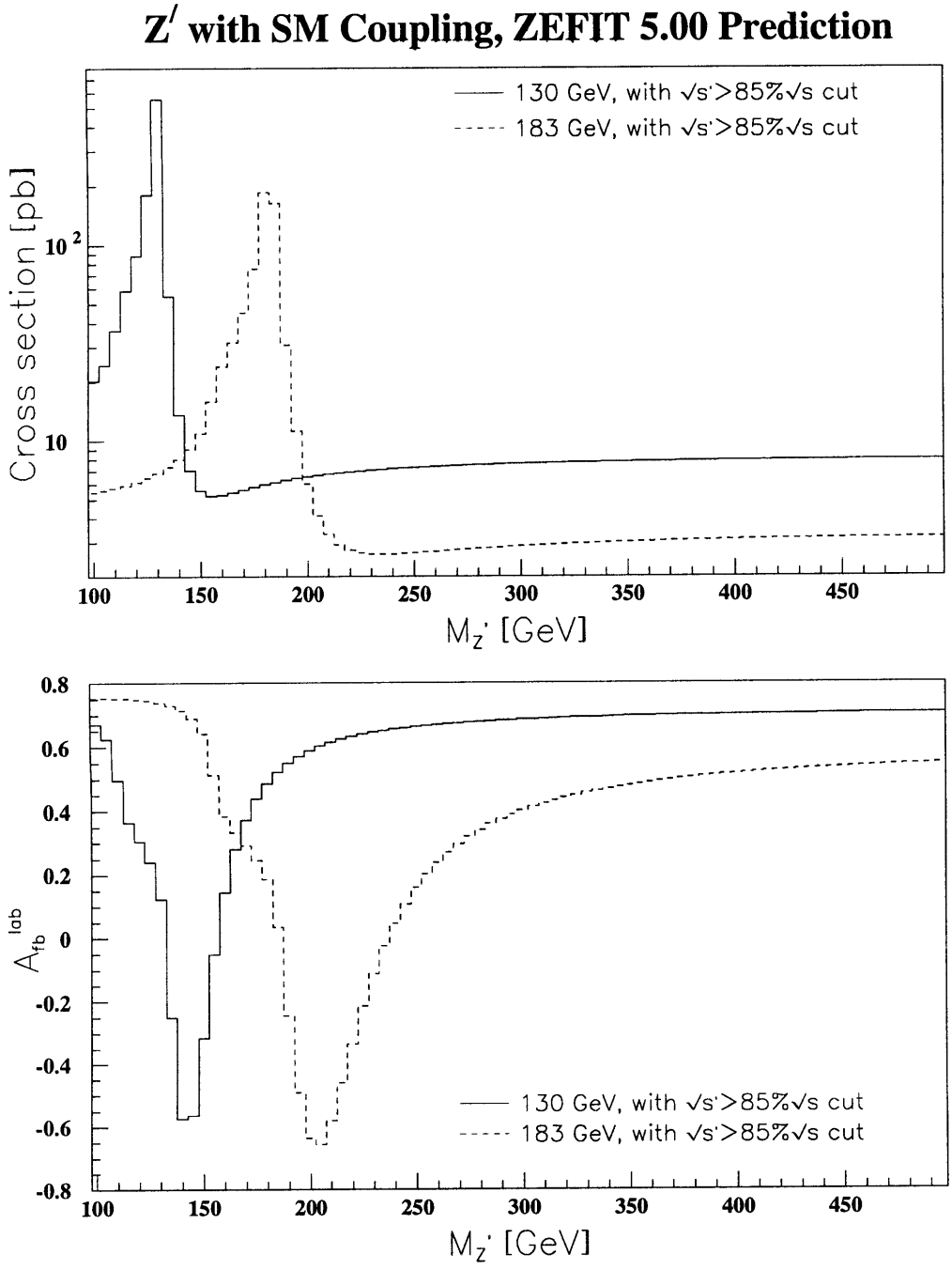

Figure 7: The predicted cross section and forward-backward asymmetry at fixed center of mass energies 130GeV and 183GeV versus the Z' mass in a simple model in which the Z' has the *same* coupling to leptons as the Standard Model Z boson. The bumps at $85\%\sqrt{s}$ are artifacts of the experimental $\sqrt{s'} > 85\%\sqrt{s}$ cut. Further, such a low mass Z' is already ruled out by LEP1 data alone [21]).

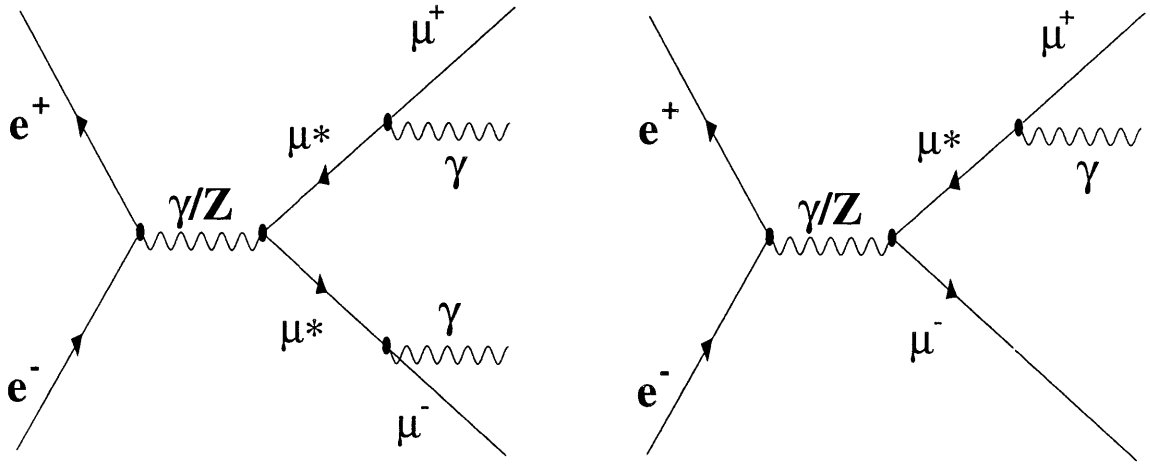

Figure 8: Examples of excited muon production and subsequent photon de-excitation.

Model prediction. Because the new terms all have factors $\propto \frac{coupling}{s-M_{Z'}^2}$, one can not separate between very small coupling and a very large Z' mass without specifying a model.

Assuming the Z' coupling to leptons to be the same as the Standard Model Z boson (Figure 7), for example, the cross section and asymmetry can be predicted. In Figure 7, the program ZEFIT [38] version 5.00 was used. As M_Z' is increased, σ and A_{fb} approach asymptotically their SM values. Notice how the effects of a low mass Z' are large and easy to verify experimentally, especially in the simple model here described in which the width of the Z', $\Gamma_{Z'}$, scales as $\Gamma_Z \times (M_{Z'}/M_Z)$.

2.4.2 Excited Leptons

Compositeness is one possibility to explain the number of fermion generations and the fermion mass spectrum [39]. If fermions are composite, they can be excited, so one should check the muon-photon invariant mass spectrum for structure. Excited lepton production (Figure 8) would show up as a bump in the muon-photon invariant mass spectrum. A search has been conducted for structure or an excess in the muon-photon invariant mass spectrum, $M_{\mu\gamma}$, with respect to the Standard Model ISR and FSR background in the 183GeV data set (Section 4).

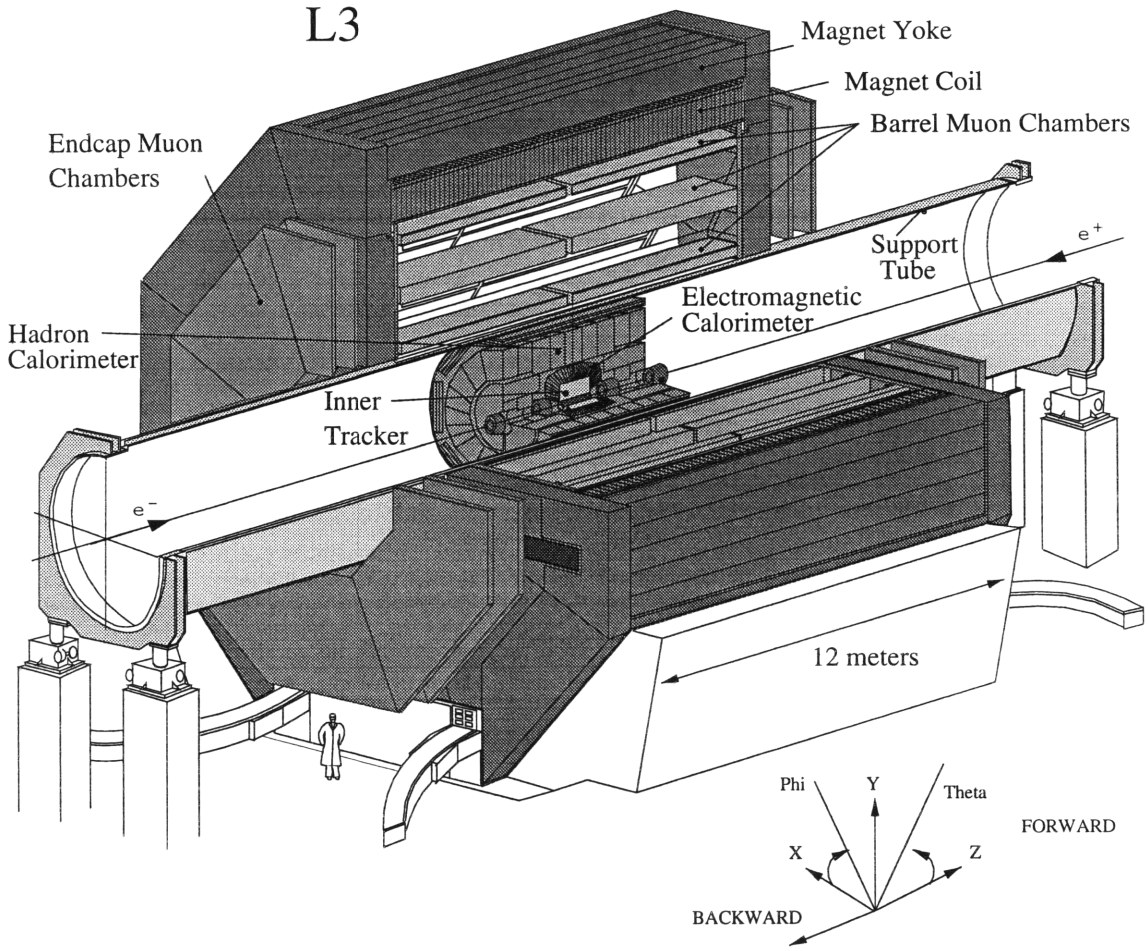

Figure 9: Perspective view of the L3 detector. Coordinate system convention defined.

3 The L3 Detector

The L3 detector [1, 2] was used to collect the candidate $e^+e^- \to \mu^+\mu^-(n\gamma)$ events for the present analysis. The L3 detector (Figures 9 and 10) is located at the center of one of the four straight sections of the Large Electron Positron collider (LEP) [3, 4]. LEP is a 27km long synchrotron accelerator storage ring located 50m underground at the CERN laboratory near Geneva, Switzerland. The accelerator is capable of stably colliding bunches of electrons against bunches of positrons in the center of the L3 detector. The nominal bunch crossing rate is 45kHz and typical luminosities are of the order $10^{31}cm^{-2}s^{-1}$.

To calibrate oneself to the huge size of the L3 detector, there are 60000 signal wires in the muon detectors alone. The detector was built to study the physics of e^+e^-collisions at center of mass energies of up to 200GeV. The design emphasizes precise measurement of electron, photon, muon,

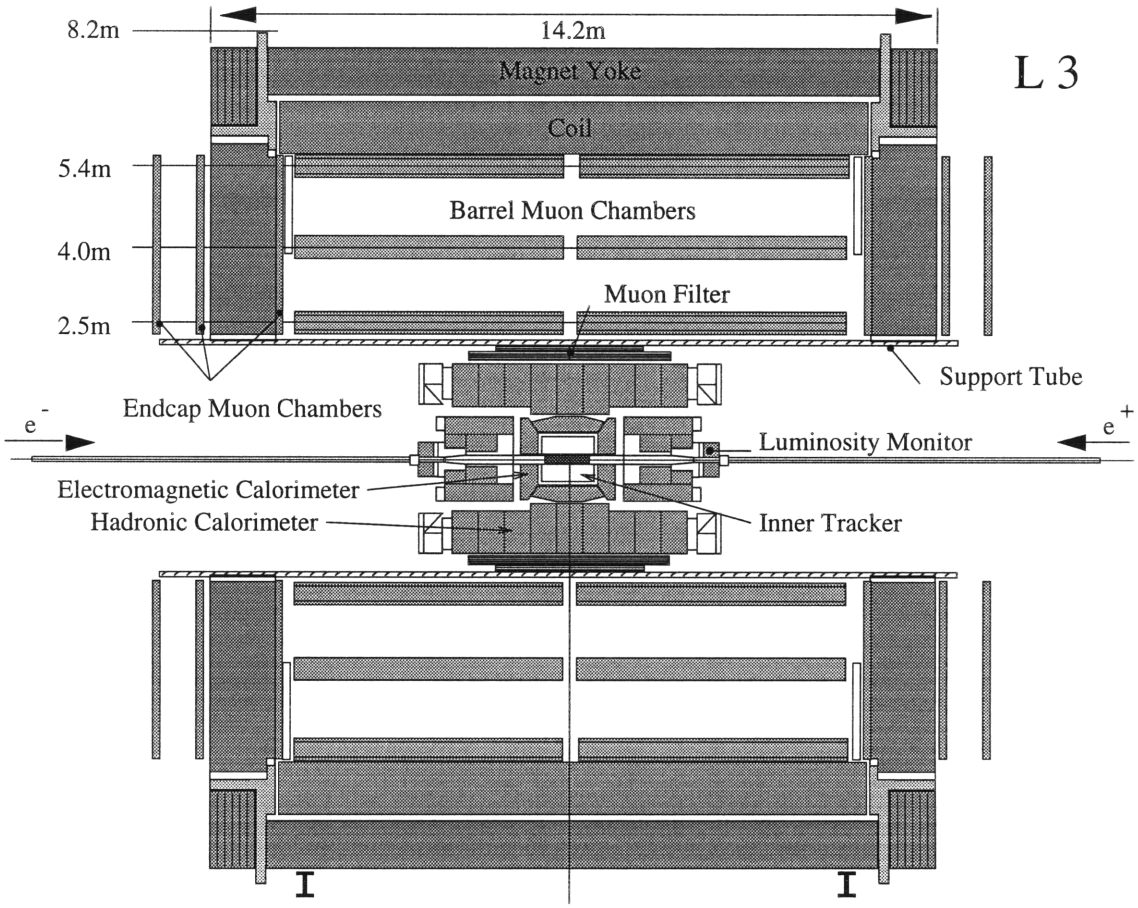

Figure 10: Side view of the L3 detector.

and jet energy and direction. Historically, the design was optimized to search with high resolution for $\mu\mu$ and ee, for top quark toponium spectroscopy, and for missing mass searches including the Higgs.

All of the L3 sub-detectors, except the endcap muon spectrometers, are supported by a 32m long 4.45m diameter stainless steel tube, called the support tube (Figure 10)). The support tube is attached to precision jacks at its ends making it independent from the solenoid which allows for precise positioning of the L3 sub-detectors with respect to the e^+e^-beams. The central, or barrel, muon spectrometer is attached to the outside of the support tube; the transverse lever arm for analysis in the 0.5T magnetic field is 2.9m. Housed inside the support tube at concentrically smaller radii (Figure 15), one has: a hadron calorimeter ($3.5\Lambda_{\rm int}$, R=75cm), scintillation counters (R=75cm), an electromagnetic calorimeter ($24X_o$, R=50cm), an inner tracking chamber with 40cm lever arm, and a silicon micro-vertex detector (R=10cm).

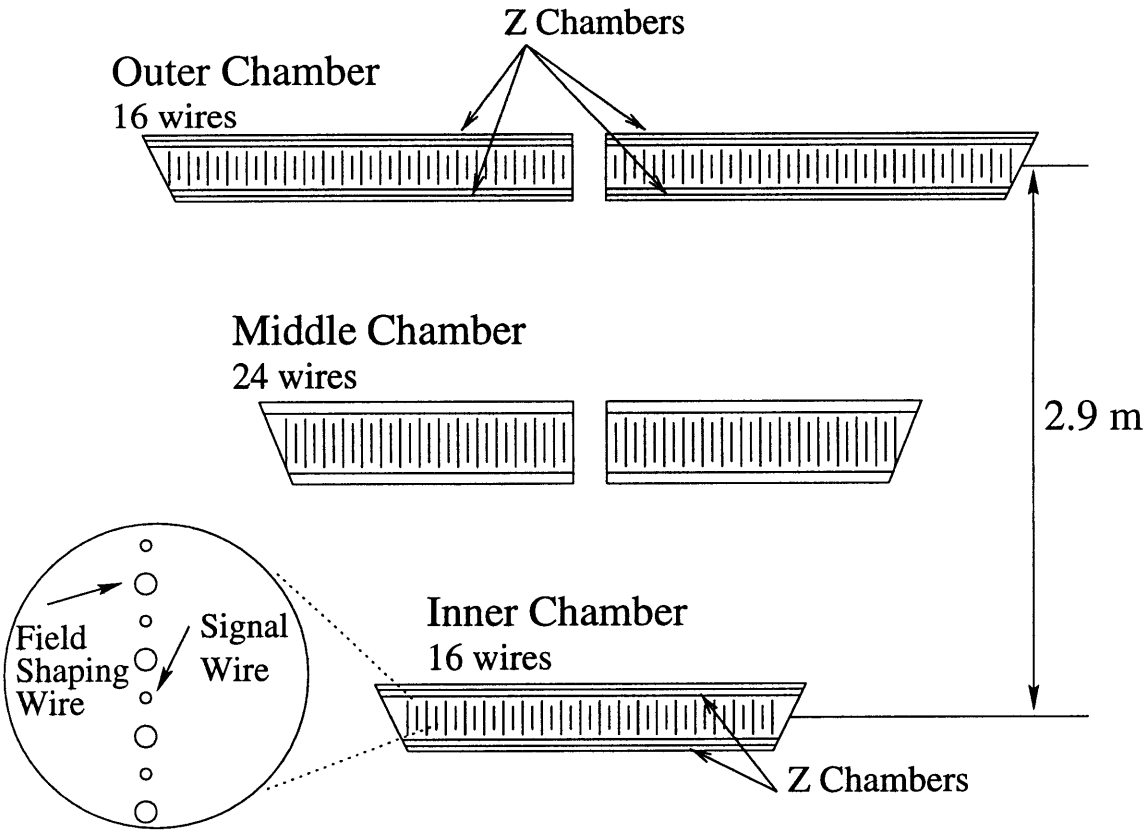

Figure 11: Side view of a barrel muon chamber octant showing the five P chambers' cell layout and the six z chamber positions. Blowup of the cell's signal wire plane is not to scale.

3.1 Magnet

The large solenoid coil (Figure 10) is driven with 30,380 amps to provide a 0.5T magnetic field along the beam line. In addition, the iron doors have been magnetized by toroidal coils driven with 6300 amps to yield a 1.2T magnetic field. The field inside the solenoid is measured by magnetoresistors, Hall probes, and NMR probes; then, the measurements are fit to an analytical model [48]. The toroid field is measured by induction loops. The field shape is taken from a 3-D computer program [49, 50].

3.2 Muon Spectrometer

The barrel muon detector [51, 52, 53] (Figures 11 and 12) is made of large drift chambers mechanically attached together on a low weight frame. The chamber pattern (Figure 11) is repeated 16 times, 8 on the forward L3 half and 8 on the backward L3 half. The detector samples the ionization trail of a high energy charged particle originating from the interaction point at angles of $|\cos(\theta)| < .707$ up to 64 times. 8 times for the Z coordinate and 56 times for the "radial" coordinate. The details of the algorithm which converts the drift chamber's digitally registers timing signals into muon candidate's momentum is quite complicated and is discussed in Section 3.9.1.

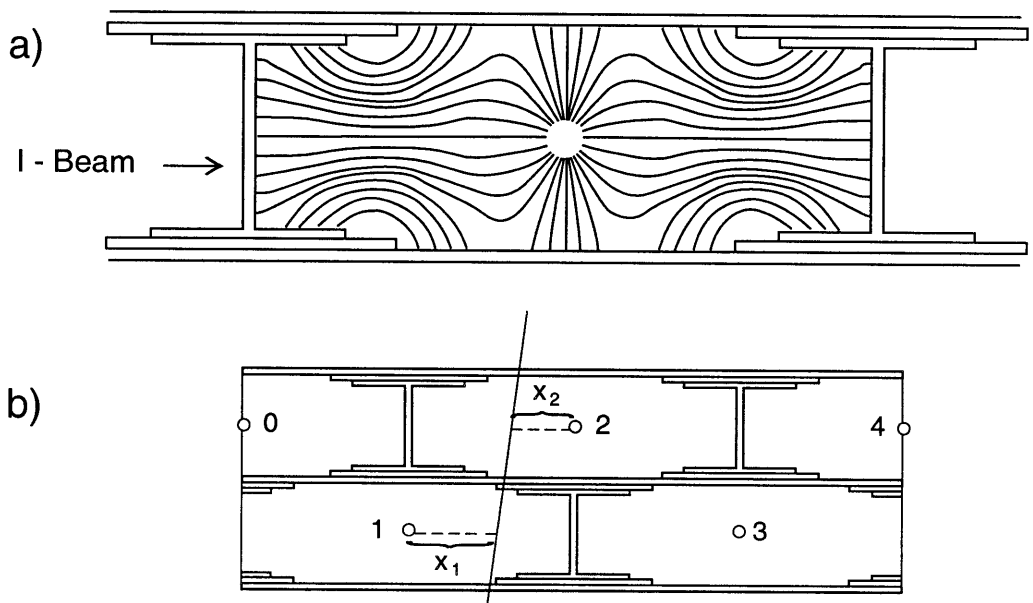

Figure 12: a) Cross section of a barrel muon Z chamber cell showing the I-beam structure and electric field map in absence of a magnetic field. b) Principle of the coordinate measurement.

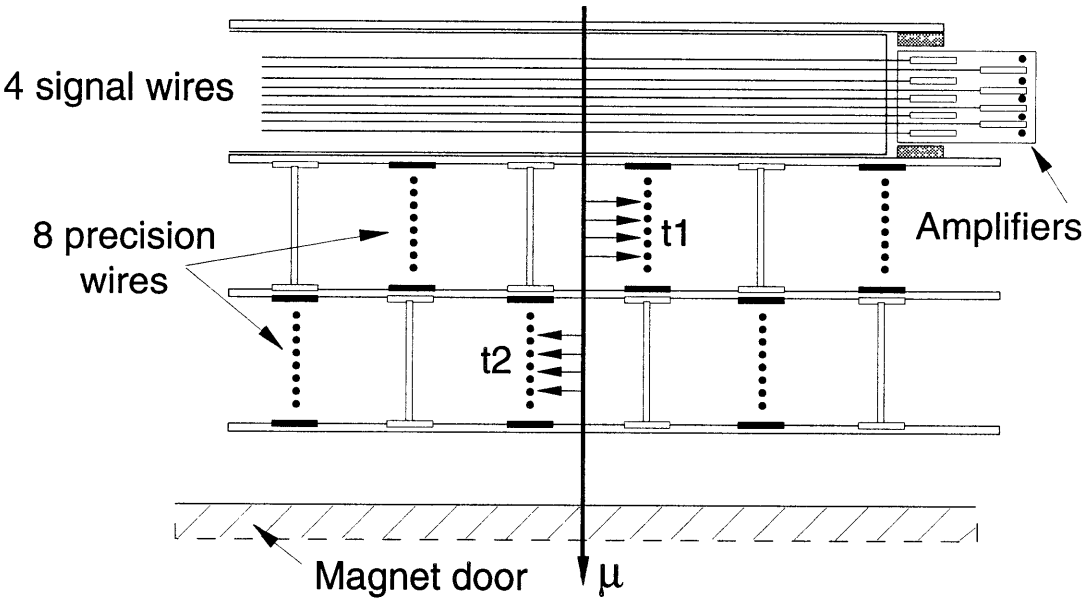

Figure 13: Slice of one of the endcap muon chambers showing the cell structure and the measurement principle. The chambers are self calibrating, for $t1 + t2 = C$.

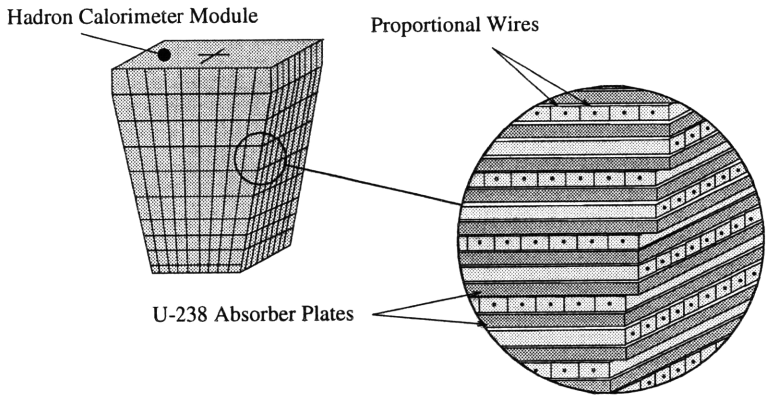

Figure 14: Hadron calorimeter module. Note how layers alternate to provide Z and ϕ coordinates. Wires of many parallel layers are hooked together into a tower structure.

The endcap (forward-backward) muon detector [49] (Figure 13) samples the ionization trail of a high energy particle originating from the interaction point at angles of $.809 < |\cos(\theta)| < .914$ up to 36 times. Over the complete solid angle of the endcap muon detectors, there is overlap with at least one layer of the barrel muon detector. Resistive plate chambers [54, 55, 56] are attached to the endcap muon chambers and are used for triggering.

3.3 Hadron Calorimeter

The L3 hadron calorimeter [57] is designed for measuring jet energies; nevertheless, it can be used to measure a minimum ionizing particle's 2.5GeV energy loss signal with 50% energy resolution. Muons which pass through detection gaps in the muon spectrometers can be recovered, notably at 90 degrees (Figure 10). Proportional counters are sandwiched between the uranium and brass absorber plates to form a hadron calorimeter module (Figure 14). A charged particle's ionization trail is sampled up to 60 times in the hadron calorimeter. Coarse granularity, Uranium decay noise, and a lack of projective geometry in the Z direction complicate tracking. The muon filter, brass absorber plates interspersed with proportional tubes located directly behind the hadron calorimeter, is not used in this analysis.

3.4 Scintillation Counters

The 30 barrel scintillators [58] (Figure 15) are located directly inside of the hadron calorimeter and cover the region $|\cos\theta| < 0.83$. The 32 endcap scintillators extend coverage down to $|\cos\theta| < 0.985$. The time of flight corrected scintillator times are used to reject cosmic rays. The high level of hadron calorimeter Uranium activity is reduced by gating the scintillator signals with narrow windows around the beam crossing.

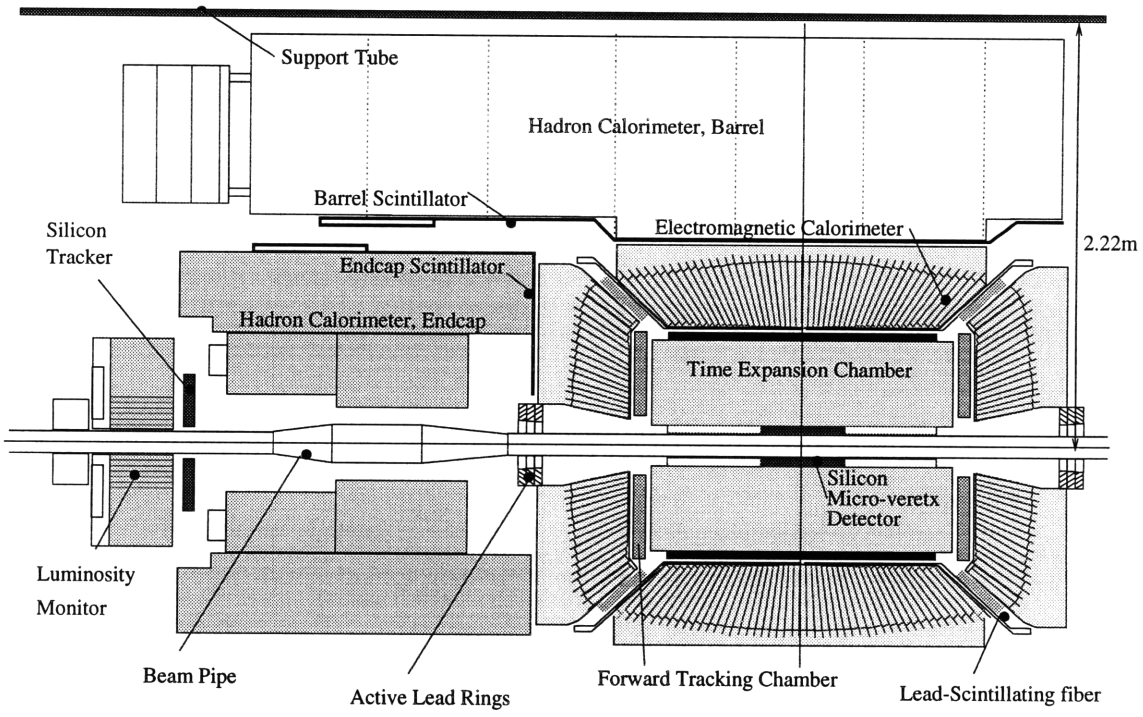

Figure 15: Block diagram of the sub-detectors inside the support tube.

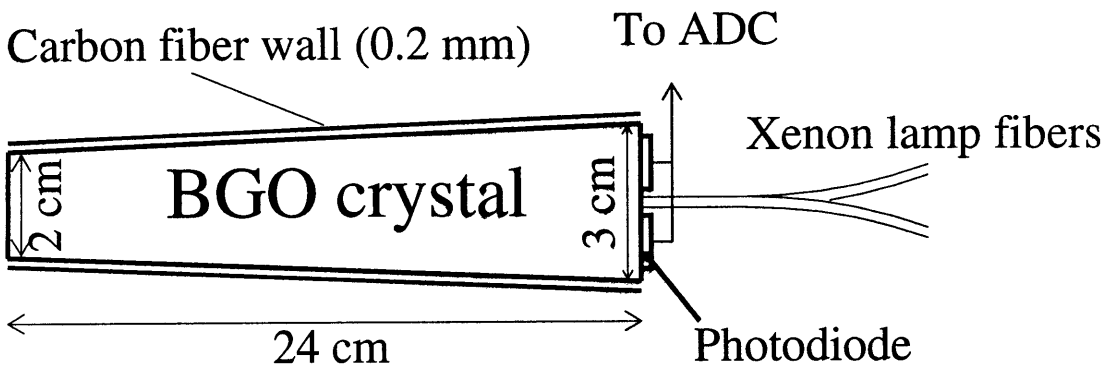

Figure 16: A bismuth germanium oxide (BGO) crystal of the electromagnetic calorimeter.

3.5 Electromagnetic Calorimeter

The electromagnetic calorimeter [59] is made of bismuth germanium oxide crystals (Figure 16). The crystals are 24 radiation lengths thick and have transverse dimensions close to the Molière radius. The signals of well isolated photons, minimum ionizing particles, and hadrons are easily discriminated from one another. The electromagnetic calorimeter is used to measure photons and as a backup to the muon chambers in the analysis.

3.6 Inner Tracker

Tracking for the vertex reconstruction is done by a Time Expansion Chamber (TEC) [60] which gives up to 62 tracking points in the $r\phi$ plane for r between 10 and 45 cm. Figure 17 shows the $r\phi$ projection of one inner and two outer sectors. The high amplification region at the sense wire plane is separated from the low field drift region by a grid wire plane. The level arm is not large enough to make an accurate momentum estimation at high energies, but it does provide accurate polar angles. Ghost track ambiguities are eliminated by matching across inner and outer sectors. A Silicon Microvertex Detector (SMD) [61] provides up to four points close to the interaction point, two in the $r\phi$ plane and two the z direction (Figure 15). Up to four points along z are obtained by the induced signals on cathode strips [62].

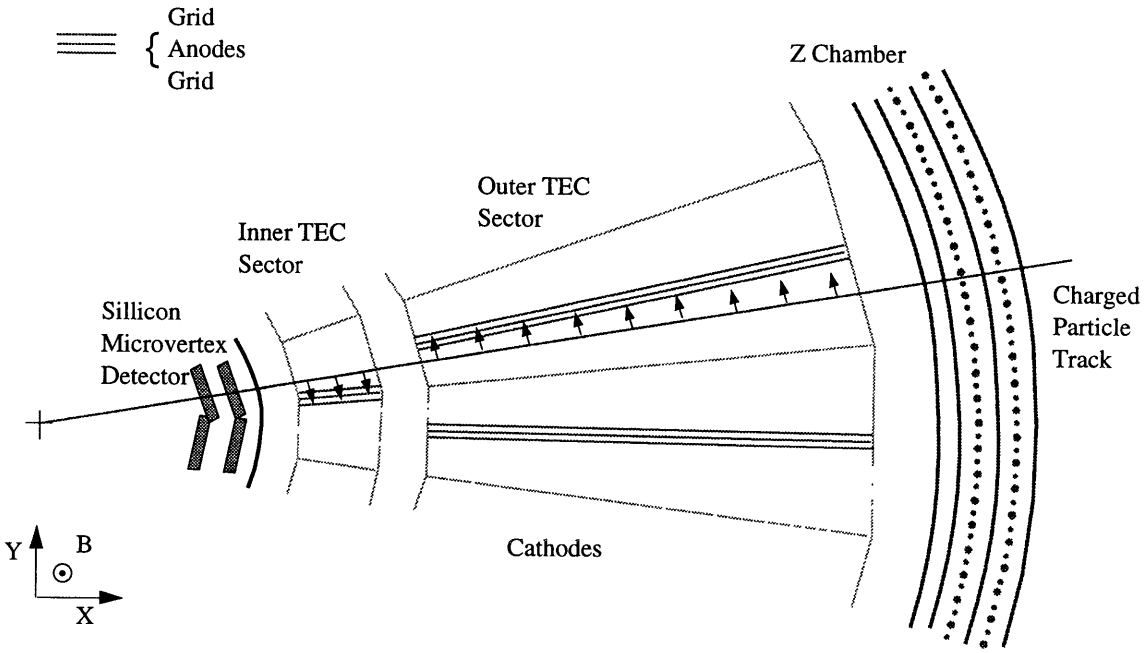

Figure 17: Cell structure of the inner tracker, Time Expansion Chamber (TEC).

3.7 Luminosity Monitor

The luminosity monitor [63](Figure 15) is made of BGO crystals and covers the polar angle range 24.93mrad $< \theta <$ 69.94mrad. It measures the rate of Bhabba events [64] which are strongly peaked at small polar angles. Since the Bhabba cross section is know to 0.3% [65], the rate is used to calibrate the luminosity delivered to L3 by LEP with high precision. The luminosity is determined independently from the present analysis [63].

3.8 Trigger

At LEP, there is a beam crossing every 22μs, i.e. 45,000 times a second. At nominal beam collision luminosities, an interesting physics event occurs only once every few seconds. Based on general physics hypotheses, one can construct an algorithm using fast, but low resolution detector information which rejects detector noise, beam-gas collisions, beam-wall collisions, cosmic ray radiation, empty events, but accepts all physics events. The hardware implementation of the algorithm constitutes the "trigger." In the case of a positive trigger, the event is permanently stored. There are, in fact, three levels of trigger at L3 which use progressively higher resolution sub-detector data to decide if an event should be permanently stored.

Event candidate trigger efficiencies		
level 1	99.7%	± .1%
level 1 muon	96.5%	± .8%
level 1 backup	92.7%	± 1.1%
level 2	100.0%	± .0%
level 3	100.0%	± .0%
level 3 muon	98.4%	± .5%
level 3 backup	99.8%	± .2%

Table 3: Trigger efficiencies calculated from $e^+e^- \to \mu^+\mu^-(n\gamma)$ candidate data events having at least one selected muon candiate in the muon chambers. Uncorrelated trigger approximation used (Appendix B).

3.8.1 Level 1

The first level of trigger decides if an event is interesting at every beam crossing. Upon a level 1 trigger, readout of the entire detector begins. There are five general types of level 1 trigger (which are themselves the logical OR of several sub-trigger decisions) [66, 67, 68, 69, 70, 71, 72]:

- Muon chamber trigger (Appendix C).
- Inner tracker trigger [2].
- Calorimetric energy trigger.
- Barrel scintillator multiplicity trigger.
- Luminosity monitor trigger.

The level 1 muon chamber trigger and the level 1 inner tracker trigger are redundant triggers for $e^+e^- \to \mu^+\mu^-(n\gamma)$ events, enabling internal cross checks. For events with hard ISR or FSR and for events with large muon energy loss in the hadron calorimeter, the energy trigger overlaps with the muon chamber trigger and the inner tracker trigger. The logical OR of the inner tracker trigger and the energy trigger are used as the the backup trigger to the muon chamber trigger to estimate the $e^+e^- \to \mu^+\mu^-(n\gamma)$ trigger selection efficiency. The detector acceptance and trigger efficiencies are kept uncorrelated using the technique described in Appendix B. The results are listed in Table 3.

The actual trigger algorithm for the muon chambers is easy to explain (Appendix C). Every possible hit cell track pattern in the muon chambers (or RPC hit strip track pattern in the endcap) with momentum greater than 2GeV which could have a production vertex originating anywhere inside the inner tracker is allowed to be a muon candidate and is triggered on. The hit wire per cell

[2]The "inner sector sub-trigger", a new type of inner tracker trigger, was installed for 1997 data taking, and could serve as a backup to the endcap muon trigger. It was only sporadically enabled in 1997; consequently, it is ignored in the trigger efficiency studies. Note: no selected event candidate has only the inner sector trigger bit set.

threshold and the required hit chamber layers are set as low as possible to maximize the detector fiducial volume, while at the same time keeping noise triggers to a minimum. There are two types of level 1 muon chamber triggers, the endcap muon triggers and the "barrel muon $\times$ barrel scintillator hit" triggers. The barrel scintillator hit trigger algorithm is straightforward: if any of the 30 barrel counters has a hit within $\pm$30ns around the beam crossing, there is a scintillator hit trigger. The scintillator hit accompanying the barrel muon trigger reduces the cosmic ray rate by a factor 10.

3.8.2 Level 2

The level 2 rejection algorithm [73] is a software trigger which has access to the detailed trigger data. It is only allowed to reject events which have one and only one level 1 trigger fired. Care is taken to reject only obvious noise events to ensure that the redundancy of the level 1 triggers is maintained.

The exact level 2 barrel muon trigger rejection algorithm is as follows: if the database indicates there is a problem with the inner tracker high voltage, the event is automatically accepted. If there is a triggered barrel octant in the horizontal position, the event is accepted. If there is no triggered octant in the horizontal position, then there must be a hit scintillator in front of at least one of the triggered octants or there must be 9 or more hit trigger wires anywhere in the outer sectors of the inner tracker. The author successfully convinced the L3 collaboration to remove the endcap muon trigger level 2 rejection algorithm. The level 1 endcap muon sub-triggers are already two-fold coincidence; the level 2 three-fold coincidence algorithm would generate inefficiencies.

Level 2 rejects 50% of the level 1 muon chamber triggered events. So that one may cross check that the level 2 trigger is not generating inefficiencies, one in every twenty level 1 barrel muon triggers rejected by level 2 is permanently stored. No selected events (Section 4) have the level 2 rejection bit set, i.e. 100% efficiency, Table 3.

3.8.3 Level 3

In the final level of trigger, level 3, a rough event reconstruction is made, and the timing constraints are tightened. An additional 50% of the events triggered by the muon chambers are rejected, yet one in every twenty level 3 events rejected by level 3 is kept in order to cross check that level 3 is not generating any inefficiencies. No selected events (Section 4) have the level 3 rejection bit set.

The level 3 muon rejection algorithm [74] was modified in 1995 [75] after the the addition of the endcap muon chambers, the endcap scintillators, and the RPCs. The new algorithm uses the timing data from the muon chambers instead of the trigger data and makes a track pattern search in the same spirit as the level 1 muon triggers. The phi granularity in the track pattern search is increased in the endcap muon chamber with respect to the level 1 search. Strict timing cuts on the scintillator and the RPC hits are also applied. All possible track patterns are searched using the hadron calorimeter hits as a backup; Table 3 shows how level 3 is able to "recover" muon triggers

using the hadron calorimeter information.

3.9 Event Reconstruction

The data structures [76] and calibrations [77, 9, 78, 79, 80, 55, 81, 82, 83, 84] used for the event reconstruction have been described elsewhere. The reconstruction algorithms are briefly described.

3.9.1 Muon Chambers

In the muon chambers (Figures 11, 12, and 13), digitized timing hits are converted into spatial coordinates based on the chamber wire's positions (i.e. precision alignment) and cell map functions. A cell map function is a function which returns a distance from the signal wire plane given a time. The electric field in the drift cell, the effects of the magnetic field map [85], properties of the chamber gas mixture [86], known timing delays, ambient pressure, and temperature are all embedded within the cell map function [87].

Spatially close hit coordinates in a chamber are joined together to form track segments. The segments are fit to a straight line. The slope and the line intersection with the midpoint of the chamber are used to match to other chamber layers. Attached segments in the $r - \phi$ projection make track candidates with $charge \cdot momentum$ and phi estimates. Attached segments in the z projection make track candidates with a θ estimate. The track candidate in the two segment projections are then joined together to form all possible track candidates. Tracks are then re-fitted more realistically. Because of multiple scattering and the complicated magnetic field map, one can not just fit a helix to the hit wires' coordinates [88]. Photo-nuclear interactions in the hadron calorimeter, hard knock-on electrons, and cosmic ray background occasionally make track finding difficult in the muon chambers. The mean energy loss of a minimum ionizing particle traversing the calorimeters is added to the momentum measured in the muon chambers to make the muon momentum estimate at the interaction point.

3.9.2 Hadron Calorimeter

ADCs register the amplified signal originating from the proportional tubes sandwiched between the Uranium plates. A conversion constant converts the ADC value into an energy. The energy and number of hits along a predefined set of track patterns is checked and minimum ionizing track candidates are made. Since the granularity of the calorimeter is optimized for hadronic energy measurement and not for tracking, one has to rely on other detectors to reduce the "ghost" track candidate ambiguities.

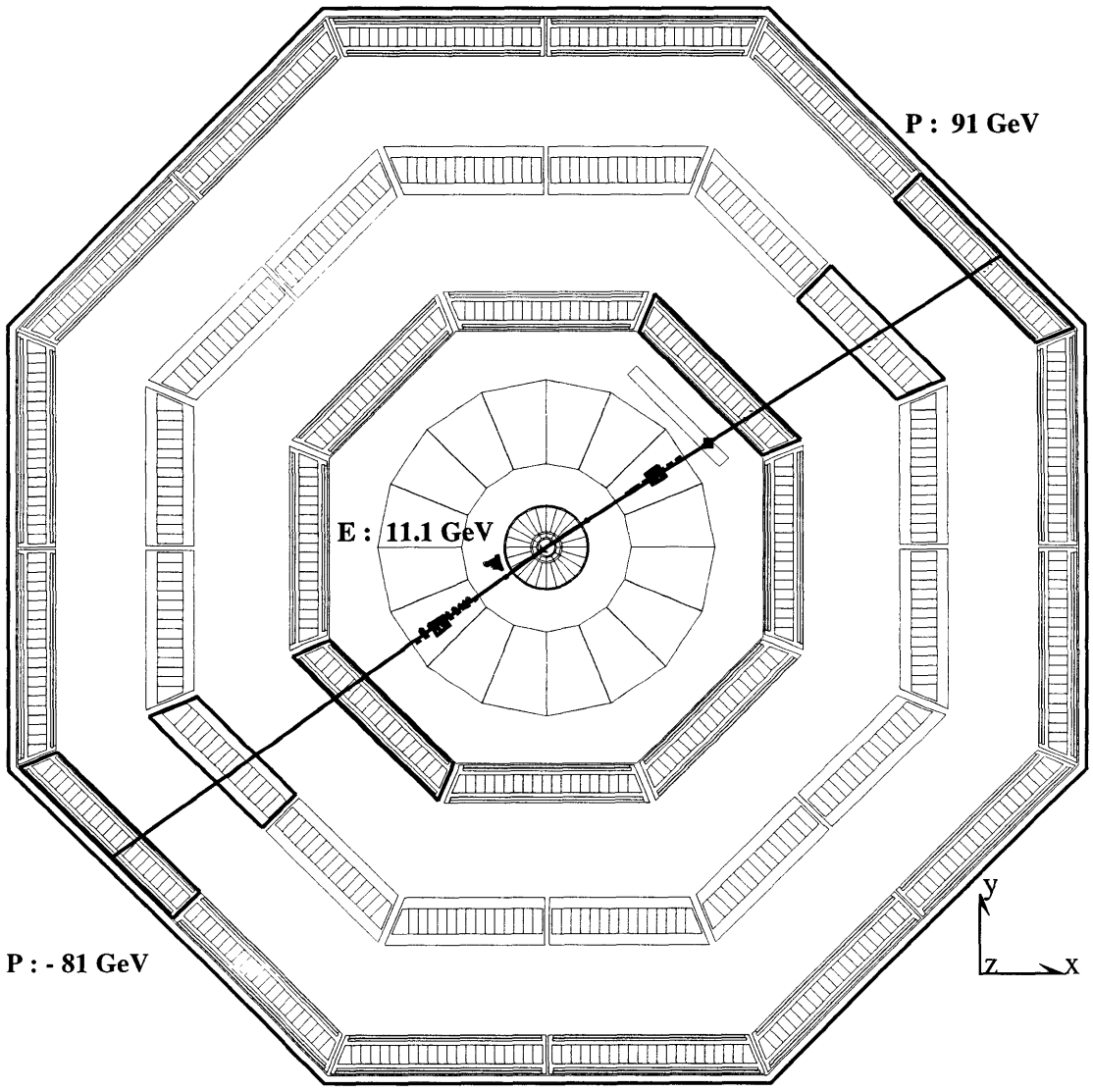

Figure 18: XY view of a typical $e^+e^- \to \mu^+\mu^-(n\gamma)$ event in the $\sqrt{s}$ =183GeV data set. Note the presence of two muons and a FSR photon in the detector.

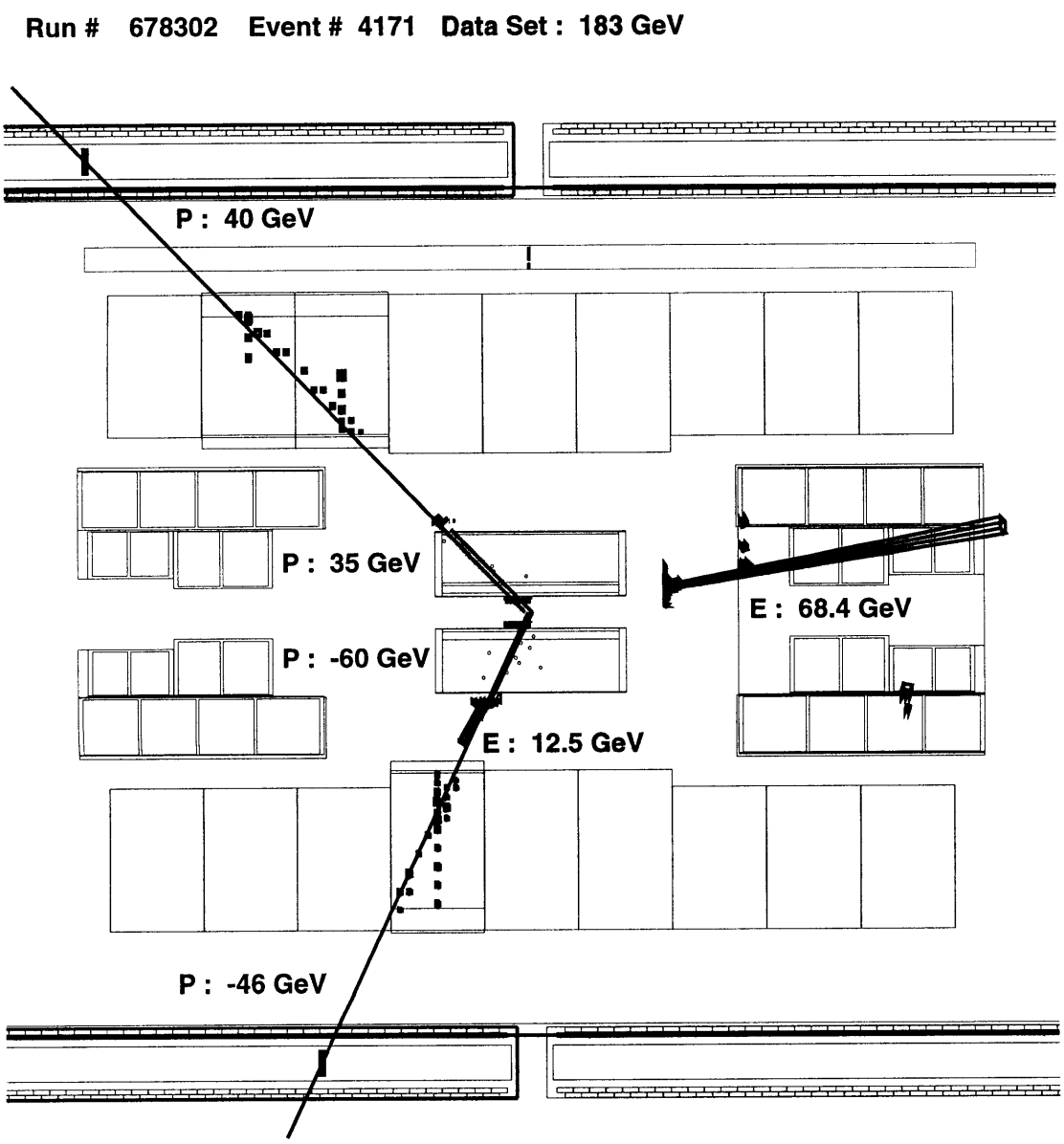

Figure 19: YZ view of a "return to Z" event in the $\sqrt{s}$ =183GeV data set. The ISR photon is seen in the detector. $\sqrt{s'}$ calculated from the muon polar angles alone is 96GeV, which is larger than the Z mass since the ISR is not collinear with the beam pipe. $\sqrt{s'}$ calculated from the measured muon momentum is 69GeV. A collimated FSR photon can also be seen close to one of the muons.

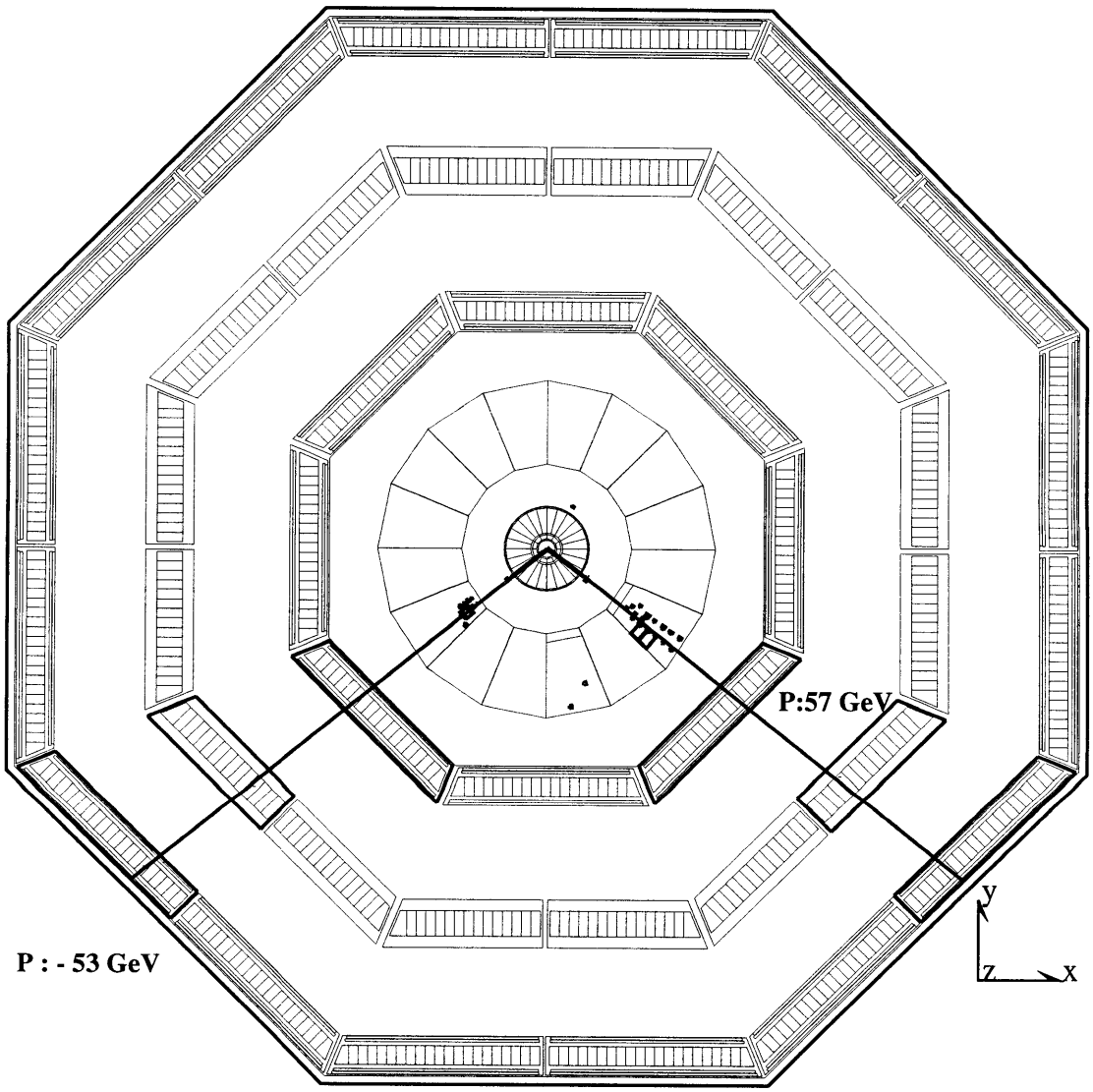

Figure 20: XY view of a $e^+e^- \rightarrow W^+W^- \rightarrow \mu^+\mu^-$ background event in the $\sqrt{s}$ =183GeV data set. Note the missing energy in the form of neutrinos. Although the measured invariant mass of the muon pair is 89GeV, the missing energy points to an active region of the detector, eliminating the return-to-Z hypothesis.

3.9.3 BGO Electromagnetic Calorimeter

Crystal energy is determined by using a nonlinear function which transforms ADC counts into energy. Adjacent crystals with energy are attached together; maxima, i.e. a crystal which has more energy than all of it contiguous neighbors are defined to be bumps. Bumps are classified by how well they fit to the test beam electron shower shape data. Discrimination between hadrons which undergo a nuclear interaction in a BGO crystal and electromagnetically interacting particles is quite good.

3.9.4 Inner Tracker and Vertex Reconstruction

Since the magnetic field in the center of L3 in the inner tracker is much more uniform than that in the location of the muon chambers, the simplification of fitting a helical trajectory to spatially close hit wires is used. The two layers of double sided silicon of the Silicon Microvertex Detector and up to 62 high resolution measurements in the $r - \phi$ projection of the time expansion chambers allow the inner tracker to be sensitive to the luminous region of beam collision (Figure 21).

3.10 Event Simulation

The event generators discussed in Section 2 are interfaced with the GEANT [89] detector simulation package. The package is used to model the L3 sub-detectors. The trigger, data acquisition, and event reconstruction are also modeled. A database [90] is extensively used. A number between ten to one hundred times the data set size of Monte Carlo generated events are run through the complete detector simulation so that efficiency predictions can be made.

Inner tracker pre-selection cuts		
Cut variable	Loose cut	Tight cut
χ^2/DoF of track circle fit	6.0	1.5
Track DCA	4.0mm	1.0mm
Track Z at DCA	120.0mm	30.0mm

Table 4: Inner tracker pre-selection track multiplicity cuts.

4 Analysis

4.1 Pre-selection of $e^+e^- \rightarrow \mu^+\mu^-(n\gamma)$ Events

From the archived events that made it past the level 3 trigger, data summary tapes are made. For future reference, the data summary tapes created by version 220 of the algorithm were used. Not all of the archived events remain on the data summary tapes. An attempt is made to eliminate the noise events missed by the level 3 trigger; nevertheless, there are still 7 million events that remain in the data summary tapes. A conservative "pre-selection" is made on these 7 million events to reduce the data set size. There are two loose pre-selection cuts. The first pre-selection cut eliminates events which only have very low momentum tracks. There must be two or more tracks anywhere in the muon chambers or inner tracker with greater than 10GeV momentum. The cut is made before matching between the inner tracker and muon chambers so that later, reconstruction matching errors can be corrected, i.e., no inefficiency is introduced. The second, and final, pre-selection cut is on the inner tracker track multiplicity. An event must have between two and six good tracks pointing to the vertex at the loose pre-selection cuts defined in Table 4. As an additional safety feature, for the high track multiplicity events with more than six good tracks pointing to the vertex at the loose pre-selection cuts, it is checked if the event still has more than six good tracks pointing to the vertex at the tight pre-selection cuts defined in Table 4. Only high track multiplicity events failing both the tight and loose cuts are rejected. Note that adding a cut on the number of energy clusters in the calorimeters has an extremely small effect in the pre-selection because the track multiplicity cut already eliminates events with a large number of energy clusters in the calorimeters.

The number of events passing the pre-selection is listed in Table 5. Even though the pre-selection cuts are very loose, out of the 7 million events on the summary tapes only 25254 remain, a factor 300 reduction.

$\sqrt{s}$(GeV)	$\int \mathcal{L}dt(pb^{-1})$	% error in $\int \mathcal{L}dt$	# events pre-selected	# events selected	% Data set Toroid Off
129.96	5.975	0.230	2534	99	55.0
135.96	5.693	0.245	2508	67	61.0
161.34	10.545	0.222	3260	87	0.0
172.13	9.808	0.244	3235	67	0.0
182.68	52.886	0.111	13717	324	95.5

Table 5: Overview of the data sets.

4.2 Selection of $e^+e^- \to \mu^+\mu^-(n\gamma)$ Events

The selection of $e^+e^- \to \mu^+\mu^-(n\gamma)$ events is made in three steps. First, all of the reconstructed objects in the sub-detectors are classified as being compatible or not being compatible with a muon (Section 4.2.1). Second, all inner tracker tracks compatible with being a muon are matched outward across the sub-detectors (Section 4.2.2). Third, events are classified as being $e^+e^- \to \mu^+\mu^-(n\gamma)$ event candidates or not (Section 4.2.3).

4.2.1 Sub-detector Object Quality Cuts

For a reconstructed sub-detector object to be considered a muon or photon candidate in that sub-detector, it must pass the cuts listed in Table 6. The distributions of selected events passing the cuts can be seen in Figures 21 and 22. Events which pass all selection cuts except for the one plotted are also included in the histograms (Figures 21 and 22) so that one may gauge the effect of the cut.

The inner tracker DCA resolution is approximately 100μm, so the 800μm DCA cut on the track with the smallest DCA is safe. The cut has been made as tight as possible in order to keep the cosmic ray contamination (Section 4.3.1), for which there is no Monte Carlo, to a minimum. Were it not for the cosmic ray contamination, one would clearly make the cut larger. The cut on the Z coordinate has also been made tight at 50mm from the zero in order to keep the cosmic ray rate low. For consistency, the cut on the muon chamber track is also at 50mm. The muon chamber DCA cut is set at 50mm because one must protect against large angle multiple scattering, an effect clearly seen in Figure 21. There are more entries in the inner tracker histograms because an inner tracker track is required for every muon whereas the muon chambers have the calorimeters as backup.

One expects a mean muon energy loss of 2.5GeV in the hadronic calorimeters, which is observed in Figure 22. Given the 50% energy resolution for muon tracks in the hadronic calorimeter, the 8GeV energy cut might seem too high. The cut is set high because there are detection gaps in the electromagnetic calorimeter, meaning an additional few GeV of collimated FSR energy can occasionally be added to the muon track cluster in the hadron calorimeter. The cut on the number of hits in a hadron calorimeter cluster is to increase the purity of minimum ionizing particle discrimination.

Sub-Detector Object Quality Cuts			
Inner Tracker			Fig.
$\|DCA\|$	$\leq$	800μm	21
Z	$\leq$	50mm	21
Muon Chamber			
$\|DCA\|$	$\leq$	50mm	21
Z	$\leq$	50mm	21
EM. Calorimeter			
EM 9 Xtal/ Sum 25 Xtal	$\geq$	0.98	22
Energy	$\leq$	1.5GeV	22
Hadronic Calorimeter			
Energy	$\leq$	8.0GeV	22
# hits	$\geq$	7	22

Table 6: The reconstructed sub-detector object quality cuts used to define muon candidates.

One expects a mean muon energy loss of 250MeV in the electromagnetic calorimeters, which is seen in Figure 22. The 1.5GeV cut on the electromagnetic calorimeter bump energy might seem too high given the 5% energy resolution in the BGO crystals at 250MeV. The cut is set high to account for the presence of collimated final state radiation. The cut on the ratio of the EM corrected fit energy in a matrix of 9 crystals to the raw energy in a matrix of 25 crystals is used to eliminate out of time cosmics which strike the electromagnetic calorimeter at an angle.

4.2.2 Matching Reconstructed Objects Across L3

Tracks are uniquely matched from the inner tracker outward. The method was chosen because it simplifies event classification (Section 4.2.3). Matching across sub-detectors is done by defining a four degree opening angle cone about inner tracker tracks. Any outer sub-detectors object inside the four degree opening angle cone is matched to the inner tracker track, resulting in a "linked muon candidate". The same four degree opening angle cone size is used for linking to all photonic bumps. A cone is not the ideal matching shape given the complicated detector geometry, yet the matching algorithm is absolutely stable. The stability is explained by the four degree cone size being much larger than the detector granularity. Further, the Gaussian multiple scattering angle, $\theta_{\rm MS}$, through the calorimeters is only one half a degree [3]. For the rare events with multiple matches in the muon chambers, the closest muon chamber track is matched to the inner tracker track. Matching in the calorimeters is inclusive to accommodate nearby final state radiation, i.e., several calorimeters bumps can be attached to a single muon candidate unless there is conflict, in which case the bumps

[3]The calorimeters comprise a thickness of 120 radiation lengths, x, before the muon chambers. One can use the Bethe formula [91], $\theta_{MS} = \frac{13.6\ \mathrm{MeV}}{p}\sqrt{x/X_o}[1 + 0.038\ln(x/X_o)]$ to find the Gaussian width of the scattering angle. A momentum of 20GeV yields one half a degree of multiple scattering. The lowest possible momentum of a "return to Z" muon is $m_Z^2/(2\sqrt{s})$, so 20GeV is the appropriate point to make the estimate.

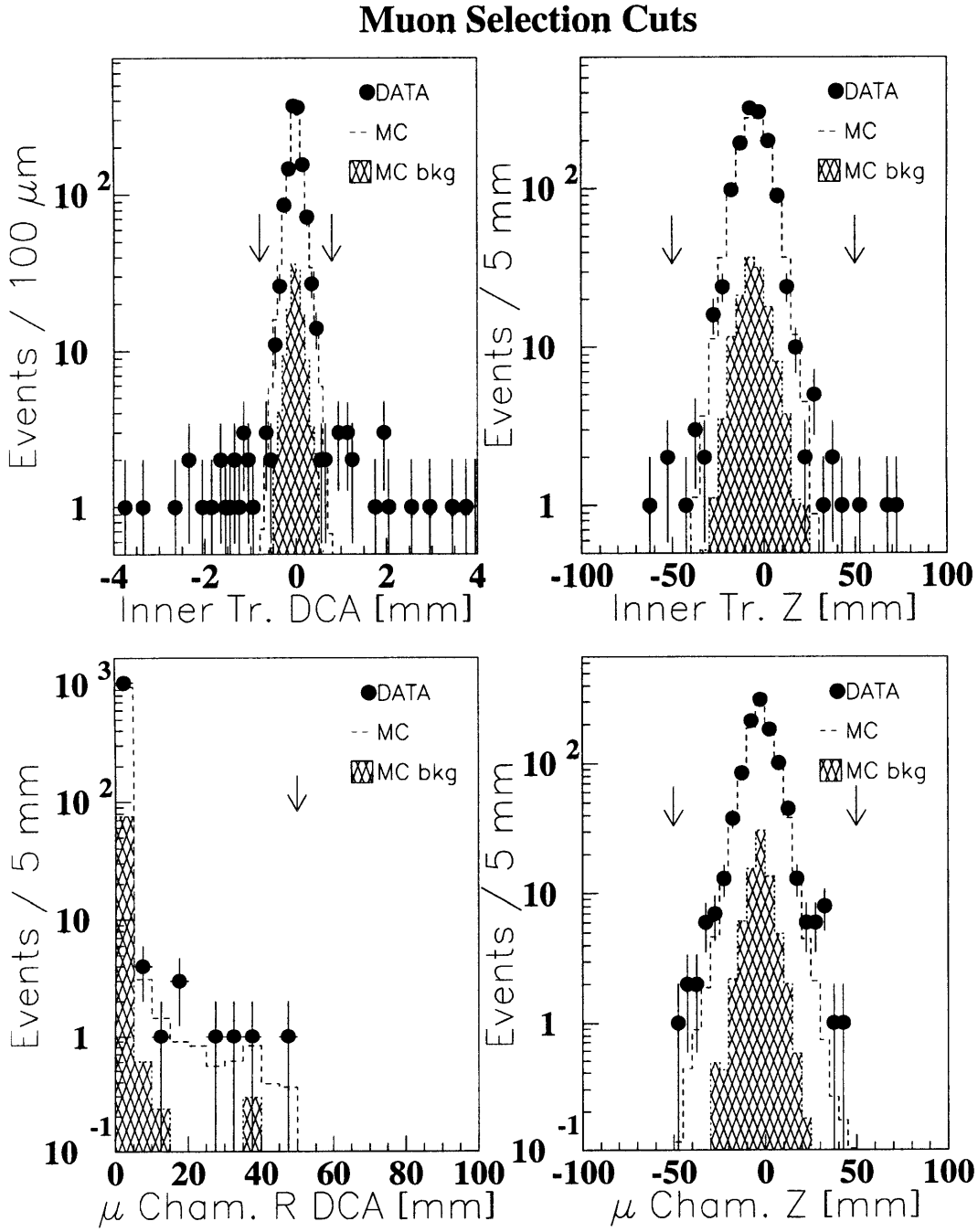

Figure 21: Selected events plus events passing all cuts except the cut plotted. Cut positions are indicated with an arrow (Table 6). Note the log scale. Every track must pass the the inner tracker vertex cuts to become a muon candidate, whereas tracks failing the vertex cut in the muon chambers could still be recovered by the backup cuts (Figure 22). Top left, inner tracker: distance of closest approach to the nominal vertex in the $r-\phi$ plane, DCA. Top right, inner tracker: Z coordinate. Bottom left, muon chambers: distance of closest approach to the nominal vertex in the $r-\phi$ plane, DCA. Bottom right, muon chambers: Z coordinate.

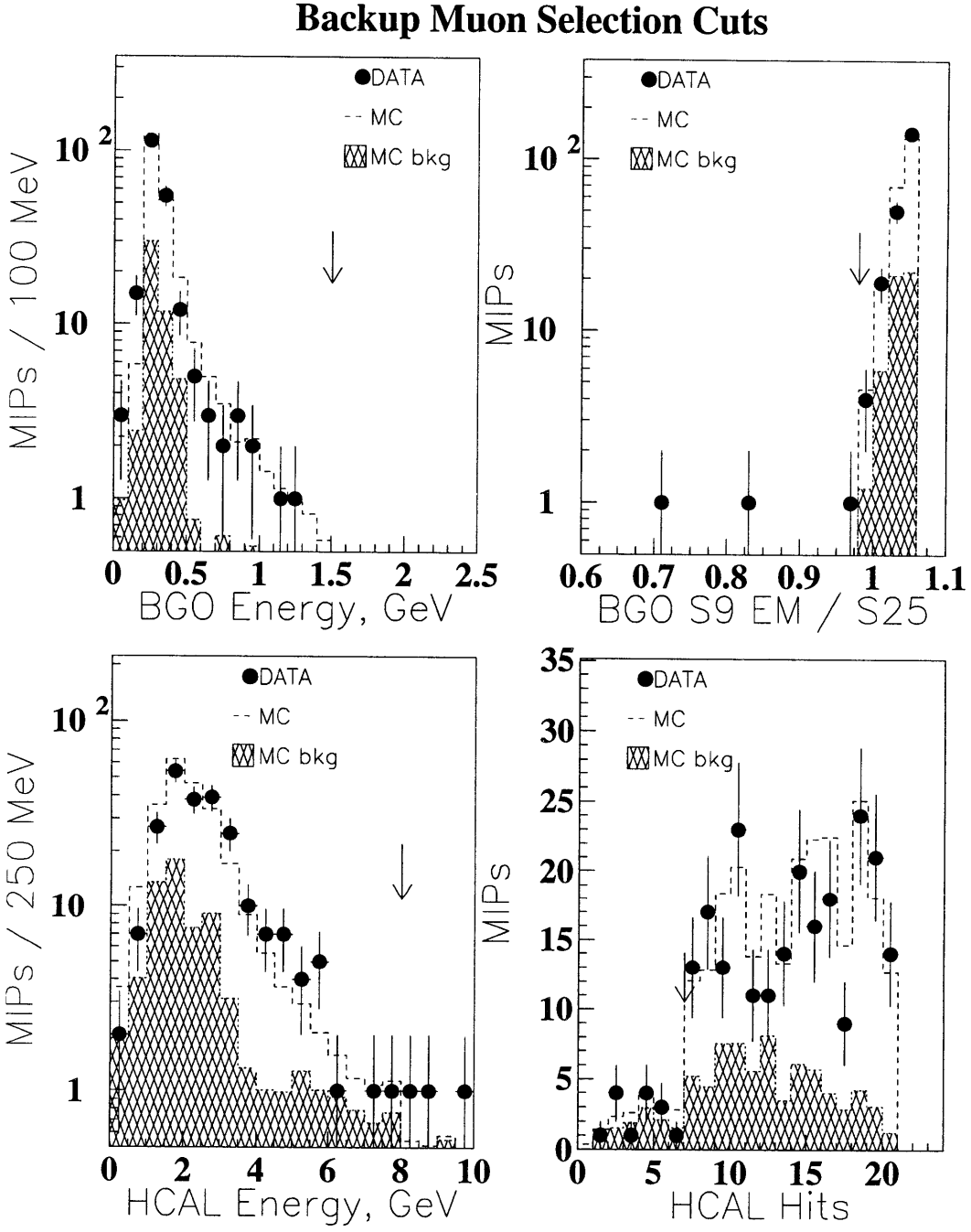

Figure 22: Selected events plus events passing all cuts except the cut plotted. Cut positions indicated with an arrow (Table 6). Upper left: energy deposited in the electromagnetic calorimeter. Upper right: ratio of fit electromagnetic shower energy in 9 adjacent crystals to raw energy in 25 adjacent crystals. Lower left: energy deposit of muon candidates in the hadron calorimeter. Lower right: hit cells attached to muon track candidates in the hadron calorimeter. The spread in the distribution is caused by muons which cross over modules in the Z coordinate and in phi.

are uniquely matched to the closest track.

If there are no matches inside the cone at a given sub-detector layer, it is checked if there would have been a unique match in the phi projection, because the phi projection is measured more often, and therefore more reliable than the polar angle. Sub-detector objects are recovered in 4 % of the selected events which had missing or poor z coordinate information. The small pre-section bias introduced by recalculating the momentum in 4 % of the events is negligible with respect to the efficiency loss if these events would be thrown away.

4.2.3 Two Muon Events

There are three types of matched sub-detector objects passing the quality cuts described in the previous two sections which are called muons:

1. An inner tracker track has at least one uniquely matched muon chamber track. The highest momentum muon chamber track matched to the inner tracker track has a momentum greater than the pre-selection momentum cut, 10GeV. The calorimeter information is ignored.

2. An inner tracker track with 10GeV or more momentum has at least one uniquely matched, minimum ionizing compatible electromagnetic calorimeter bump *and* has at least one uniquely matched, minimum ionizing compatible hadronic calorimeter energy deposit.

3. An inner tracker track with 10GeV or more momentum has at least one uniquely matched, minimum ionizing compatible electromagnetic calorimeter bump *or* has at least one uniquely matched, minimum ionizing compatible hadronic calorimeter energy deposit.

These are called "muon chamber" muons, "double calorimeter" muons, and "single calorimeter" muons, in descending order of priority. Figure 23 is a breakdown of the two muon candidates event types in the 183GeV data set. Notice how the majority of the events are identified with at least one muon in the muon chambers. It was cross-checked that the measurement can be made with the backup double and single calorimeter muons alone, albeit with 35% larger statistical error. Foreshadowing the rest of the chapter, cuts are also made on the muon pair opening angle which must be more that 90°, the scintillator time differences, and the highest muon momentum; all increase the signal purity.

4.3 Backgrounds

The breakdown of the backgrounds in the selected events are found in Table 7. The largest physics background is the two photon background at high energy in the $\sqrt{s'} > 10\%\sqrt{s}$ sample, which is simply explained by the boost of the Z in the "return-to-Z" events increasing at high energy. The "return-to-Z" events become less and less distinguishable from two photon events based on the muon

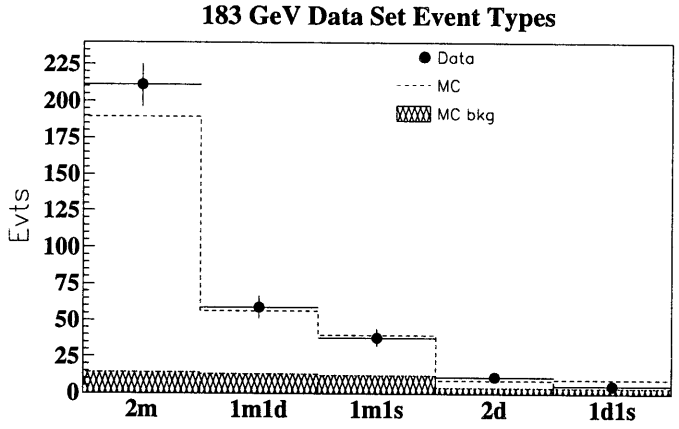

Figure 23: Event types in the 183GeV data set. From left to right in order of decreasing priority: two muon chamber muons (2m), one muon chamber muon + one double calorimeter muon (1m1d), one muon chamber muon + one single calorimeter muon (1m1s), two double calorimeter muons (2d), one double calorimeter + one single calorimeter muon (1d1s).

polar angles alone at high energy. Note how the W-pair background increases after threshold. The Tau-pair background slowly increases with increasing $\sqrt{s}$ because of the fixed momentum cut used in the analysis.

The bias in the $\sqrt{s'}$ estimate, sometimes called "feed-through" or "ISR contamination", is caused by $e^+e^- \to \mu^+\mu^-(n\gamma)$ events with small muon pair invariant mass which are assigned to the high $\sqrt{s'}$ sample. It is treated as a "background" to the signal, but in fact, one is just unfolding the spectrum. Since the separation between high energy and the "return-to-Z" events improves at higher $\sqrt{s}$, the correction decreases with increasing $\sqrt{s}$.

4.3.1 Cosmic Ray Background

On the Z pole, the cosmic ray background contamination [92, 93] was determined to be $\approx 0.15\%$ of the candidate events. At 183GeV, the cross section for back to back muons is reduced by a factor 500. Clearly, a new strategy had to be developed, or a precise measurement of the $e^+e^- \to \mu^+\mu^-(n\gamma)$ cross section could not be made. Three things were changed in the present analysis to keep the cosmic ray contamination down to the percent level: the momentum cuts, the vertex cuts, and the timing cuts. The price to pay for tighter cuts is a slight increase in the systematic error which is by far outweighed by the factor 100 decrease in the cosmic ray contamination.

Since the cosmic ray momentum spectra falls like $1/p^3_{cosmic}$ [21], the 10GeV pre-selection momentum cut is required on both muon candidates in an event. One muon must be measured to have at least 40GeV momentum. Past analysis [94, 92, 93, 95] only cut on one muon's momentum. As was already mentioned, the inner tracker has $\approx 100\mu$m resolution in the $R-\phi$ plane, so a tight cut

Relative Background Contamination in Event Candidates, in %									
$\sqrt{s}$	$\tau^+\tau^-$	W^+W^-	$e^+e^-\mu^+\mu^-$	q^+q^-	ZZ	Ze^+e^-	$\mu^+\mu^-_{\text{bias}}$	Cosmic	Total
Cut: $\sqrt{s'} > 0.1\sqrt{s}$									
130	1.26	.00	2.29	.00	.00	.01	.25	.40	4.21
136	1.20	.00	1.98	.00	.00	.00	.43	.40	4.00
161	1.79	.06	5.86	.00	.00	.00	.44	.40	8.55
172	1.92	.31	7.90	.00	.00	.00	.43	.40	10.96
183	1.94	.48	9.57	.00	.00	.01	.28	.40	12.68
Forward Events									
130	1.30	.00	1.28	.00	.00	.00	.16	.20	2.94
136	.86	.00	1.47	.00	.00	.00	.27	.20	2.80
161	1.80	.05	3.98	.00	.00	.00	.31	.20	6.34
172	2.04	.34	4.74	.00	.00	.00	.31	.20	7.63
183	1.96	.61	5.79	.00	.00	.02	.17	.20	8.75
Backward Events									
130	.93	.00	3.15	.00	.00	.00	.49	.20	4.76
136	1.32	.00	2.07	.00	.00	.00	.61	.20	4.20
161	1.48	.06	6.22	.00	.00	.01	.53	.20	8.49
172	1.29	.21	9.61	.00	.00	.01	.56	.20	11.88
183	1.63	.24	10.89	.00	.00	.01	.40	.20	13.37
Cut: $\sqrt{s'} > 0.85\sqrt{s}$									
130	1.48	.00	.47	.00	.00	.01	11.26	.30	13.51
136	1.55	.00	1.21	.00	.00	.00	9.72	.30	12.78
161	2.13	.03	2.41	.00	.00	.00	7.07	.30	11.95
172	2.26	.21	2.68	.00	.00	.00	6.62	.30	12.07
183	2.46	.34	4.42	.00	.00	.00	5.11	.30	12.63
Forward Events									
130	1.49	.00	.33	.00	.00	.00	8.57	.20	10.59
136	1.12	.00	.59	.00	.00	.00	6.68	.20	8.59
161	2.09	.03	1.45	.00	.00	.00	5.51	.20	9.27
172	2.30	.20	.59	.00	.00	.00	5.59	.20	8.88
183	2.41	.40	2.51	.00	.00	.00	4.50	.20	10.02
Backward Events									
130	1.20	.00	1.02	.00	.00	.00	19.22	.20	21.64
136	1.65	.00	.00	.00	.00	.00	19.29	.20	21.14
161	1.98	.06	3.62	.00	.00	.02	12.69	.20	18.56
172	1.52	.17	6.43	.00	.00	.00	10.53	.20	18.86
183	2.25	.15	5.98	.00	.00	.02	7.43	.20	16.03

Table 7: The percentage of background contamination at the different $\sqrt{s}$ obtained from SM MC and detector simulation.

of 800μm on at least one of the muons is used; furthermore, all muons satisfy the pre-selection inner tracker DCA constraint.

A final cosmic ray rejection cut is on the barrel scintillator times. For every muon candidate, the smallest of the three scintillator times closest in the phi projection is attached to it. If both muons are in the barrel and one is above 11.25° from the horizontal plane and one is below 11.25° from the horizontal plane and both have a time of flight corrected time greater than 3.0ns from zero the event is rejected as a cosmic ray. If the acollinearity of the two muons is less than ten degrees and the difference of their time of flight corrected times is between -10ns and -4ns (cosmic rays could have between -9ns and -5ns time of flights), the event is rejected as an unambiguous cosmic ray. Events having only one scintillator time are accepted if the time of flight corrected time is less than 3.0ns from zero.

The flatness of the muon chamber track angular distributions after the selection cuts demonstrates the effectiveness of the cosmic ray rejection (Figure 24). The residual cosmic ray contamination was determined by using the events which pass all of the cuts except the inner tracker vertex cuts. The estimate was cross-checked by a visual scan of the selected events and by counting the number of selected events between the negative ten to four nano-second band.

4.4 Selected Event Distributions

The θ, ϕ, highest momentum muon (P_{μ}^{high}), muon pair opening angle, $\sqrt{s'}$, and muon pair invariant mass distributions are found in Figure 25. In the θ and ϕ distributions there are two entries per event. In the other four distributions, there is one entry per event. The sum of the MC background and the MC signal plus background distributions are plotted for comparison with the data distributions. The small cosmic ray background estimate is not included in the MC sum.

The agreement with Monte Carlo is acceptable given the statistics of the data set. A detailed investigation of the structure in the $\cos\theta$ and momentum distributions, which catch the eye, revealed no peculiarities. The cross section one would have measured had one chosen a different value of the momentum cut or a different polar angle cut off in the detector is plotted (Figure 26) as a ratio with the measured cross section at the nominal cut. At each cut value, the potential one sigma statistical error due to the change in the number of events, $\propto \sqrt{|N_{\rm cut} - N_0|}$, is plotted. To be conservative, the variation caused by the θ and momentum cut is accounted for by assigning one half the largest (statistically significant) deviation, or $\approx 5\%$, as a systematic error in Section 5. Variations in all of the other cut variables were checked to have a negligible effect on the measured quantities, except for the vertex cuts, which are treated separately (Section 4.3.1), since there is no cosmic ray Monte Carlo.

The efficiency of using the $\sqrt{s'}$ estimator instead of the muon pair invariant mass for measuring the cross section can also be seen in Figure 25. Even though the background contamination in the

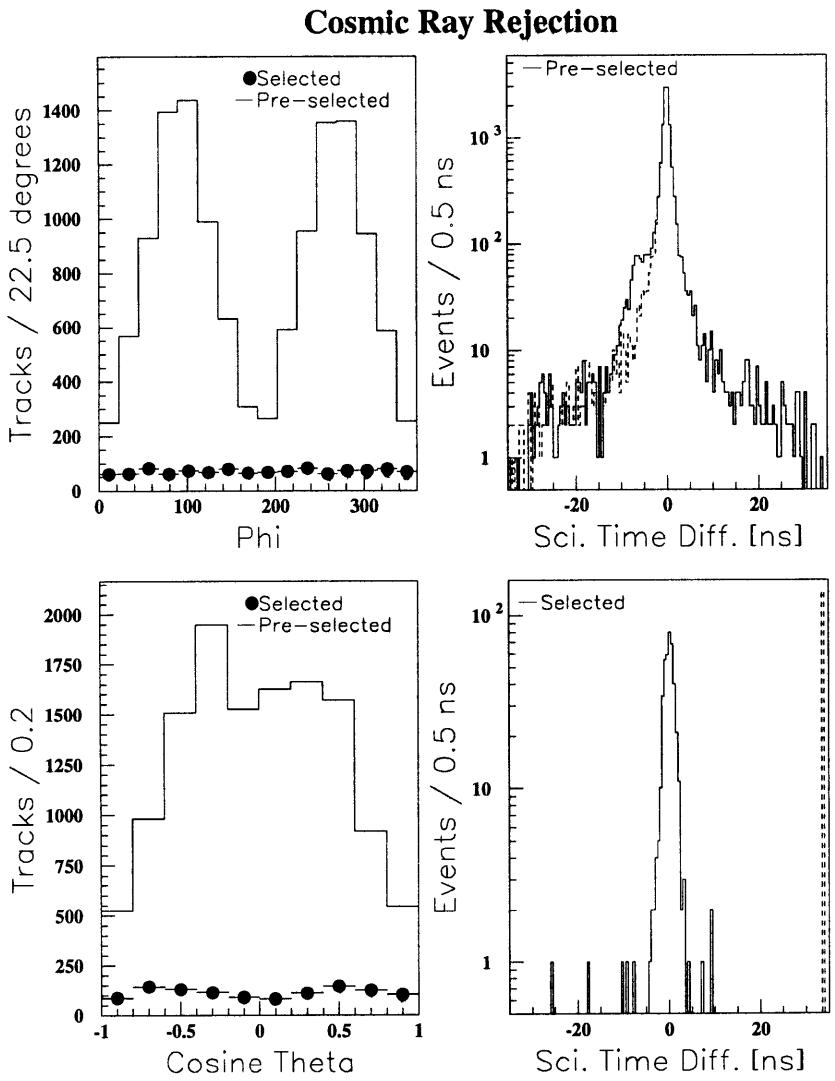

Figure 24: All data. Upper left: Note the preponderance of cosmic rays in the pre-selected event ϕ distribution. The peaks at 90° and 270° in ϕ correspond to vertical in the L3 coordinate system. Lower left: The peak at $\cos\theta = -0.4$ is the default for muons without Z coordinate information and the concentration in θ between 45° and 135° is caused by a 23m diameter access shaft drilled during the experiment's construction. Upper right: For the pre-selected events, the barrel scintillator time difference between upper and lower counters; the reflection of the histogram about zero accentuates "in time" cosmic peak; the majority of the events are out of time cosmic rays in coincidence with Uranium noise. The level 1 scintillator gate is ±30ns and the level 3 scintillator gate is ±10ns. Lower right: For the selected events, the barrel scintillator time difference between upper and lower counters, when both exist. Also shown in the overflow bin is the number of events passing all cuts *except* the scintillator timing cut.

high muon invariant mass sample is small, the product of the purity and efficiency is 25% less than in the $\sqrt{s'}$ distribution at an equivalent cut because of the momentum resolution.

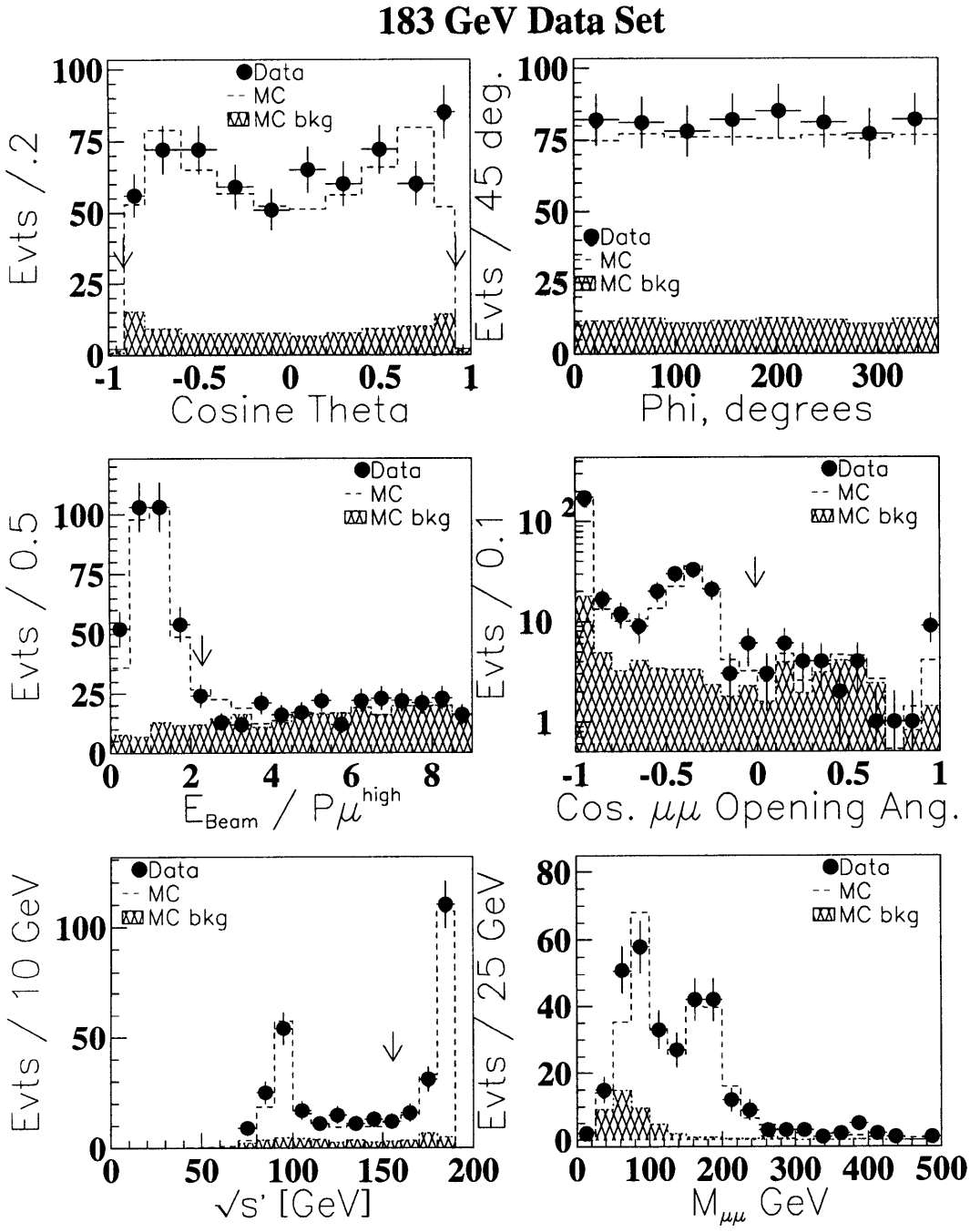

Figure 25: All selected muon candidates. Cuts indicated with an arrow. Upper left: $\cos\theta$, last bin ends at cos(24°). Upper right: ϕ. Center left: Highest momentum muon. Center right: $\cos\theta^{\mu\mu}_{opening}$. Bottom left: $\sqrt{s'}$. Bottom right: Measured $\mu\mu$ invariant mass.

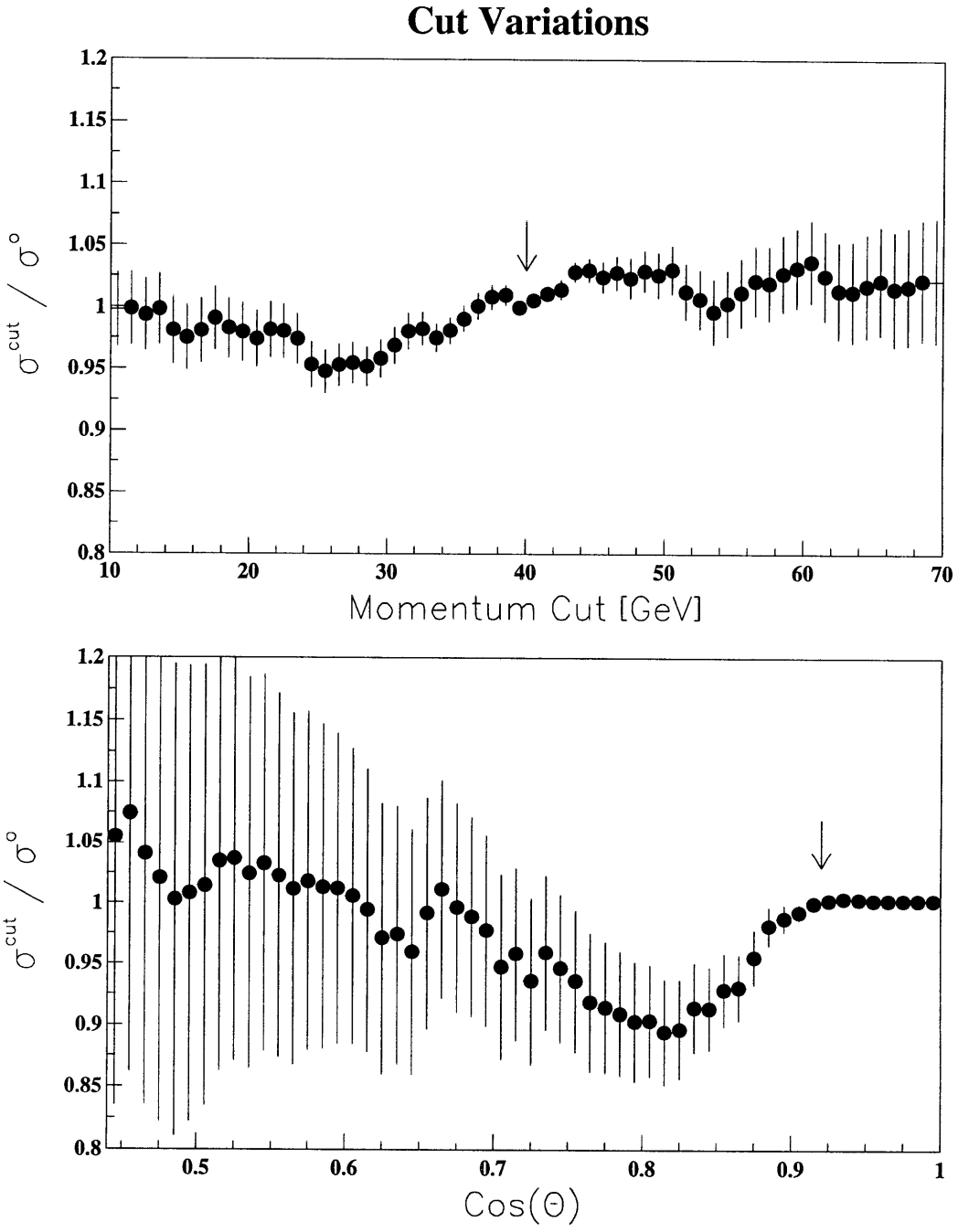

Figure 26: Variation of the measured cross section in the 183GeV data set with respect to changes in the momentum cut and the fiducial volume cut.

5 Results

5.1 Cross Section

The formula for the measured cross section is

$$\sigma = \frac{N_{cand} - N_{bkg}}{\int \mathcal{L}dt \cdot \prod_i \epsilon_i}. \tag{15}$$

N_{cand} is the number of candidate events selected by the analysis (Section 4). N_{bkg} is the number of background events estimated to be contained in the candidate events,

$$N_{bkg} = N_{\tau\tau} + N_{WW} + N_{ee\mu\mu} + N_{qq} + N_{ZZ} + N_{Zee} + N_{bias} + N_{Cosmic}. \tag{16}$$

All are obtained using Standard Model Monte Carlos, except for the cosmic ray contamination, N_{Cosmic}. Table 7 lists the background contaminations at the different energies and $\sqrt{s'}$ cuts. $\int \mathcal{L}dt$ is the integrated luminosity of the data sample (Table 5), and the product $\prod_i \epsilon_i$ is a product of the efficiency due to acceptance times the efficiency caused by the trigger; they are uncorrelated (Appendix B).

One should never rely blindly on Monte Carlo. As a simple cross check of the efficiency for the $\sqrt{s'} > 0.85\sqrt{s}$ cross section measurement, one can use Equation 6 and integrate in polar angle up to 24 degrees, the edge of the endcap muon chambers. The phi detection gaps can be ignored because of the two backup calorimeter muon selections. The resulting $\approx$ 90% efficiency due to detector acceptance alone can be compared with the $\sqrt{s'} > 0.85\sqrt{s}$ efficiencies in Table 8; keeping track of the details with the Monte Carlo detector simulation makes a difference in the final results at the few percent level.

The errors on the MC efficiency calculations are determined by assuming a binomial distribution of selected and skipped Monte Carlo events and that the calculated efficiency is an unbiased estimator of the real efficiency,

$$\begin{aligned} \epsilon &= N^{MC}_{selected}/N^{MC}_{total} \\ \sigma_\epsilon &= \frac{\sqrt{\epsilon(1-\epsilon)}}{N^{MC}_{total}}. \end{aligned} \tag{17}$$

See Table 8 for the final result, or graphically, in Figure 27.

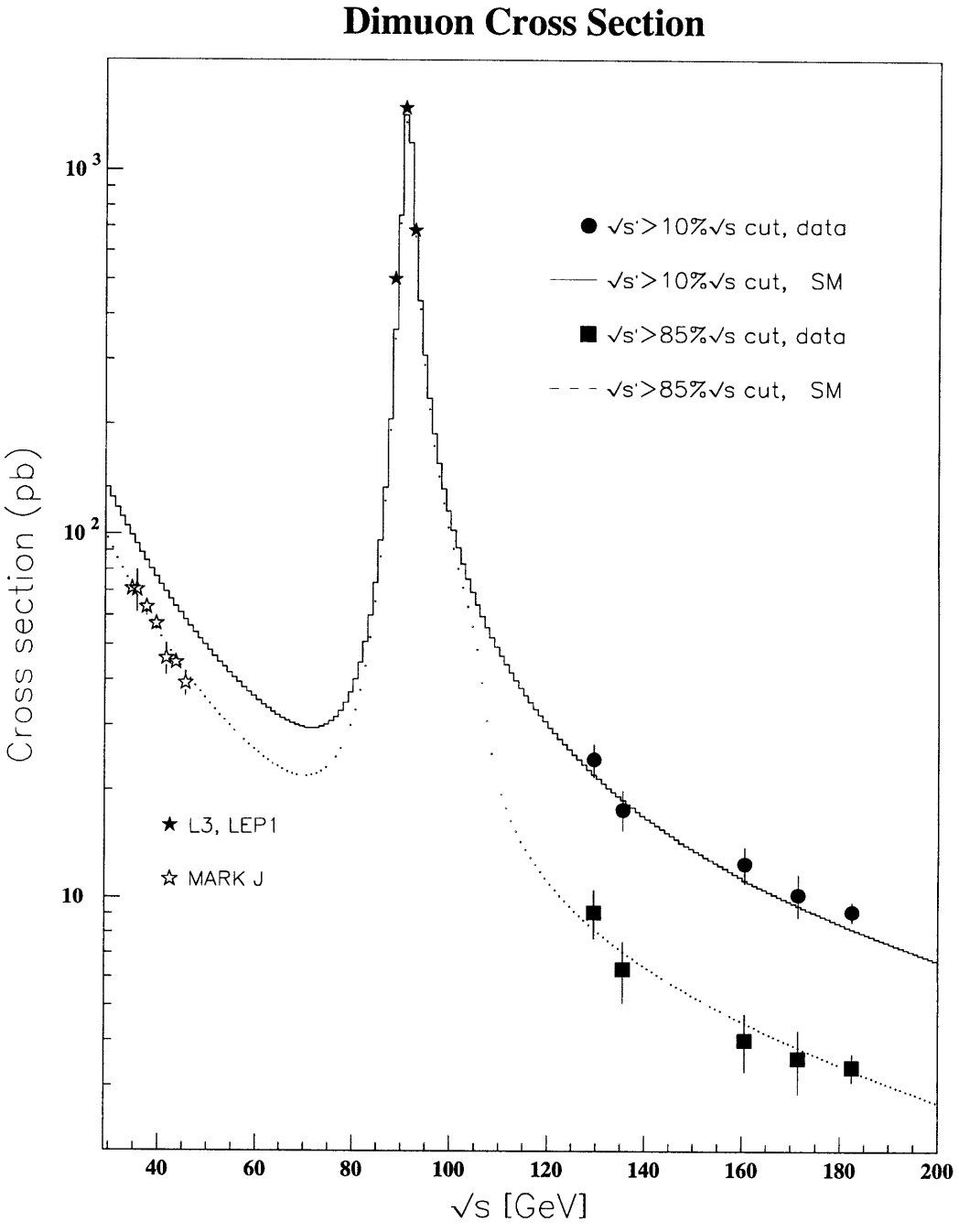

Figure 27: The measured cross section at $\sqrt{s'} > 10\%$ and $85\%\sqrt{s}$ cuts (solid circles and squares). Error bars statistical only. SM prediction, ZFITTER 5.00, is shown. Selected previous lower energy measurements are also plotted [10, 96]

Cross Section Results							
Events: $\sqrt{s'} > 0.1\sqrt{s}$							
$\sqrt{s}$ [GeV]	N_{cand}	$\%Bkg.$	ϵ_{acc}	σ [pb]	Δ^{σ}_{stat} [pb]	Δ^{σ}_{syst} [pb]	$\sigma_{SM}[pb]$
130	99	4.21	.657	24.26	2.54	1.21	22.05
136	67	4.00	.638	17.66	2.25	.88	18.74
161	87	8.55	.611	12.46	1.45	.62	11.21
172	67	10.96	.601	10.21	1.39	.51	9.49
183	324	12.68	.593	9.14	.57	.46	8.19
Events: $\sqrt{s'} > 0.85\sqrt{s}$							
$\sqrt{s}$ [GeV]	N_{cand}	$\%Bkg.$	ϵ_{acc}	σ [pb]	Δ^{σ}_{stat} [pb]	Δ^{σ}_{syst} [pb]	$\sigma_{SM}[pb]$
130	54	13.51	.871	9.10	1.41	.46	8.19
136	35	12.78	.836	6.32	1.24	.32	7.06
161	40	11.95	.821	4.01	.73	.20	4.48
172	33	12.07	.822	3.57	.71	.18	3.82
183	164	12.63	.804	3.38	.30	.17	3.31

Table 8: The measured cross section.

5.2 Forward-Backward Asymmetry

The forward-backward asymmetry, A_{fb}, can be measured in the same way as the cross section. Use equation 4 and replace the cross sections by the background subtracted and efficiency corrected number of events:

$$A_{fb} = \frac{\frac{N_f^{cand} - N_f^{bkg}}{\int \mathcal{L}dt \cdot \prod_i \epsilon_f} - \frac{N_b^{cand} - N_b^{bkg}}{\int \mathcal{L}dt \cdot \prod_i \epsilon_b}}{\frac{N_f^{cand} - N_f^{bkg}}{\int \mathcal{L}dt \cdot \prod_i \epsilon_f} + \frac{N_b^{cand} - N_b^{bkg}}{\int \mathcal{L}dt \cdot \prod_i \epsilon_b}} \tag{18}$$

The acceptance, charge confusion probability, and the effect of background with asymmetries different than the signal are automatically taken care off. See Table 9 for the final result, or graphically, in Figure 28. Notice how $\sigma_f + \sigma_b$ in Table 9 corresponds to σ in Table 8 to well within the statistical error, Δ^{σ}_{stat}, of σ.

5.3 Z' Mass and Coupling Limits

One can use the measured cross section and forward-backward asymmetry (Figures 27 and 28) at the high $\sqrt{s'}$ cut to put limits on the mass an additional Z' boson might have. The return-to-Z events are cut away with the high $\sqrt{s'}$ cut to increase the sensitivity to Z' propagator effects [97]. As an illustration, if one chooses $g^{Z'} = \frac{e}{\sin\theta_W}$, $a'_l = -0.59$, and $v'_l = -0.04$, their Standard Model Z boson values, a 95% confidence limit on the Z' mass $M_{Z'} > 315$GeVis obtained using this measurement alone. The L3 limit using all channels is 805GeV [98] which is 115GeV higher than the current CDF Standard Model Z' limit [36] of $M_{Z'} > 690$GeV.

There is a simple scaling law [99] which indicates the Z' mass limit will improve with increasing center of mass energy and luminosity as $(sL)^{\frac{1}{4}}$. If the LEP energy is raised to 200GeV and the

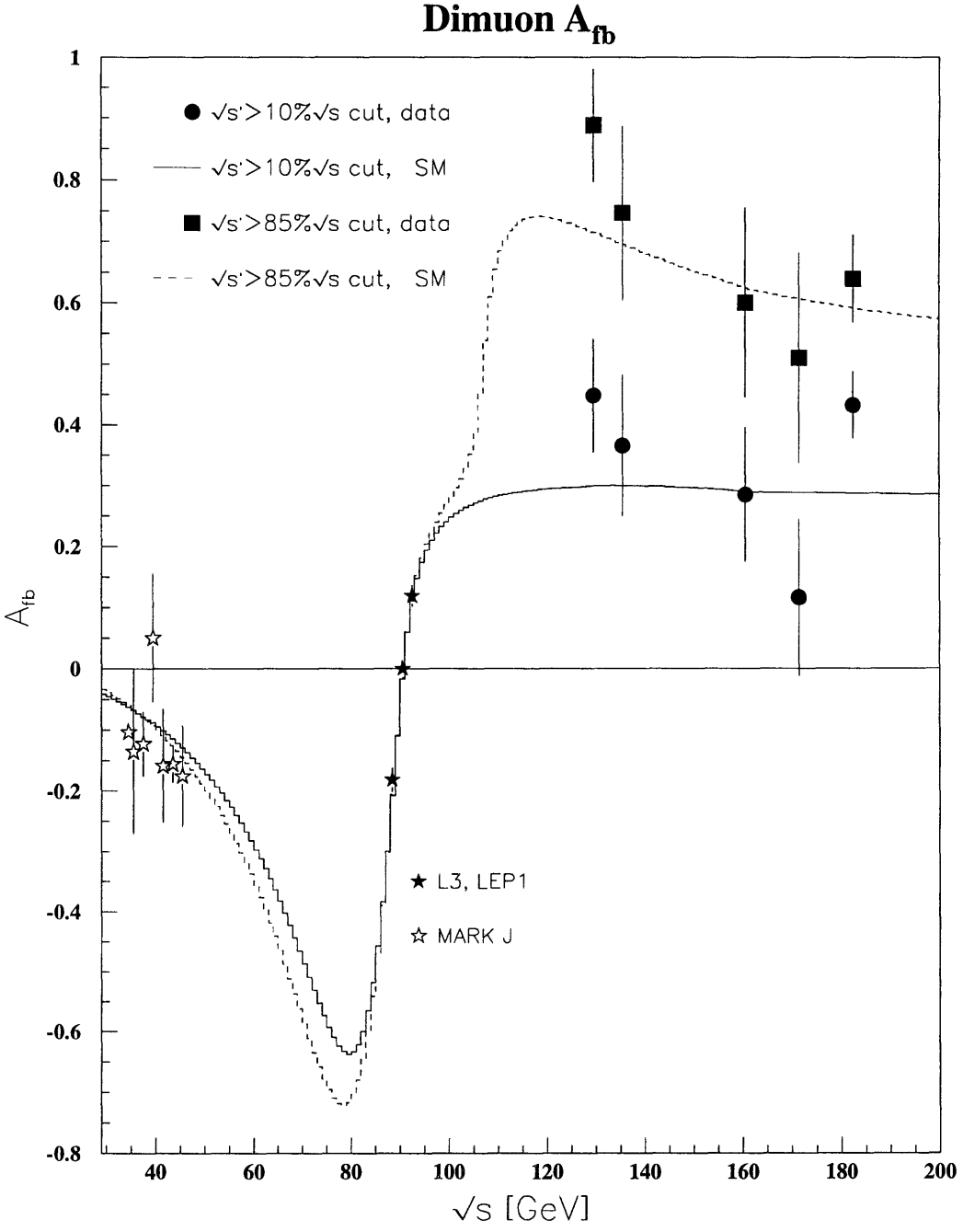

Figure 28: The measured A_{fb} at $\sqrt{s'} > 10\%$ and $85\%\sqrt{s}$ cuts (solid circles and squares). Error bars statistical only. SM prediction, ZFITTER 5.00, is shown. Selected previous lower energy measurements are also plotted [10, 96]

A_{fb} Results												
Events: $\sqrt{s'} > 0.1\sqrt{s}$												
$\sqrt{s}$	N_f	N_b	$\%bkg_f$	$\%bkg_b$	ϵ_f	ϵ_b	σ_f [pb]	σ_b [pb]	A_{fb}	$\Delta^{A_{fb}}_{stat}$	$\Delta^{A_{fb}}_{syst}$	A^{SM}_{fb}
130	67	25	2.9	4.8	.62	.59	17.63	6.73	.448	.093	.022	.299
136	44	20	2.8	4.2	.60	.58	12.52	5.82	.365	.116	.018	.300
161	49	26	6.3	8.5	.57	.53	7.73	4.30	.285	.110	.014	.289
172	34	25	7.6	11.9	.55	.51	5.77	4.57	.116	.129	.006	.289
183	194	79	8.8	13.4	.53	.50	6.40	2.54	.432	.055	.022	.288
Events: $\sqrt{s'} > 0.85\sqrt{s}$												
$\sqrt{s}$	N_f	N_b	$\%bkg_f$	$\%bkg_b$	ϵ_f	ϵ_b	σ_f [pb]	σ_b [pb]	A_{fb}	$\Delta^{A_{fb}}_{stat}$	$\Delta^{A_{fb}}_{syst}$	A^{SM}_{fb}
130	44	6	10.6	21.6	.75	1.12	8.98	.53	.888	.092	.044	.714
136	26	7	8.6	21.1	.71	1.08	5.84	.85	.746	.142	.037	.695
161	24	9	9.3	18.6	.70	.93	2.90	.72	.600	.155	.030	.623
172	20	9	8.9	18.9	.70	.88	2.63	.86	.509	.172	.025	.606
183	109	34	10.0	16.0	.67	.86	2.78	.61	.639	.071	.032	.591

Table 9: The measured Asymmetry.

integrated luminosity is increased by a factor ten to $500pb^{-1}$, one could expect at least a factor 2 improvement in the $m_{Z'}$ limit by the year 2000 [4].

5.4 Excited Lepton Search

A search for excited muon pair production,$\mu^*\mu^*$, and single excited muon production,$\mu^*\mu$, with subsequent photon de-excitation (Section 2.4.2) was made using the 183GeV data set. Published search results exist for the lower energy data at LEP [40, 41, 42, 43, 44, 45, 46, 47]. Taking the set of pre-selected events, the exact same procedure is followed as in Section 4 to select events with two muons: the same DCA cuts, the same energy cuts in the calorimeters, the same matching algorithm, etc. However, the 90° acollinearity cut (Figure 25) is removed and the momentum cut is fixed to its pre-selection value, 10GeV; relaxing these two cuts increases the search efficiency. Only photons with greater than 20GeV energy are used to make the muon-photon invariant mass spectrum, in order to reduce the FSR background to the search.

The result of the search for pair-production of excited muons in the 183GeV data is shown in Figure 30. No data events pass the cuts. The Monte Carlo expectation is that 0.8 multiple hard radiative events would pass the selection cuts and mimic excited muon pair production. Only one data event has two photons with energy greater than 20GeV, but the event is not a candidate because one of the two muons does not pass the momentum cut. The event with two photons and two muons

[4] Off the Z peak and ignoring the coupling strength, the size of the ratio of the $Z'\gamma$ interference to the photon propagator is $s/(M^2_{Z'} - s)$. Let O be an observable quantity. To detect a Z' from a deviation of O, one needs: $\Delta O_{Z'}/O > s/(M^2_{Z'} - s)$, but $\Delta O_{stat}/O = 1/\sqrt{N}$, and $N = \sigma \times L$. With $\sigma \sim 1/s$, one has $\Delta O_{stat}/O \sim \sqrt{s/L}$. Assuming a heavy $M_{Z'}$, $M_{Z'limit} \sim \sqrt{O/\Delta O_{stat}}\sqrt{s}$, or $M_{Z'limit} \sim (sL)^{\frac{1}{4}}$.

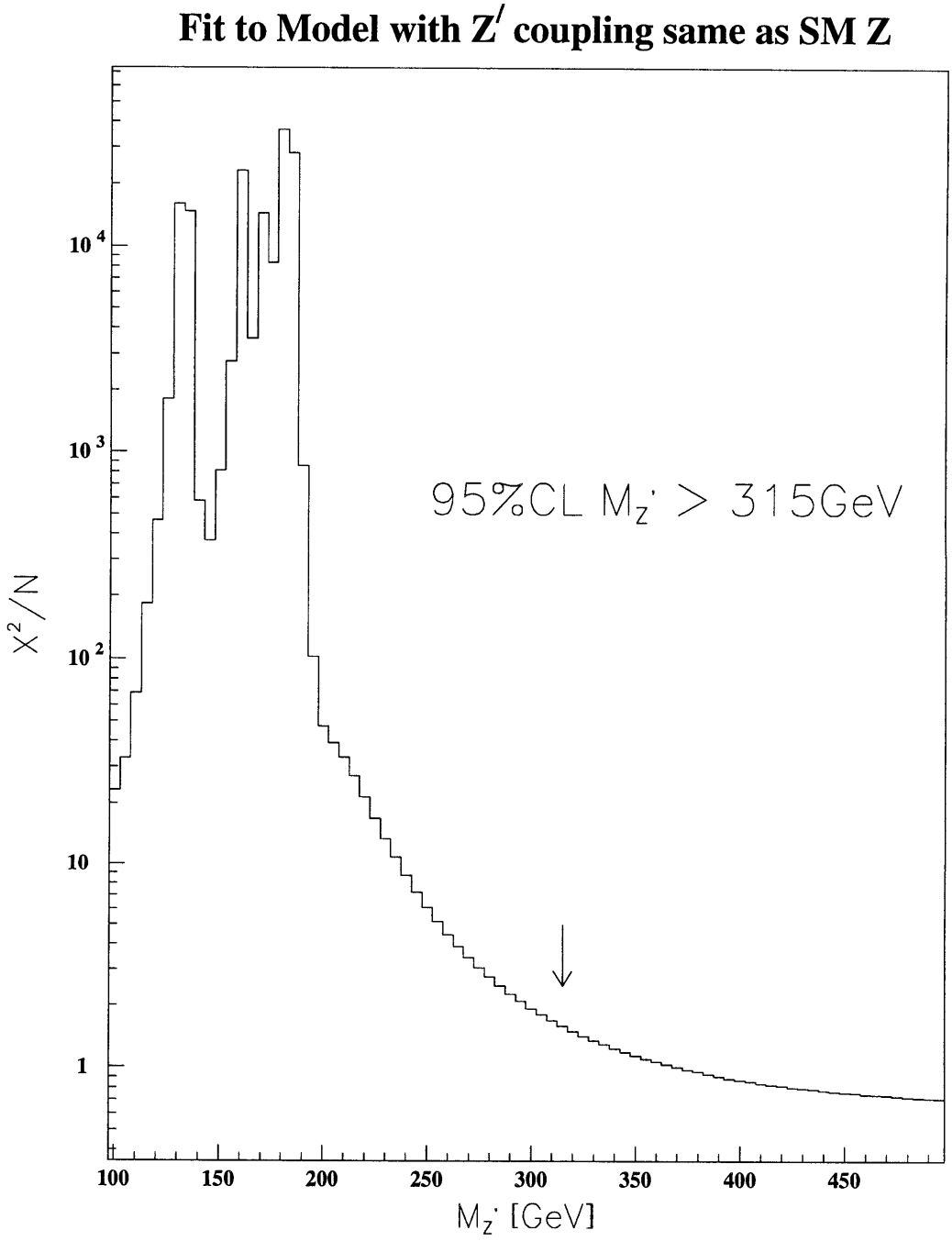

Figure 29: χ^2/N of a fit of the cross section and asymmetry data to a model in which a Z' has the exact same coupling to leptons as the SM Z.

can be visually inspected in Figure 31. A Monte Carlo [100, 101, 39] with a 90GeVexcited muon at $\sqrt{s}$ =182.7GeVis also shown in the plot. In the Monte Carlo, it was assumed that excited leptons have the same coupling as SM leptons to the Z and photon [102]. The cross section for excited lepton pair production assuming SM coupling at this energy is $0.772pb$. The selection efficiency for the hypothetical excited muon, μ^*, is 0.76. The 95% upper limit confidence level on the cross section times branching ratio of a 90GeV μ^* into a muon and photon is 0.02pb. Another analysis [103] recently found similar results.

One can also search for single production of excited muons, Figure 32. The same procedure is followed as in the double production search except that the photon is required to be in the barrel region of the electromagnetic calorimeter, $\sin\theta > 0.707$, which eliminates most of the ISR. The SM expectation is 15.25 events after cuts, or 30.5 entries in the histogram, which could be compared with the 18 events selected in the data. $\mu\mu^*$ production with a μ^* mass less than 90GeV has already been ruled out by LEP1 data alone [21]. Between 90GeVand 165GeV, the single μ^* selection efficiency is close to 61%, but it drops precipitously as the μ^* mass approaches the beam energy because of the pre-selection muon momentum cut. The cross section times branching ratio limits for three mass ranges are seen in Figure 32. The limits are less stringent than the excited lepton pair limits because of the large SM "background".

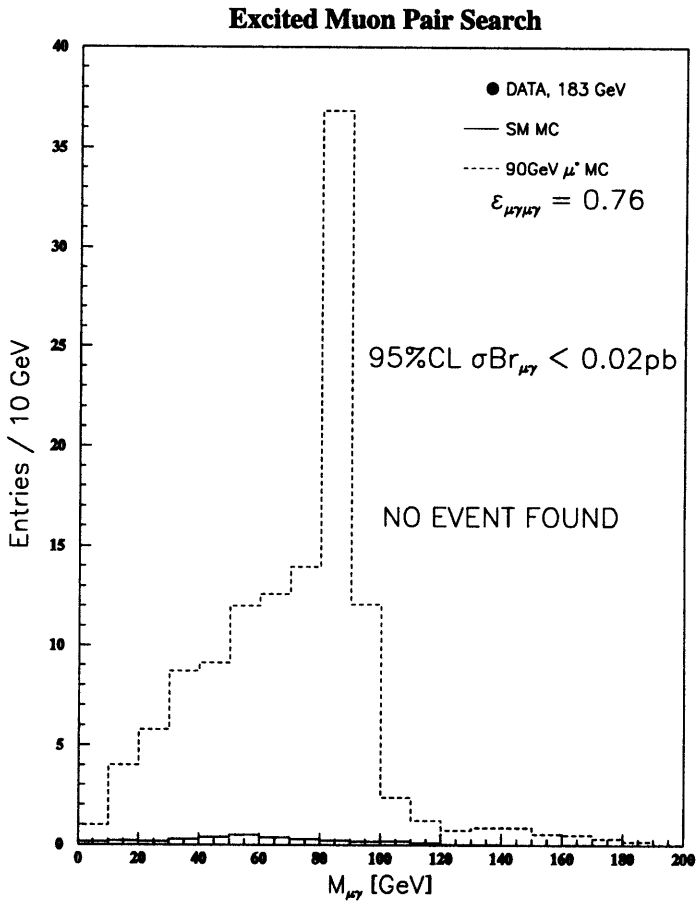

Figure 30: The $M_{\mu\gamma}$ invariant mass of events with two muons and two photons. No data event satisfies the cuts. The SM Monte Carlo (Tables 1 and 2) luminosity weighted expectation is 0.8 events. Also shown is a Monte Carlo with a 90GeV μ^* in which it is assumed the excited muon couples to the photon and Z with the same strength as a SM lepton [102]. The excited muon pair selection efficiency for the search, determined from the excited lepton Monte Carlo is 0.76. The shape of the excited lepton distribution is cause by the ghost combination (four entries per event because of the two possible pairings) and the detector resolution.

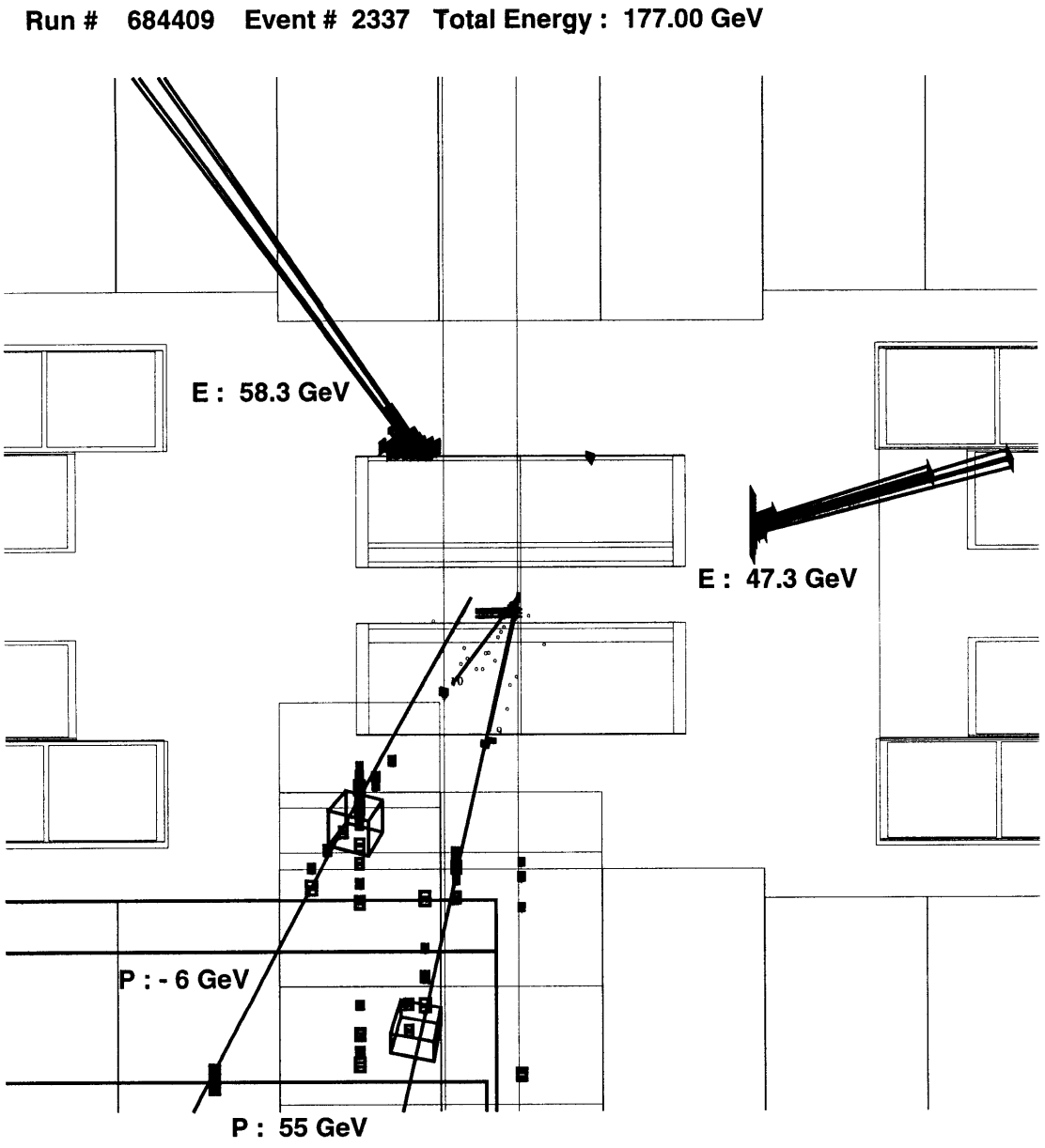

Figure 31: The only event with two photons passing the 20GeV energy cut; the event is not selected as an excited muon-pair candidate event because one muon does not pass the 10GeV momentum cut. The two sets of muon-photon invariant mass combinations are: a) 107 and 31GeVand b) 92 and 31GeV. The invariant mass of the two photons is 82.5GeV. Note: the bad Z vertex fit of the lower momentum muon track is the result of a hard multiple scattering in the hadron calorimeter. In addition, the momentum of the low momentum track is also measured to be 6GeV in the inner tracker which eliminates the possibility of a poor momentum fit in the muon chambers and confirms the event is not an excited muon-pair.

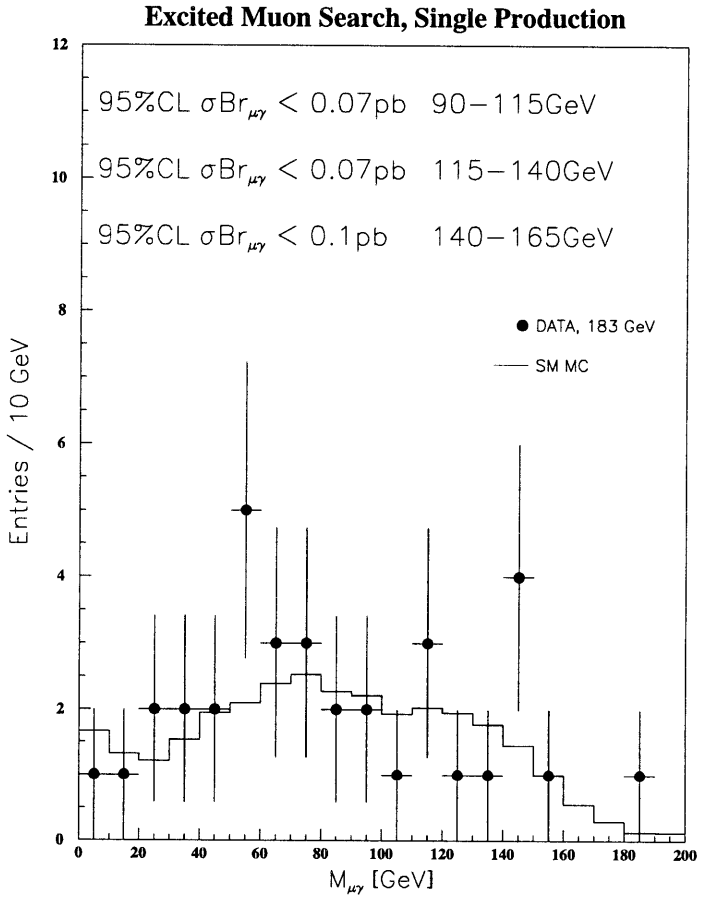

Figure 32: The $M_{\mu\gamma}$ invariant mass of events with two muons and one photon. There are 18 events in the data, i.e. 36 entries in the histogram. The SM Monte Carlo luminosity weighted expectation is 15.25 events (30.5 entries). Limits on the cross section times branching ratio for electromagnetic de-excitation of the excited muon are shown for three ranges.

6 Summary

The cross section and forward-backward charge asymmetry for the process $e^+e^- \to \mu^+\mu^-(n\gamma)$ have been measured at the highest center of mass energies to date, which ranged from 130 to 183GeV. The data was obtained from $85pb^{-1}$ of integrated luminosity collected with the L3 detector. The measurements agree with the Standard Model prediction in the new high energy range explored: $\chi^2_{SM}/N = .61$ with 10 degrees of freedom. A mass limit on an additional heavy, neutral gauge boson of $M_{Z'} > 315$GeV is set using muon pair production alone, rising to $M_{Z'} > 805$GeV when all final states are considered. Excited muon pair-production with electromagnetic coupling is excluded up to 183GeV at the 95% CL: $\sigma_{\mu\gamma} \times Br_{\mu\gamma} < 0.02$pb, and single excited muon production is excluded in the mass range 140 GeV $< M_{\mu*} <$ 165 GeV at the 95% CL: $\sigma_{\mu\gamma} \times Br_{\mu\gamma} < 0.10$pb.

7 Acknowledgments

There are hundreds of physicists, engineers, and technicians in the L3 collaboration, many of whom I have never even met. I warmly thank every collaborator who has or is doing his job to the best of his ability; thanks to them, L3 has taken data.

Certain people have marked my personal research experience more than others. Making an incomplete list: I thank my advisor Prof. Ulrich Becker for teaching me not every problem needs to be solved with a computer, I thank Dr. Yuan-Hann Chang for teaching me it is better to tell everyone what you do not know instead of what you do, I thank Prof. Alexei Lebedev for teaching me it is always better to first try and solve the exact problem before grabbing the back of an envelope, I thank Dr. J.J. Blaising for helping me keep the nature of my hardware responsibilities in perspective, I thank Dr. Joseph Burger for his dedicated work in the muon group, I thank Prof. Samuel Ting for the opportunity to work in the EMI group, and I thank Prof. Peter Fisher for teaching the MIT graduate students a class about experimental particle physics at CERN. In addition, I thank Arne Robohm for letting me use his Feynman diagrams and for many helpful discussions, and I thank, in alphabetical order, Michel Fabre, Klaus Freudenreich, Paul de Jong, Cary Lapoint, Dave Luckey, Christoph Paus, Sabine Riemann, Thorsten Siedenburg, and Yoshi Uchida for many enlightening conversations.

The thesis is dedicated to my wife Johanne and my son Timothé.

Appendix A

A Additional Figures

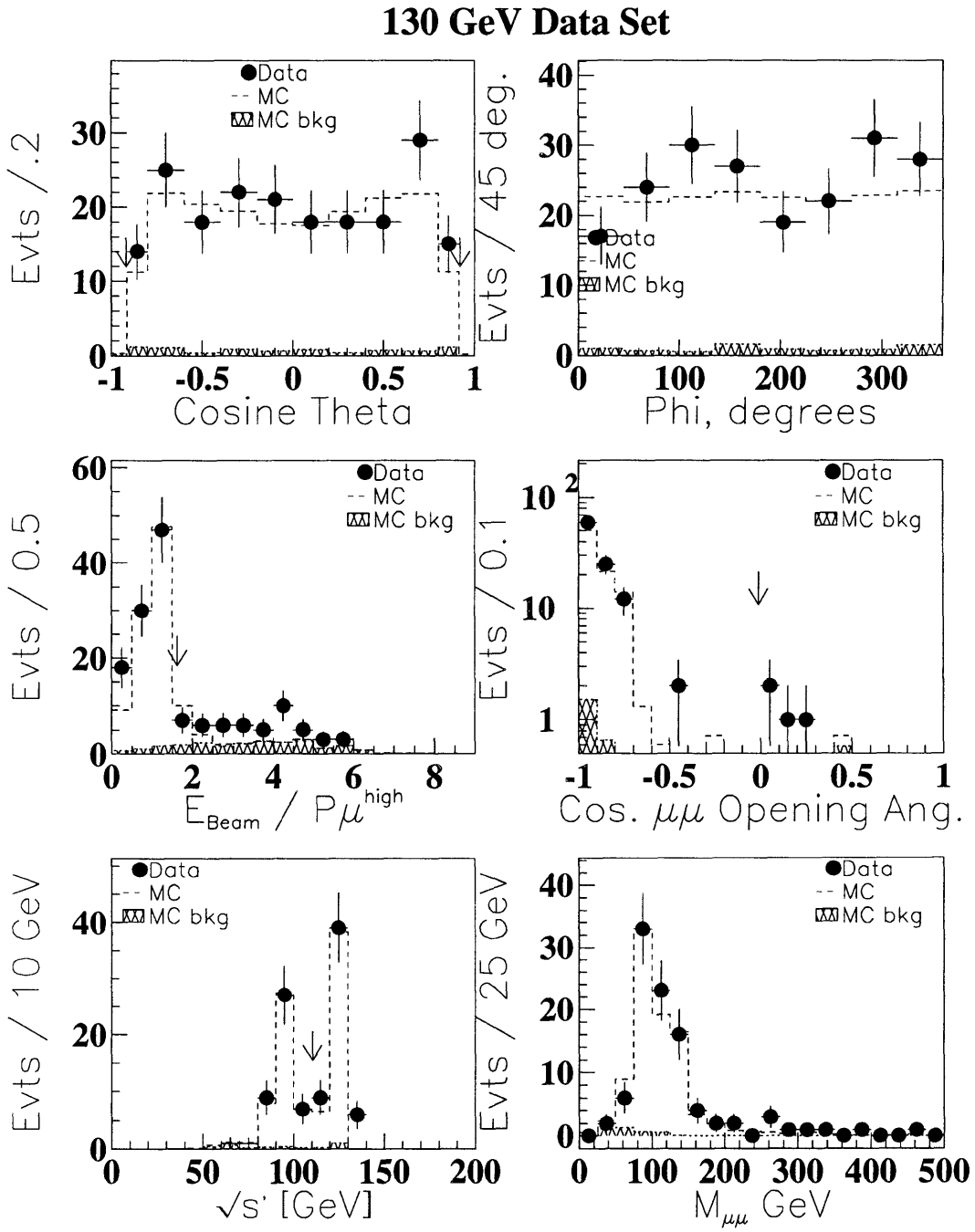

Figure 33: All selected muon candidates. Cuts indicated with an arrow. Upper left: $\cos\theta$, last bin ends at cos(24°). Upper right: ϕ. Center left: Highest momentum muon. Center right: $\cos\theta^{\mu\mu}_{opening}$. Bottom left: $\sqrt{s'}$. Bottom right: Measured $\mu\mu$ invariant mass.

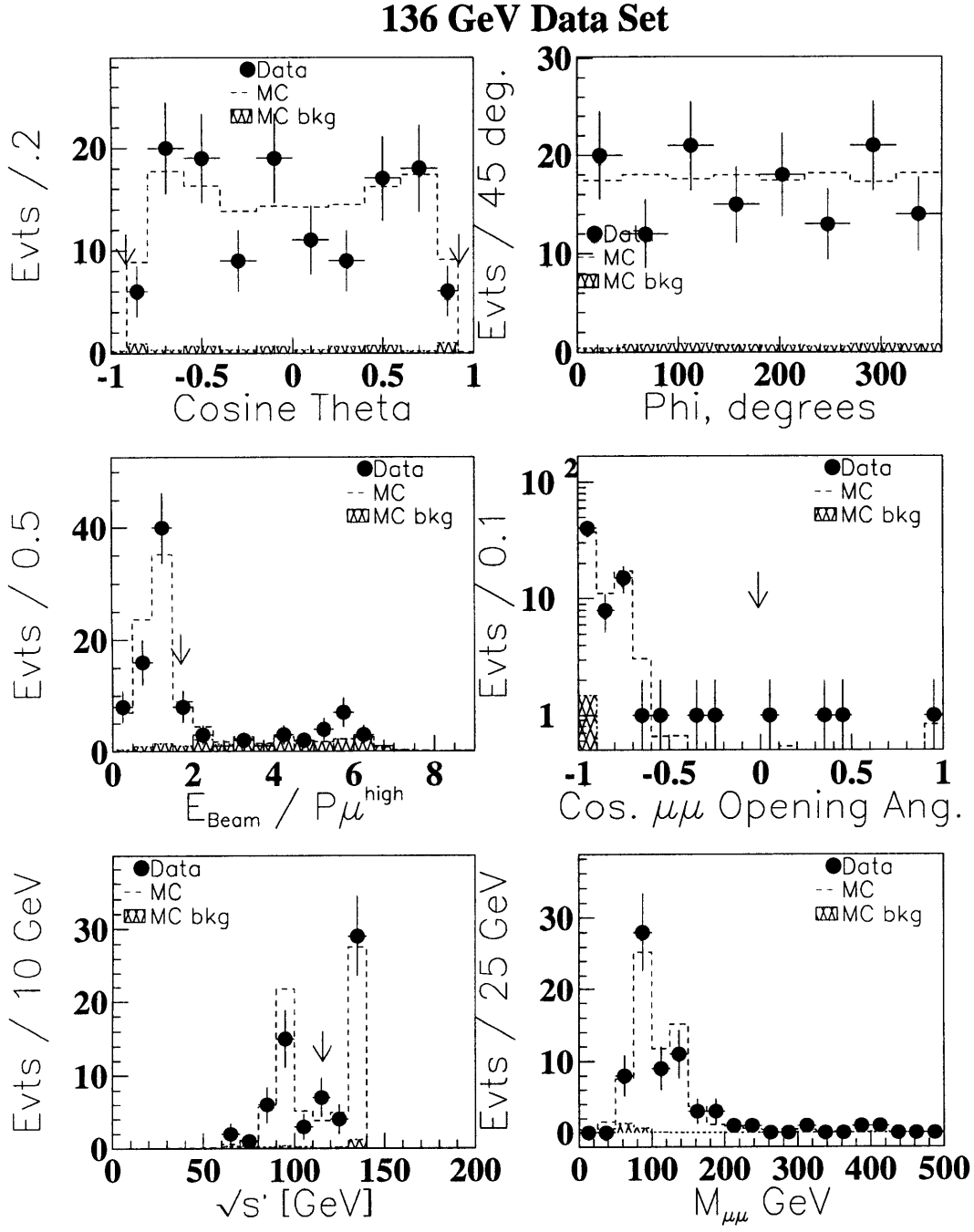

Figure 34: All selected muon candidates. Cuts indicated with an arrow. Upper left: $\cos\theta$, last bin ends at cos(24°). Upper right: ϕ. Center left: Highest momentum muon. Center right: $\cos\theta^{\mu\mu}_{opening}$. Bottom left: $\sqrt{s'}$. Bottom right: Measured $\mu\mu$ invariant mass.

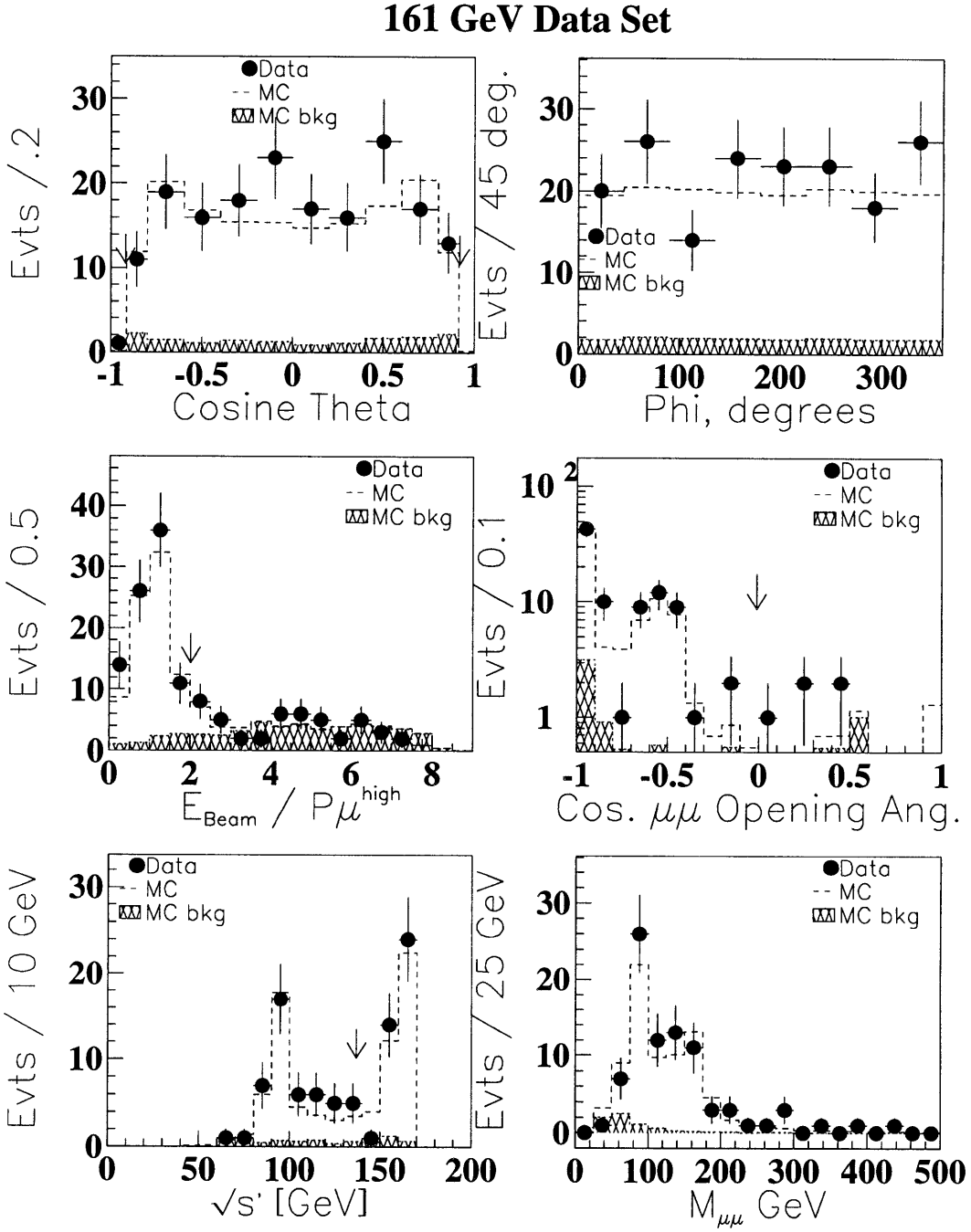

Figure 35: All selected muon candidates. Cuts indicated with an arrow. Upper left: $\cos\theta$, last bin ends at cos(24°). Upper right: ϕ. Center left: Highest momentum muon. Center right: $\cos\theta^{\mu\mu}_{opening}$. Bottom left: $\sqrt{s'}$. Bottom right: Measured $\mu\mu$ invariant mass.

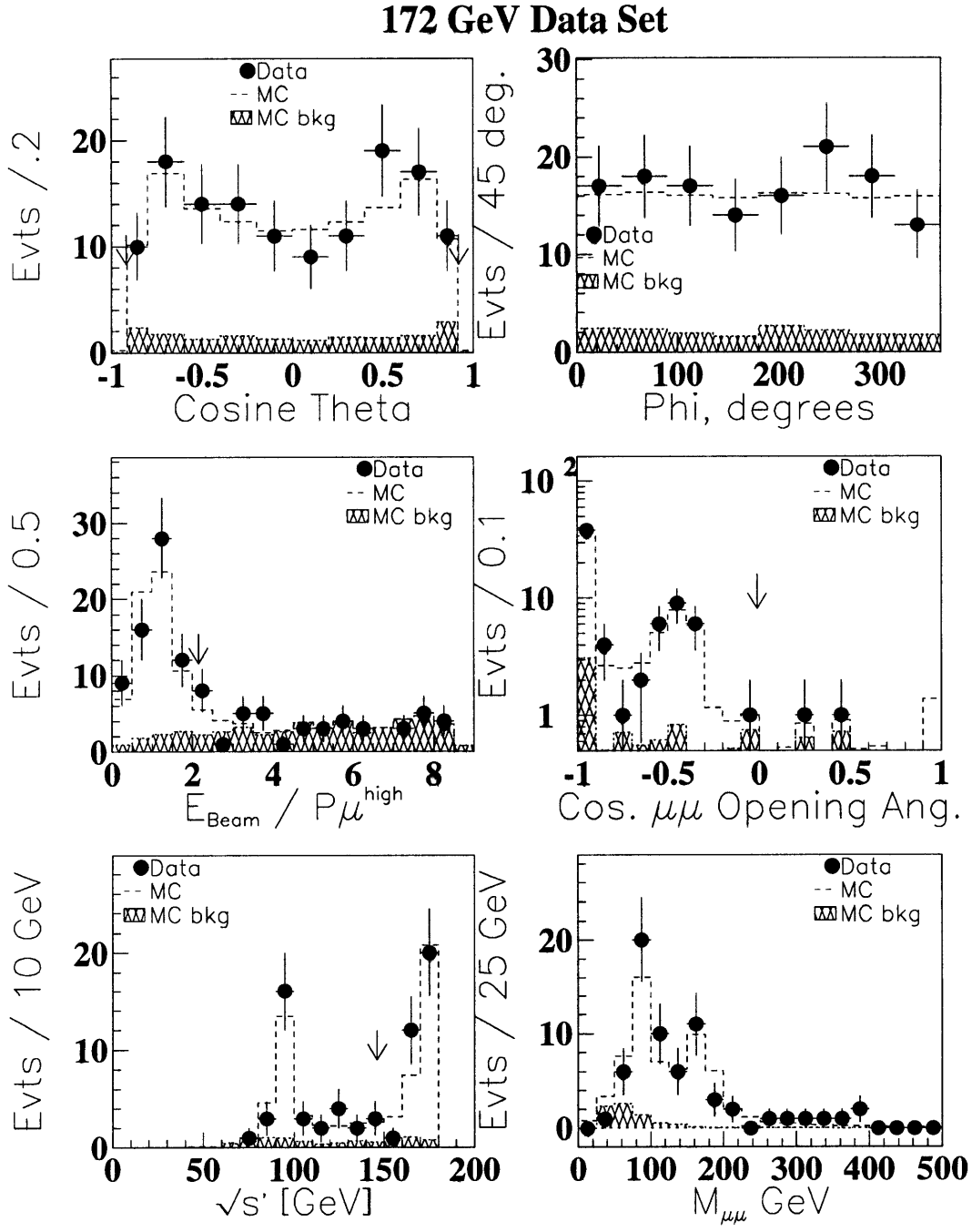

Figure 36: All selected muon candidates. Cuts indicated with an arrow. Upper left: $\cos\theta$, last bin ends at cos(24°). Upper right: ϕ. Center left: Highest momentum muon. Center right: $\cos\theta^{\mu\mu}_{opening}$. Bottom left: $\sqrt{s'}$. Bottom right: Measured $\mu\mu$ invariant mass.

Appendix B

B Uncorrelated Trigger Approximation

The backup trigger (energy × inner tracker) to the muon trigger covers a larger solid angle than the muon trigger; consequently, for trigger studies, it is required that the candidate muon pair event have at least one selected muon track reconstructed in the muon chambers. As a result, detection gaps between the muon chambers are not included as trigger inefficiency. After the events in the detection gaps are eliminated, let N_{muon} and N_{backup} define the sets of events with muon chamber triggers and backup muon triggers, respectively. Schematically, on has:

$$\begin{aligned} N_{total} &= N_{muon}.OR.N_{backup} \\ N_{both} &= N_{muon}.AND.N_{backup} \end{aligned}$$

N_{total} is the total number of events and N_{both} are the events with both triggers. The following relations are true if the triggers are uncorrelated:

$$\begin{aligned} \epsilon_{muon} &= \frac{N_{both}}{N_{backup}} \\ \epsilon_{backup} &= \frac{N_{both}}{N_{muon}} \\ \epsilon_{level_1} &= \epsilon_{muon} + \epsilon_{backup} - \epsilon_{muon}\epsilon_{backup} \\ \sigma_{\epsilon_{muon}} &= \sqrt{\frac{\epsilon_{muon}(1-\epsilon_{muon})}{N_{backup}}} \\ \sigma_{\epsilon_{backup}} &= \sqrt{\frac{\epsilon_{backup}(1-\epsilon_{backup})}{N_{muon}}} \\ \sigma_{\epsilon_{level_1}} &= \sqrt{[(1-\epsilon_{muon})\sigma_{\epsilon_{backup}}]^2 + [(1-\epsilon_{backup})\sigma_{\epsilon_{muon}}]^2} \end{aligned}$$

Appendix C

C level-1 Muon Trigger

The level-1 muon trigger consists of two major branches, the barrel muon trigger processor [71, 72] and the endcap muon trigger processor [104]. The processors are physically independent from one another, although intermediate results from the barrel muon trigger processor are sent to the endcap muon trigger processor. One of the author's roles at L3 consisted of maintaining and monitoring the level-1 muon trigger processors.

C.1 Barrel Muon Trigger

The amplified and discriminated timing signals originating from the P and Z chamber wires are picked off by receivers before being encoded by TDCs and sent to trigger cards which, to reduce the number of channels by a factor of two, make a logical $.OR.$ of neighboring wire pairs. The 120 wires in a Z chamber become 60 "trigger wires" for the trigger processor. The P chambers cells with 16, 24, and 16 wires have 8, 12, and 8 equivalent "trigger wires" per cell.

The $.OR.$ed signals are latched every beam crossing. The characteristic drift time in the P and Z drift chamber cells is used for gating the latch. Before 1994, the exact value or the trigger latches were $1.31\mu s$ and $2.41\mu s$ for P and Z wires. The gates were increased to $2.09\mu s$ and $3.19\mu s$ to handle multiple closely spaced particle bunches in the so called bunch train mode running of LEP in 1995.

The threshold for a P chamber cell to become a trigger hit is two "trigger wires". The threshold for a Z chamber cells to become a trigger hit is obviously only one "trigger wire".

The triggered cells, i.e. the ones satisfying the threshold requirement, are sent into data arrays which function as one to one buffer maps in RAM memory of the chamber's cell structure. Programmable Logic Units (PLUs) have access to these memories. The PLUs check 165 P and 148 Z track patterns in the P (R-ϕ) and Z projection of each octant. A track pattern or "road" is a combination of cell hits from a 2GeV (or more) track originating from the vertex. There are track patterns which cross over into neighboring octants, so a PLU has access to three octants worth of data arrays.

There are three types of level-1 barrel muon triggers: the dimuon trigger, the small angle dimuon trigger, and the single muon trigger. Each has its own coincidence pattern checked in the 3 P and 4 Z layers for the 165 P and 148 Z track patterns in each octant (Table 10). In the Z chambers, it is also recorded if the coincidence was in the first set of 74 Z track patterns (backward hemisphere) or in the last set of 74 Z track patterns (forward hemisphere).

For the single muon trigger, after the track pattern search, 165-fold and 148-fold logical $.OR.$s

Barrel Track Pattern Coincidence		
Sub-trigger	P coincidence	Z coincidence
Single muon trigger	2 out of 3 layers	3 out of 4 layers
Dimuon trigger	2 out of 3 layers	No requirement
Small angle dimuon trigger	First layer	1 out of 2 first layers

Table 10: Barrel muon chamber layer coincidence requirements to be satisfied by at least one of the 165 P and 148 Z track patterns. The 313 track patterns are checked in each of the 8 barrel muon octants every beam crossing.

are made from the P and Z track pattern coincidence decisions in each of the 8 octants. If there is a P and Z trigger component in the same octant, the single muon trigger fires. For the dimuon trigger, 165-fold logical $.OR.$s are made out of the P track pattern coincidence decisions in each octant. Any two octants with P trigger components except adjacent octants fire the dimuon trigger. The single muon trigger and dimuon trigger P track pattern coincidence conditions happen to be the same. For the small angle dimuon trigger, 165-fold logical $.OR.$s are made of the P track pattern coincidence decisions in each octant. Forward and backward 74-fold logical $.OR.$s are made out of the Z track pattern coincidence decisions in each octant. A P-Z match forward and a P-Z match backward fires the small angle dimuon trigger. The match must be back-to-back $\pm$ one octant in phi. The final level-1 barrel muon chamber trigger is the logical $.OR.$ of the three sub-trigger decisions.

The last component to the level-1 barrel muon trigger consists of the barrel scintillators [58]. Whenever any one of the 30 barrel scintillator counters has a trigger hit in coincidence with a level-1 barrel muon chamber trigger, the event is sent to level-2. Clearly, one prefers not use the barrel scintillators as part of the level-1 "barrel muon chamber" trigger decision because of detection gaps in the horizontal plane. Also, the barrel scintillators end at a polar angle of 34° whereas the barrel muon chambers end at a polar angle of 24°. The barrel small angle dimuon trigger is thereby clipped off at a polar angle of 34°.

The barrel scintillator coincidence requirement is included because the level-1 trigger throughput of the system is limited to 25Hz by the hadron calorimeter DAQ. Reading out the muon chamber triggers at 20 Hz instead of 2Hz (which is the reduction factor caused by $.AND.$ing the barrel muon chamber trigger with the barrel scintillators), would result in an unacceptable 50% deadtime in the readout. One in ten beam crossings has a superimposed Uranium noise hit in the scintillators, hence the majority of the barrel muon triggers sent to level-2 are Uranium noise hits in the scintillators in coincidence with out-of-time cosmic rays in the barrel muon chambers. These noise triggers are rejected with 75% efficiency by the higher trigger levels.

C.2 Endcap Muon Trigger

Resistive plate chambers (RPCs), endcap scintillators, barrel scintillators, endcap muon chambers trigger hits, and elements composed of barrel muon chamber trigger cells are all used as ingredients for the level-1 endcap muon trigger algorithm. Erasable Programmable Read Only Memories (EPROMs) are used instead of PLUs. There are nine types of endcap muon triggers, five dimuon triggers and four single muon triggers [105, 104].

The RPCs are attached to the outer two layers of the endcap muon chambers. A track pattern matrix between the two layers pointing to the L3 vertex is checked for coincidence in the two layers. The RPC gates are 90ns wide around the beam crossing [54]. There are 16 RPC trigger decisions made in total, 8 in the forward octants and 8 in the backward octants.

The endcap scintillators (Figure 15) use the same gating as the barrel scintillators [79]. There are 16 on the forward side and 16 on the backward side. As opposed to the level-1 barrel muon trigger, the level-1 endcap muon trigger processor performs a matching with the barrel and endcap scintillator hits.

The track pattern search in the endcap muon chambers is much simpler than in the barrel; the entire chamber is the track pattern. Eight timing hits anywhere in a chamber cause the endcap chamber trigger to fire, hence there are in total 16×2×3 endcap muon chamber triggers.

The barrel muon chamber trigger processor sends many intermediate results to the endcap muon trigger processor; a logical *.OR.* of the MI trigger cells in each octant; a logical *.OR.* of the MM trigger cells in each octant; the P component of the single and dimuon barrel sub-triggers of each octant; a logical *.OR.* of the forward innermost two Z chambers layer trigger cell hits in each octant; a logical *.OR.* of the backward innermost two Z chambers layer trigger cell hits in each octant; and the sixteen barrel small angle dimuon trigger sub-trigger decisions.

There are four endcap single muon triggers (Table 11), each one being the logical *.OR.* of 16 sub-decisions, 8 forward and 8 backward. Three of the four single muon triggers cover 24 to 34 degrees: RPC *.AND.* endcap scintillator, RPC *.AND.* endcap muon chamber trigger, and endcap scintillator *.AND.* endcap muon chamber. All combinations of two out of three were chosen to reduce inefficiencies. The remaining single muon trigger covers the 34 to 45 degree region, picking up exactly where the barrel single muon trigger stops, at 45 degrees. Slightly more complicated than the previous three, it is composed of the following trigger hits: barrel scintillator *.AND.* the innermost barrel P layer *.AND.* one of the innermost two barrel Z layers *.AND.* the innermost endcap muon chamber *.AND.* either the middle endcap muon chamber *.OR.* the middle barrel muon chamber.

The dimuon triggers are listed in Table 11. The collinearity requirements have been set to their loosest possible values. A muon anywhere in the forward half along with a second muon anywhere in the backward half will fire the trigger. The same is true when both muons are forward or both

Endcap Single Muon Triggers	
RPC *.AND.* endcap scintillator	
RPC *.AND.* endcap muon chamber	
endcap scintillator *.AND.* endcap muon chamber	
barrel scintillator *.AND.* endcap muon chamber *.AND.* barrel muon chamber	
Endcap Dimuon Triggers	
First muon	Second muon
RPC forward (backward) RPC forward (backward)	RPC backward (forward) RPC forward (backward)
EC sci. forward (backward) EC sci. forward (backward)	small angle barrel backward (forward) small angle barrel forward (backward)
EC sci fwb ch. forward (backward)	RPC backward (forward)
fwb ch-endcap sci forward (backward) fwb ch-endcap sci forward (backward)	fwb ch-endcap sci. backward (forward) fwb ch-endcap sci. forward (backward)
RPC	barrel P track

Table 11: Endcap muon triggers.

muons are backward except when the triggered octants are neighbors. The RPC dimuon trigger with both muons on the forward side or both muons on the backward side, however, is much too sensitive to low energy LEP background and has always been disabled. Because of the last endcap dimuon trigger listed in Table 11, the "endcap" dimuon triggers cover the *entire* fiducial volume of the muon detector as long as there is at least one endcap muon.

The dimuon triggers are not composed of single muon triggers, for the single muon triggers have been made tight in order to keep the background low. Tight single muon triggers and loose dimuon trigger are complementary when triggering on W^+W^- or $\mu^+\mu^-$.

The total level-1 endcap muon trigger rates is the logical *.OR.* of the 9 sub-triggers just described. The typical level-1 endcap muon trigger rate is 1Hz, but is sensitive to poor beam conditions rising occasionally to as much as 5Hz. 50% of the level-1 endcap muon triggers are rejected by the level-3 trigger (Level-2 is by-passed, for the trigger information is already efficiently used by level-1.).

C.3 Discussion

The barrel muon trigger processor is extremely flexible. The barrel PLUs are loaded with the trigger algorithm before every physics fill. Fortunately, the flexibility has not yet been needed, for the LEP background conditions have been quite good. The endcap EPROMs have to be re-burned to change the algorithm, but there are enable bits which allow one tighten the the sub-triggers. The system integration would have been better if, when the endcap muon chambers were installed, the barrel trigger processors would have been eliminated. The majority of the barrel intermediate decisions are already sent to the endcap trigger processor, and EPROMs greatly reduce the number of wires and the number of modules. On the other hand, if ever the trigger algorithm would have to be changed,

the EPROMs must re-burned, which is unacceptable during a physics run. Another solution would have been to use Field Programmable Gate Arrays (FPGAs), a newer technology which is quickly becoming the standard. With FPGAs, one has complete flexibility and a small number of external wires, the advantages of both systems.

A FORTRAN package simulating the trigger processor's algorithm can be obtained from the author by request (bryan.smith@cern.ch).

m_Z	m_t	m_H	$1/\alpha(m_Z)$	α_s	G_F
91188.1 MeV	175.6 GeV	300 GeV	128.896	0.1221	$1.66388 \cdot 10^{-5}$ GeV^{-2}

Table 12: Input for the MC.

ZFITTER flag values									
AFBC	1	SCAL	0	SCRE	0	AMT4	3	BORN	0
BOXD	1	CONV	1	FINR	1	FOT2	3	GAMS	1
INCL	0	INTF	1	BARB	2	PART	0	POWR	1
PRNT	1	ALEM	2	QCDC	2	VPOL	1	WEAK	1
FTJR	1	EXPR	0	EXPF	0	HIGS	0	AFMT	1

Table 13: For completeness, ZFITTER version 5.0 parameters used to obtain Standard Model predictions.

Appendix D

D Monte Carlo

The input to the Monte Carlo for obtaining Standard Model predictions are listed in Table 12. In addition, the exact ZFITTER program [31, 28, 32, 27] parameters used for SM predictions can be found in Table 13. By examining the shape and ratio of the event generator, KORALZ [30], and the semi-analytical calculation, ZFITTER, (Figure 37) one concludes the efficiency calculations would be biased if the ZFITTER predictions at the settings in Table 13 are accurate. KORALZ makes higher order QED calculations only in the *absence* of ISR-FSR interference. KORALZ also makes approximations in the calculation of the FSR contribution (hence the sharpening at the Z peak). If one sets the ZFITTER parameters $INTF = 0$ and $FINR = 0$, corresponding to neglecting initial-final state interference and approximation the final state radiation contribution by a correction factor (instead of working out the complete convolution integral) the agreement with KORALZ improves (Figure 38). The programs used to obtain the background estimates in the events candidates are listed in Table 14.

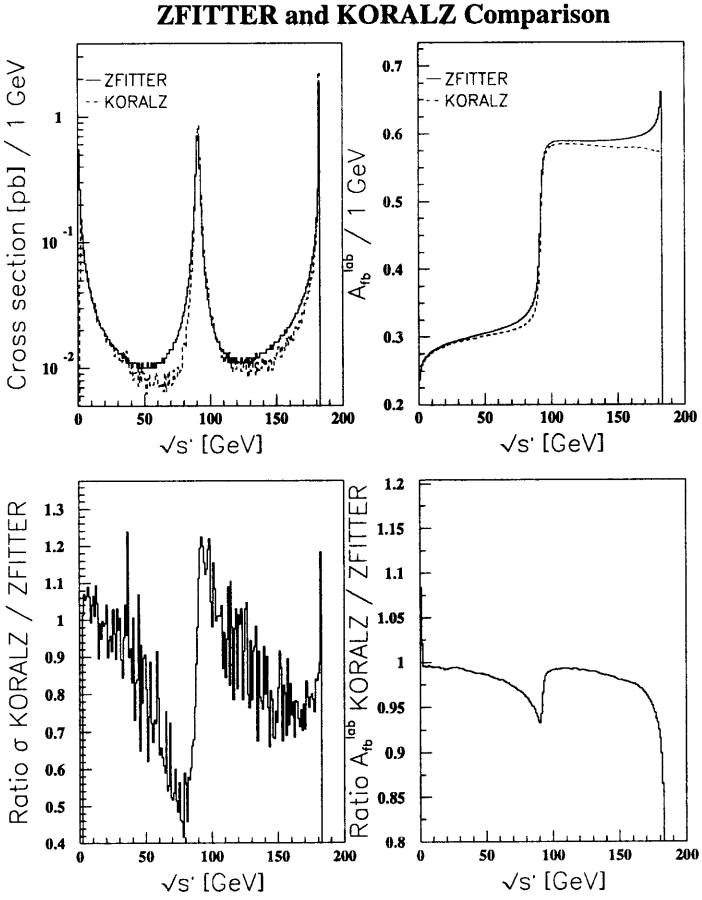

Figure 37: Comparison of KORALZ and ZFITTER at $\sqrt{s}$ =183GeV. Because of the cut in the KORALZ event generator at very low $\mu^+\mu^-(n\gamma)$ invariant mass, the KORALZ number of events is normalized to the ZFITTER $\sqrt{s'} > 0.1\sqrt{s}$ cross section value. The structure around the return to Z events is caused by KORALZ approximation the FSR radiation contribution. The difference above $\sqrt{s'} > .9\sqrt{s}$ is caused by KORALZ neglecting ISR-FSR interference. Notice the log scale on the upper left plot and the suppressed zero in all of the plots.

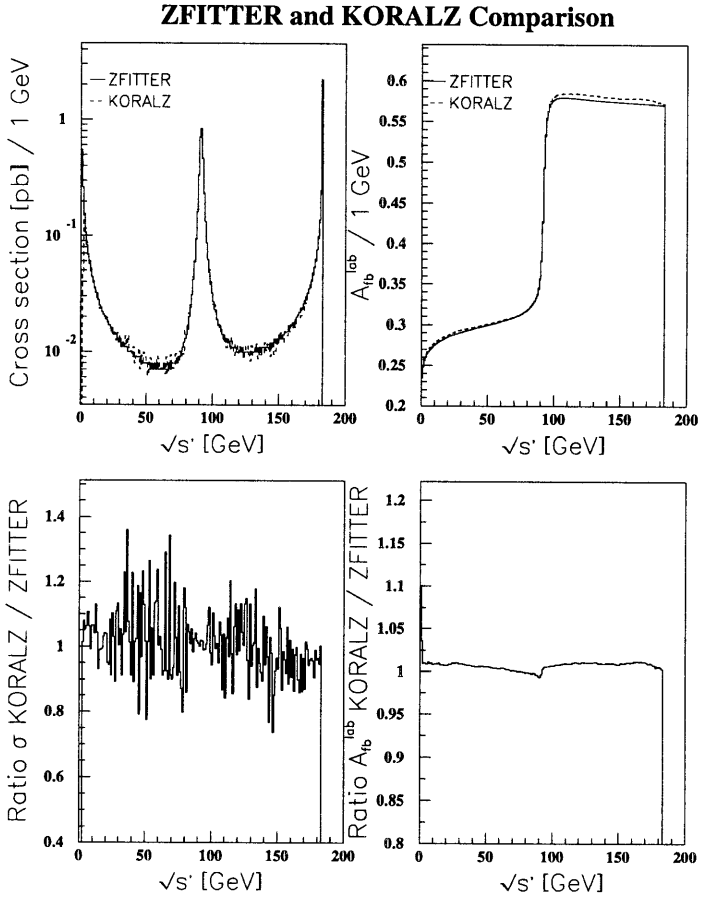

Figure 38: Same as Figure 37, except ZFITTER parameters $INTF = 0$ and $FINR = 0$. As expected, agreement improves. Notice the log scale on the upper left plot and the suppressed zero in all of the plots.

Reaction	Monte Carlo
Primary backgrounds	
$\tau^+\tau^-(\gamma)$	KoralZ [30]
$W^+W^-(n\gamma)$	KoralW [106, 107]
$e^+e^-\mu^+\mu^-$	Diag36 [108]
Secondary backgrounds	
q^+q^-	JETSET [109, 110]
ZZ	JETSET [109, 110]
Ze^+e^-	JETSET [109, 110]
Extremely small backgrounds	
$e^+e^-\tau^+\tau^-$	Diag36 [108]
All other four fermion.	EXCALIBUR [111]

Table 14: Set of Monte Carlo generators employed for background estimation.

Appendix E

E The Standard Model of Electroweak Interactions

E.1 Historical Overview

Quantum electrodynamics, QED, pioneered in the 1940s by Feynman, Schwinger and Tomonaga [112, 113, 114] was "renormalizable", i.e. infinities in propagators could be controlled such that high precision predictions of processes involving charged particles and photons could be made. Could a theory be developed for the weak nuclear force? Schwinger made the first attempt in 1957 [115] to unite electromagnetic interactions of QED with the weak nuclear force. In this model, weak interactions were mediated by massive charged vector particles. Glashow [116] and Salam [117] independently proposed a similar model which included the idea of gauge invariance, first proposed by Yang and Mills in 1954 [118]. As well as the charged mediators, called W^+ and W^-, this model featured a massive neutral mediating particle, the Z^0, although neutral weak currents had not yet been observed. The masses of these particles were put in by hand and the theory was not renormalizable.

A method of "generating" gauge boson masses in a more natural way was found by Higgs [119, 120, 121] building on the work of Goldstone [122]. The Higgs mechanism led to the presence of massive scalars, Higgs particles. In 1967, Weinberg [123] and Salam [124] independently published an electroweak model for leptons using the Higgs mechanism. An extension to the quark sector was made by Glashow, Illiopoulos and Maiani by the suggestion of an as yet unobserved fourth quark [125]. The model was made anomaly free by introduction of the concept of color [126, 127] . The renormalizability of this theory was shown by 't Hooft [128].

The key to establishing the Glashow-Weinberg-Salam theory was the first observation of neutral weak currents in 1973 [129]. The first direct observation of the W and Z particles in 1983 at their predicted masses provided solid confirmation [130, 131]. Questions such as why there are three fermion generations with a rapidly increasing mass hierarchy, how does one accommodate massive neutrinos into the theory, and what is the structure of the, as of yet hypothetical, Higgs sector are examples of outstanding, potentially interrelated, issues which need to be resolved by further experimental work and theoretical interpretation.

E.2 Elements of Electroweak Theory

At present, matter is observed to consist of elementary fermions. An anti-particle exists for every fermion. The fermions are divided into three generations, each one comprising two leptons and two

quarks. The mass is the only quantum number which distinguishes the generations. Quarks and leptons are observed to interact by means of both charged and neutral currents. Parity violation experiments show that the charged current interaction is of a $V-A$ (vector - axial-vector) form, so only the left handed fermion spinor field component interacts with the charged current, whereas the neutral current has both left and right handed components. Interactions between the fermions are presently described by means of gauge theories. The elementary particles of the gauge fields are called gauge bosons.

Besides the fermion masses, quark mixing angles, and mass of the Higgs scaler, there are three other free parameters in the Standard Model of Electroweak Interactions. Once the parameters are set, comparison with experimental data can begin. The freedom to choose the remaining three parameters is large, yet it is customary to choose the following set: the Fermi constant, G_μ, defined by the muon lifetime; the fine structure constant at low energy, α, defined by Thomson scattering; and $\sin^2\theta_W$, the weak mixing angle. Assuming gauge invariant Higgs-gauge field interactions lead to mass terms for the vector bosons, $\sin^2\theta_W$ describes the rotation of the basic SU(2) and U(1) fields W_μ and B_μ, which yield the mass diagonalized photon, Z, and W fields:

$$\begin{aligned} A_\mu &= B_\mu \cos\theta_W - W_\mu^3 \sin\theta_W \\ Z_\mu &= B_\mu \sin\theta_W + W_\mu^3 \cos\theta_W \\ W_\mu^\pm &= \frac{1}{\sqrt{2}}(W_\mu^1 \pm W_\mu^2). \end{aligned}$$

The Higgs mechanism provides a relationship between θ_W and the masses of the gauge bosons,

$$\rho \equiv \frac{M_W^2}{M_Z^2 \cos^2\theta_W}. \tag{19}$$

In the minimal Standard Model $\rho = 1$. The coupling strengths g and g' of the SU(2) and U(1), respectively, are related to the electromagnetic strength $e = \sqrt{4\pi\alpha}$, via:

$$g \sin\theta_W = g' \cos\theta_W = e \tag{20}$$

Thus g and g' can be replaced by e and θ_W, parameters determined by experiment; furthermore, by requiring the calculations of weak charged current interactions to agree with the older Fermi $V-A$ theory, one sees how the three parameters are related to the mass of the W boson, M_W:

$$M_W^2 = \frac{\pi\alpha}{\sqrt{2} G_\mu \sin^2\theta_W} \tag{21}$$

The couplings of the photon, Z, and W, Figure 39, to fermions are given by $-ieQ_f\gamma_\mu$, $ie\gamma_\mu(v_f - a_f\gamma_5)$, and $ie\gamma_\mu(1-\gamma_5)/(2\sqrt{2}\sin\theta_W)$, respectively. The photon propagator is $-ig^{\mu\nu}/k^2$, and the W

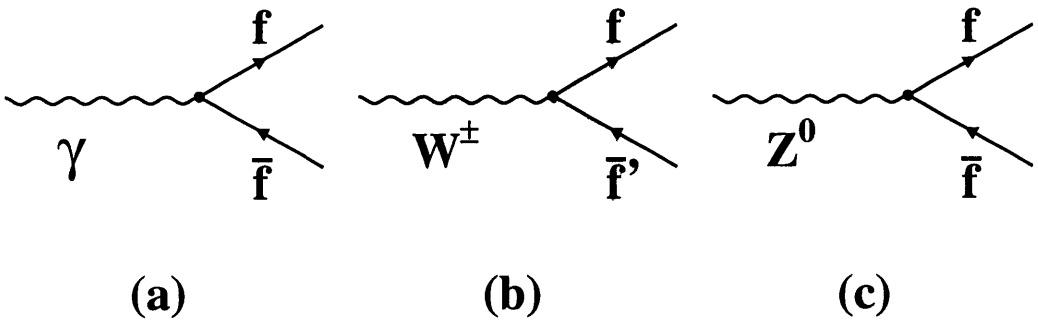

Figure 39: Feynman graphs for (a) electromagnetic, (b) charged current, and (c) neutral current interactions.

and Z propagator is $i(-g^{\mu\nu} + \frac{k^\mu k^\nu}{M^2})/(k^2 - M^2)$. The coupling constants v_f and a_f are

$$\begin{aligned} v_f &= \frac{I_3^f - 2Q_f \sin^2\theta_W}{2\sin\theta_W \cos\theta_W} \\ a_f &= \frac{I_3^f}{2\sin\theta_W \cos\theta_W} \end{aligned} \tag{22}$$

where I_3 is the third component of the weak isospin, Q_f is the fermion charge. I_3 is $\frac{1}{2}$ for up type quarks and neutrinos and $-\frac{1}{2}$ for all other fermions. v_f and a_f just defined provide the connection with the tree-level calculations presented in Section 2.1.1.

References

[1] L3 Collaboration, B. Adeva *et al.*. The Construction of the L3 Experiment. *Nuclear Instruments and Methods A*, 289:35+, 1990.

[2] L3 Collaboration, O. Adriani *et al.*. Results from the L3 Experiment at LEP. *Physics Reports*, 236:1+, 1993.

[3] The LEP design group. The LEP Main Ring. LEP Design Report 1, CERN, Geneva, June 1984.

[4] The LEP design group. The LEP Injector Chain. LEP Design Report 29, CERN, Geneva, 1983.

[5] D. Decamp *et al.*. ALEPH: A Detector for Electron-Positron Annihilations at LEP. *Nuclear Instruments and Methods A*, 294:121+, 1990.

[6] P. Aarnio *et al.*. The Delphi Detector at LEP. *Nuclear Instruments and Methods A*, 303:233+, 1991.

[7] K. Ahmet *et al.*. The OPAL Detector at LEP. *Nuclear Instruments and Methods A*, 305:275+, 1990.

[8] The LEP Collaborations and The LEP Electroweak Working Group and the SLD Heavy Flavour Group. A Combination of Preliminary LEP Electroweak Measurements and Constraints on the Standard Model. Technical Report 154, CERN PPE, 1997.

[9] L3 Collaboration B. Adeva *et al.*. Measurement of Cross Sections and Leptonic Forward-Backward Asymmetries at the Z Pole and Determination of Electroweak Parameters. *Zeitschrift für Physik C*, 62:551+, 1994.

[10] L3 Collaboration: M. Acciarri *et al.*. Determination of Electroweak Parameters from the Measurement of Hadronic and Leptonic Cross Sections and Forward-Backward Asymmetries at the Z Resonance and Determination of Electroweak Parameters, 1997. To be published in European Physics Journal C.

[11] L3 Collaboration M. Acciarri *et al.*. Measurement of Hadron and Lepton-Pair Production at 161 GeV $< \sqrt{s} <$ 172 GeV at LEP. *Physics Letters B*, 407:361+, 1997.

[12] L3 Collaboration M. Acciarri *et al.*. Measurement of Hadron and Lepton-Pair Production at 130 GeV $< \sqrt{s} <$ 140 GeV at LEP. *Physics Letters B*, 370:195+, 1996.

[13] L3 Collaboration M. Acciarri *et al.*. Measurement of Muon Pair Production at 50 GeV $< \sqrt{s} <$ 86 GeV at LEP. *Physics Letters B*, 374:331+, 1996.

[14] OPAL Collaboration K. Ackerstaff *et al.*. Measurement of Cross-sections and Asymmetries in e^+e^- Collisions at 130-140 GeV Centre-of-mass Energy. *Physics Letters B*, 376:232+, 1996.

[15] OPAL Collaboration K. Ackerstaff *et al.*. Production of Fermion-pair Events in e^+e^- at 161 GeV Centre-of-mass Energy. *Physics Letters B*, 391:221+, 1997.

[16] OPAL Collaboration K. Ackerstaff *et al.*. Tests of the Standard Model and Constraints on New Physics from Measurements of Fermion Pair Production at 130-GeV to 172 GeV at LEP. CERN PPE 101, CERN, 1997. Submitted to *Zeitschrift für Physik C.*

[17] ALEPH Collaboration D. Buskulic *et al.*. Measurement of Hadron and Lepton Pair Production from e^+e- Annihilation at Center-of-Mass Energies of 130 GeV and 136. *Physics Letters B*, 378:373+, 1996.

[18] ALEPH Collaboration R. Barate *et al.*. Study of the Muon Pair Production at Center-of-Mass Energies from 20-GeV to 136-GeV with the ALEPH detector. *Physics Letters B*, 399:329+, 1997.

[19] DELPHI Collaboration P. Abreu *et al.*. A Study of the Reaction $e^+e^- \to \mu^+\mu^-(n\gamma)$ at LEP and Search for New Physics at Annihilation Near 80-GeV. *Zeitschrift für Physik C*, 75:581+, 1997.

[20] Robert N. Cahn and Gerson Goldhaber. *The Experimental Foundations of Particle Physics.* Cambridge University Press, 1989.

[21] R.M. Barnett *et al.*, Particle Data Group. Review of Particle Physics. *Physics Review D*, 54:1+, 1996.

[22] M. Consoli and W. Hollik. Electroweak Radiative Corrections for Z Physics. Z Physics at LEP1 Volume 1: Standard Physics 08, CERN, Geneva, September 1989.

[23] M. Bohm and W. Hollik. Forward-backward Asymmetries. Z Physics at LEP1 Volume 1: Standard Physics 08, CERN, Geneva, September 1989.

[24] F.A. Berends. Z line shape. Z Physics at LEP1 Volume 1: Standard Physics 08, CERN, Geneva, September 1989.

[25] E. Accomando *et al.*. Standard Model Processes. Physics at LEP2, Vol. 1 1, CERN, Geneva, February 1996.

[26] M. Veltman. Limit on mass differences in the Weinberg Model. *Nuclear Physics B*, 123:89+, 1977.

[27] D. Bardin *et al.*. An Analytical Program for Fermion Pair Production in e^+e^- Annihilation. Technical Report 6443, CERN TH, 1992.

[28] D. Bardin *et al.*. Analytic Approach to the Complete set of QED Corrections to Fermion Pair Production in e^+e^- annihilation. *Nuclear Physics B*, 351:1+, 1991.

[29] F.A. Berends and W.L. van Neerven and G.J.H. Burgers. Higher order radiative corrections at LEP energies. *Nuclear Physics B*, 297:429+, 1988.

[30] S. Jadach and B.F.L. Ward and Z. Was. The Monte Carlo Program Koralz, version 4.0, for the Lepton or Quark Pair Production at LEP / SLC Energies. *Computer Physics Communications*, 79:503+, 1994.

[31] D. Bardin *et al.*. QED Corrections with Partial Angular Integration to Fermion Pair Production in e^+e^- Annihilation. *Physics Letters B*, 255:290+, 1991.

[32] D. Bardin *et al.*. A Realistic Approach to the standard Z peak. *Zeitschrift für Physik C*, 44:493+, 1989.

[33] Rabindra N. Mohapatra. *Unification and Supersymmetry.* Springer-Verlag, 1986.

[34] D. London and J. Rosner. Extra gauge bosons in E_6. *Physics Reviews D*, 34:1530+, 1986.

[35] M. Cvetic and P. Langacker. Z' Physics and Supersymmetry. In G.L. Kane, editor, *Perspectives in Supersymmetry.* World Scientific, 1997.

[36] CDF Collaboration, F. Abe *et al.*. Search for new Gauge Bosons Decaying into Dileptons in PP Collisions at $\sqrt{s} = 1.8$ GeV. *Physics Reviews Letters*, 79:2192+, 1997.

[37] A.D. Martin, R.G. Roberts, and W.J.Stirling. Parton Distributions Updated. *Physics Letters B*, 306:145+, 1993.

[38] A. Leike, S. Riemann, and T. Riemann. Z-Z' Mixing and Radiative Corrections at LEP 1. *Physics Letters B*, 291:187+, 1992.

[39] F. Boudjema and F. Renard. Compositeness. Z Physics at LEP1 Volume 2: Higgs Search and New Physics 08, CERN, Geneva, September 1989.

[40] L3 Collaboration, M. Acciarri *et al.*. Search for excited leptons in e^+e^- annihilation at $\sqrt{s} =$ 161 GeV. *Physics Letters B*, 401:139+, 1997.

[41] L3 Collaboration, M. Acciarri *et al.*. Search for excited leptons in e^+e^- annihilation at $\sqrt{s} =$ 130 GeV-140 GeV. *Physics Letters B*, 370:211+, 1996.

[42] Delphi Collaboration, P. Abreu *et al.*. Search for excited leptons in e^+e^- annihilation at $\sqrt{s} = 161$ GeV. *Physics Letters B*, 393:245+, 1997.

[43] Delphi Collaboration, P. Abreu *et al.*. Study of radiative leptonic events with hard photons and search for excited charged leptons at $\sqrt{s} = 130$ GeV-136 GeV. *Physics Letters B*, 380:480+, 1996.

[44] Aleph Collaboration, D. Buskulic *et al.*. Search for excited leptons at 130 GeV-140 GeV. *Physics Letters B*, 385:445+, 1996.

[45] Opal Collaboration, K. Ackerstaff *et al.*. Search for excited leptons in e^+e^- collisions at $\sqrt{s} = 161$ GeV. *Physics Letters B*, 391:197+, 1997.

[46] Opal Collaboration, G. Alexander *et al.*. Search for excited leptons in e^+e^- collisions at $\sqrt{s} = 130$ GeV and 136 GeV. *Physics Letters B*, 386:463+, 1996.

[47] Opal Collaboration, G. Alexander *et al.*. Search for unstable heavy and excited leptons in e^+e^- collisions at $\sqrt{s} = 170$ GeV-172 GeV. *European Physics Journal C*, 1:45+, 1998.

[48] C. Brouwer *et al.*. Large Scale Application of Magnetoresistors in the Magnetic Field Measuring System of the L3 Detector. *Nuclear Instruments and Methods A*, 313:50+, 1992.

[49] A. Adam *et al.*. The Forward Muon Detector of L3. *Nuclear Instruments and Methods A*, 383:342+, 1996.

[50] J. Simkin and C.W. Trowbridge. Three-Dimensional Computer Program (TOSCA) for Non-linear Electromagnetic Fields. Technical Report 97, Rutherford, 1979.

[51] B. Adeva *et al.*. Muon detection in the L3 experiment at LEP. *Nuclear Instruments and Methods A*, 277:187+, 1989.

[52] B. Adeva *et al.*. Test results of the L3 precision muon detector. *Nuclear Instruments and Methods A*, 289:335+, 1990.

[53] The Muon Group of the L3 Collaboration. A high resolution muon detector. *Nuclear Instruments and Methods A*, 289:335+, 1990.

[54] A. Aloisio *et al.*. The RPC trigger system for the L3 forward backward muon detector. In *San Francisco 1994, Computing in High Energy Physics*. Lawrence Berkley Lab., 1994.

[55] G .Carlino, P. Paolucci, D. Piccolo. RPC Performances at L3 experiment. L3 Internal Note 1811, University of Naples, 1995.

[56] R. Santonico, R. Cardarelli. Developement of Resistive Plate Counters. *Nuclear Instruments and Methods A*, 187:377+, 1981.

[57] O. Adriani *et al.*. Hadron Calorimetry in the L3 Detector. *Nuclear Instruments and Methods A*, 302:53+, 1991.

[58] Ulrich Uwer. Aufbau und Eichung der Szintillationszähler des L3-Experiments. Master's thesis, RWTH Aachen, 1990.

[59] B. Adeva *et al.*. The L3 BGO Electromagnetic Calorimeter. *Nuclear Instruments and Methods A*, 265:252+, 1988.

[60] F. Beissel *et al.*. Construction and Performance of the L3 Central Tracking Detector. *Nuclear Instruments and Methods A*, 332:33+, 1993.

[61] M. Acciarri *et al.*. The L3 Silicon Micro-vertex Detector. *Nuclear Instruments and Methods A*, 351:300+, 1994.

[62] K. Deiters *et al.*. Construction and Performance of a Large Cylindrical Wire Chamber with Cathode Readout. Technical Report 15, Institut für Hochenergiephysik Zeuthen, 1991.

[63] M. Acciarri *et al.*. Luminosity Measurement in the L3 Detector at LEP. *Nuclear Instruments and Methods A*, 381:236+, 1996.

[64] H.J. Bhabba. The Scattering of Positrons by Electrons with Exchange in Dirac's Theory of the Positron. *Royal Society of London Proceedings A*, 154:195+, 1936.

[65] S. Jadach *et al.*. Upgrade of the Monte Carlo Program Bhlumi for Bhabba Scattering at Low Angles to Version 4.04. *Computer Physics Communications*, 102:229+, 1997.

[66] P. Bene *et al.*. First Level Charged Particle Trigger for the L3 Detector. *Nuclear Instruments and Methods A*, 306:150+, 1991.

[67] L. Tauscher and S. Vlachos and M. Wadhwa. A charged particle trigger based on neural networks for the L3 experiment using the inner-TEC detector. L3 Internal Note 2016, University of Basel, 1996.

[68] R. Bizzari *et al.*. The L3 Energy Trigger. *Nuclear Instruments and Methods A*, 283:799+, 1989.

[69] P. Bagnaia *et al.*. The First Level Energy Trigger of the L3 Experiment. *Nuclear Instruments and Methods A*, 324:101+, 1993.

[70] P. Bagnaia *et al.*. The L3 Energy Trigger for the LEP 8 Bunch Operation. *Nuclear Instruments and Methods A*, 323:528+, 1992.

[71] M. Fukushima. L3 Level 1 Muon Trigger. L3 Internal Note 515, MIT, 1987.

[72] T.S. Dai, M. Fukushima. L3 Level 1 Muon Trigger Schematics. L3 Internal Note 668, MIT, 1989.

[73] Y. Bertsch *et al.*. The Second Level Trigger of the L3 Experiment. *Nuclear Instruments and Methods A*, 340:309+, 1994.

[74] C. Dionisi *et al.*. The Third Level Trigger System of the L3 Experiment at LEP. *Nuclear Instruments and Methods A*, 306:150+, 1991.

[75] C. Dionisi and A. De Salvo and C. Luci. New stategy for the L3 third level muon trigger algorithm. L3 Internal Note 2032, INFN-Sezione di Roma, 1996.

[76] Michel Goossens. ZEBRA. CERN Program Library Long Writeup, CERN-CN, 1992.

[77] I.C. Brock *et al.*. Luminosity Measurement in the L3 Detector at LEP. *Zeitschrift für Physik C*, 381:236+, 1996.

[78] C. Checci *et al.*. BGO Calibration at LEP II. L3 Internal Note 1892, BGO Group, 1995.

[79] U. Uwer. The L3 Scintillation Counter System: Description and Status. L3 Internal Note 2003, Aachen, 1996.

[80] D. Bourilkov, G. Rahal-Callot. TEC Calibration at LEP2 using High Energy Lepton Pairs. L3 Internal Note 2047, ETH Zurich, 1997.

[81] Michel Fabre. *The Dimuon Mass Resolution of the L3 at LEP and Its Dependence on the Muon Spectroemter Alignment.* PhD thesis, ETH, 1992.

[82] R. Assmann *et al.*. The Energy Calibration of LEP in the 1993 Scan. *Zeitschrift für Physik C*, 66:567+, 1995.

[83] R. Assmann *et al.*. LEP Energy Calibration in 1996. Internal Note 1, CERN PPE, 1997.

[84] L. Arnaudon *et al.*. Accurate Determination of the LEP Beam Energy by Resonant Depolarization. *Zeitschrift für Physik C*, 66:45+, 1995.

[85] U. Becker and Y.H. Chang and J.P. Rodin and B.R. Smith. Drift Velocity and Deflection in Nonperpendicular Electric and Magnetic Fields. *Nuclear Instruments and Methods A*, 360:476+, 1995.

[86] U. Becker and S.C. Nahn and J.P. Rodin and B.R. Smith. Effect of Nitrogen Contamination on Drift Chambers in Magnetic Fields. *Nuclear Instruments and Methods A*, 351:583+, 1994.

[87] Johannes Onvlee. *The Behaviour of the L3 Muon Chambers in a Magnetic Field.* PhD thesis, NIKEF, Amsderdam, 1989.

[88] V. Innocente and E. Nagy. Trajectory Fit in Presence of Dense Materials. *Nuclear Instruments and Methods A*, 324:297+, 1993.

[89] R. Brun *et al.*. GEANT version 3.16. Technical report, CERN-EE/DD, 1993.

[90] B. Adeva *et al.*. The L3 Database System. *Nuclear Instruments and Methods A*, 309:318+, 1991.

[91] H. A. Bethe. Passage of radiations through matter. *Physics Reviews*, 89:1256+, 1953.

[92] Ulrich Uwer. *Messung der Myonpaarproduktion auf der Z-Resonanz.* PhD thesis, RWTH Aachen, 1994.

[93] Stephan Roth. *Messung der Myonpaarproduktion und ihrer Strahlungskorrekturen mit dem L3-Detektor bei LEP.* PhD thesis, RWTH Aachen, 1997.

[94] Dehong Zhang. *Muon Pair Production in e^+e^- Collisions at the Z Resonance.* PhD thesis, NIKEF, Amsderdam, 1994.

[95] Arne Robohm. *Muon Pair Production at the L3 Experiment and Determination of Electroweak Parameters.* PhD thesis, ETH, 1998.

[96] MARK J Collaboration: M. Adeva *et al.*. Electroweak Studies in e^+e^- collisions: $12 < \sqrt{s} < 46.78$ GeV . *Physical Review D*, 38:2665+, 1988.

[97] Sabine Riemann. Limits on an Additional Heavy Gauge Boson Z' from the L3 experiment. L3 Internal Note 2126, Zeuthen, 1997.

[98] Sabine Riemann. Search for Z' Bosons with the L3 experiment. L3 Internal Note 2234, Zeuthen, 1998.

[99] A. Leike. Scaling of Z' exclusion limits and Z' measurements with energy, luminosity, and systematic errors. In *Tests of the Electroweak Symmetry Breaking*, 1997.

[100] K. Hagiwara and D. Zeppenfeld and S. Komamiya. Excited Lepton Production at LEP and HERA. *Zeitschrift für Physik C*, 29:115+, 1985.

[101] By F. Boudjema and A. Djouadi and J.L. Kneur. Excited Fermions at e^+e^- and ep colliders. *Zeitschrift für Physik C*, 57:425+, 1993.

[102] K. Hagiwara *et al.*. Excited Lepton Production at LEP and HERA. *Zeitschrift für Physik C*, 29:115+, 1985.

[103] M. A. Falagan. Search for Excited Leptons Decaying Radiatively, at $\sqrt{s} = 183$ GeV. L3 Internal Note 2217, CIEMAT, 1998.

[104] Shouxiang Wu, private communication.

[105] Alexei Lebedev, private communication.

[106] M. Skrzypek and S. Jadach and W. Placzek and Z. Was. Monte Carlo program KORALW-1.02 for W pair production at LEP-2 / NLC Energies with Yenni-Frautschi-Suura Exponentiation. *Computer Physics Communications*, 94:216+, 1996.

[107] M. Skrzypek and S. Jadach and M. Martinez and W. Placzek and Z. Was. Initial State QED Corrections to W Pair Production at LEP-2 / NLC: Monte Carlo versus Semianalytical Approach. *Physics Letters B*, 372:289+, 1996.

[108] F.A. Berends and P.H. Daverfeldt and R. Kleiss. Complete Lowest Order Calculations for Four Lepton Final States in Electron-Positron Collisions. *Nuclear Physics B*, 253:441+, 1985.

[109] T. Sjöstrand. PYTHIA 5.7 and JETSET 7.4 Physics and Manual. Technical Report 7112, CERN-TH, 1993.

[110] T. Sjöstrand. High-Energy-Physics Event Generation with PYTHIA and JETSET. *Computer Physics Communications*, 82:74+, 1994.

[111] F.A.Berends and R. Pittau and R. Kleiss. EXCALIBUR: A Monte Carlo program to evaluate all four fermion processes at LEP-200 and beyond. *Computer Physics Communications*, 85:437+, 1995.

[112] R. P. Feynman. Space-time Approach to Quantum Electrodynamics. *Physics Reviews*, 76:769+, 1949.

[113] J. Schwinger. On Quantum Electodynamics and the Magnetic Moment of the Electron. *Physics Reviews*, 73:416+, 1948.

[114] S. Tomonaga. On a Relativistically Invariant Formulation of the Quantum Theory of Wave Fields. *Progress in Theoretical Physics*, 1:27+, 1946.

[115] J. Schwinger. A Theory of the Fundamental Interactions. *Annalen der Physik*, 2:407+, 1957.

[116] S. Glashow. Partial-symmetries of Weak Interactions. *Nuclear Physics*, 22:579+, 1961.

[117] A. Salam and J. Ward. Electromagnetic and Weak Interactions. *Physics Letters*, 13:168+, 1964.

[118] C.N. Yang and R.L. Mills. Conservation of Isotopic Spin and Isotopic Gauge Invariance. *Physics Reviews*, 96:191+, 1954.

[119] P.W. Higgs. Broken Symmetries, Massless Particles, and Gauge Fields. *Physics Letters*, 12:132+, 1964.

[120] P.W. Higgs. Broken Symmetires and the Masses of Guage Bosons. *Physics Review Letters*, 13:508+, 1964.

[121] P.W. Higgs. Spontaeous Symmetry Breakdown without Massless Bosons. *Physics Reviews*, 145:1156+, 1966.

[122] J. Goldstone. Field Theories with 'Superconductor' Solutions. *Nuovo Cimento*, 154:19+, 1961.

[123] S. Weinberg. A Model of Leptons. *Physics Reviews Letters*, 19:1264+, 1967.

[124] A. Salam. Weak and Electromagnetic Interactions. In *Proceedings of the 8th Nobel Symposium*, 1968.

[125] S.L. Glashow, I. Illiopoulos, L. Maiani. Weak Interactions with Lepton-Hadron Symmetry. *Physics Reviews D*, 2:1285+, 1970.

[126] C. Bouchiat and J. Iliopoulos and P. Meyer. An Anomaly Free Version of Weinberg's Model. *Physics Letters B*, 38:519+, 1972.

[127] M. Y. Han and Y. Nambu. Three Triplet Model with Double SU(3) Symmetry. *Physics Review B*, 139:1006+, 1965.

[128] G. 't Hooft. Renormalizable Lagrangians for Massive Yang-Mills Fields. *Nuclear Physics B*, 35:167+, 1971.

[129] F. Hassert *et al.*. Observation of Neutrino-like Interactions without Muon or Electron in the Gargamelle Neutrino Experiment. *Physics Letters B*, 46:138+, 1973.

[130] G. Arnison *et al.*. Experimental Observation of Isolated Large Transverse Energy Electrons with Associated Missing Energy at $\sqrt{s} = 540$ GeV. *Physics Letters B*, 122:103+, 1983.

[131] G. Arnison *et al.*. Experimental Observation of Lepton Pairs of Invariant Mass around 95 GeV at the CERN SPS Collider. *Physics Letters B*, 126:398+, 1983.